NANOPARTICLE TRANSPORT THROUGH FRACTURES AND HETEROGENEOUS POROUS MEDIA

A Dissertation

Presented to the Faculty of the Graduate School

of Cornell University

In Partial Fulfillment of the Requirements for the Degree of

Master of Science

by

Sasikrishnan Kalyana Rama Subramanian

May 2012

ABSTRACT

Nanoparticles have a diffusion constant a couple of orders of magnitude smaller than inert chemical tracers such as potassium bromide (KBr), and this means that they can potentially be used to measure the degree to which subsurface flow occurs through fractures and high permeable zones in heterogeneous porous media. Using carbon based 2-5 nm particles (C-Dots); we inject dual tracers at different flow rates into a permeable core channel (fracture). The KBr tracer has time to diffuse into the surrounding halo much more than the particle tracer and arrives much later in the effluent. We carry out this kind of experiment in laboratory apparatus with different geometry (Hele-Shaw fracture cell, Rectangular and Cylindrical Beadpack columns). The Interpretation required models that take into account the flow in the halo as well as the core and, which also include dispersion. All experiments could be interpreted in a consistent fashion. The success suggests that it may be possible to assess the extent of fracture-controlled flow in the subsurface by combining non-sticking nanoparticles with an inert chemical tracer.

BIOGRAPHICAL SKETCH

Sasikrishnan Kalyana Rama Subramanian graduated in 2006 with Bachelors in Chemical Engineering from Visveswaraiah Technological University, Bangalore, Karnataka, India.

He came to Cornell in Fall 2007 to pursue an M.Eng in Chemical Engineering. While close to graduating with the M.Eng, an opportunity to work in an exciting diverse research project combining nanotechnology and subsurface tracers came up. To work on this project, he started the M.S. Program in Geological Science at Cornell under the guidance of Dr. Cathles.

Now, empowered with two Masters degrees from Cornell, he is diving into the entrepreneurial world to capitalize on energy and tech opportunities in India and USA.

To amma, appa, poorni, relatives and all my friends

ACKNOWLEDGEMENTS

I’d like to thank KAUST-CU Center for Energy and Sustainability for financially supporting my research work. I’d like to thank Dr. Cathles for guiding and advising me on this research problem. Over the past four years I have learnt a lot from him. His enthusiasm for research is exemplary and that has motivated me to a great extent. He is a very patient, kind and understanding Professor who goes out of the way to help when needed. I’d like to also thank Dr. Archer for serving in my committee and for providing valuable inputs and encouraging me throughout the program.

I’d like to thank my colleagues Alex, Vivian and Hongyi for always being there to help out in the lab and providing a great atmosphere to work in; KAUST-CU Research Staff (Dave and Brenda) for training me and helping me in the lab; Celia, Angie and Savannah for helping me order equipment and supplies and guiding me through the various administrative tasks.

My friends at Cornell and outside – Thank you! You all have and continue to enrich my life. I thank you all for your constant support and encouragement which has been critical for me to finish up.

I’d like to express my gratitude to my parents, sister, relatives and family friends for being patient and supportive.

TABLE OF CONTENTS

LIST OF FIGURES

LIST OF TABLES

CHAPTER 1

INTRODUCTION

Diverse fields such as groundwater contaminant migration, enhanced oil recovery, geothermal engineering, soil science and radioactive waste management all require understanding of flow through physical heterogeneities of different scales in the subsurface, and particularly how heterogeneities lead to flow short circuiting (i.e., the focusing of flow along pathways occupying a fraction of the total volume, with relatively little flow in the other parts of the volume). In the case of contaminant migration, whether the contamination results from a toxic spill, application of pesticide, or the escape of radioactive waste, short circuiting can cause the dangerous material to arrive at a sensitive location such as a drinking water aquifer much faster than expected. Short circuiting of water injected to push oil toward a recovery well can greatly reduce the effectiveness of a water flood. Fingering of cold recharge water into a geothermal well will degrade its power output. Understanding how fluid flow short-circuits in the subsurface is thus important for many reasons and has been a topic of research for many decades. The causes of flow short-circuiting are still not well understood, in large part because the short circuiting is difficult to define and measure.

One approach to understanding flow short-circuiting has been to run and interpret chemical tracer tests. If the flow is homogeneous and isotropic and the tracer is inert (e.g., does not interact with the mineral solids), the breakthrough curves for a solute can be modeled and interpreted using the advection-dispersion equation. Typically the tracer will attain 50% of its injected concentration when the pore fluid volume between an injection and monitor site has

been displaced once, and the breakthrough curve will be symmetric around the point at which it reaches 50% of its injected concentration (or half of the maximum concentration it ultimately attains). Halide salts, fluorescent dye molecules, and radionuclides are common tracers that are usually inert.

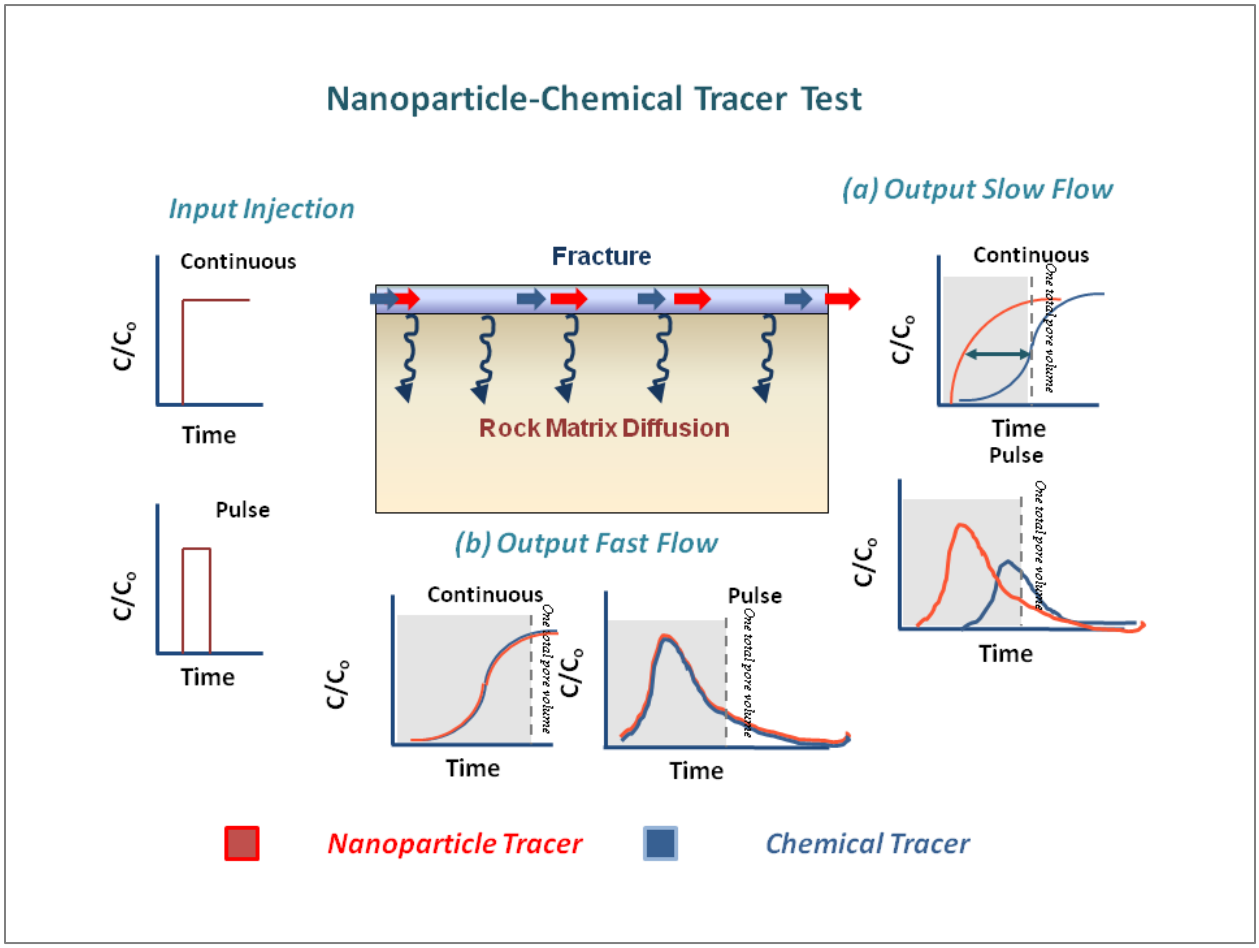

Figure 1: Tracer tests to interpret Flow Short-circuiting (a) slow flow (b) fast flow

When the flow is not uniform, breakthrough curves are generally not symmetric (Figure 1). For a pulse tracer input the breakthrough curve will commonly have a long tail and for a continuous input a much more gradual rise. These heterogeneous flow breakthrough curves have

been interpreted in two ways. One interpretation assumes that the tracer is transported at different rates through the contrasting permeability zones, and the breakthrough represents their summed contributions (flow channeling). Another (dual porosity) interpretation is that flow occurs through only part of the porosity, but the chemical tracer diffuses into the stagnant pores (matrix diffusion), as illustrated in Figure 1a. At low Darcy flow velocities, matrix diffusion tends to delay the arrival of chemical tracer [1-6] as illustrated in Figure 1a. At very fast injection rates the channel spectrum interpretation may be the most appropriate because there may not be enough time for the chemical to diffuse significantly into the matrix porosity, and the arrival curve would look as highlighted in Figure 1b.

Our purpose in this thesis is to investigate how tracers with a strong contrast in diffusivity can be used to quantify matrix diffusion in systems with heterogeneous flow. We do this by running laboratory experiment that combine a 2-5 nm sized engineered nanoparticle tracer with a diffusion coefficient of $\sim 10^{-7}$ cm^2s^{-1} with a solute tracer with a diffusion coefficient of $\sim 10^{-5}$ cm^2s^{-1}. We show that the difference in the breakthrough curves of two such tracers is a direct measure of the degree to which flow is short circuited by particularly permeable pathways. In other words, we show that fluid bypass can be measured by the gap in arrival times between a diffusing and non-diffusing tracer.

The problem with particle tracers has traditionally been their retention in the porous media. Larger particles settle, are strained or filtered out in pore throats, or are caught in flow eddies. Small particles (with higher Brownian motion) tend to agglomerate with each other or stick to the solid surface. The result is that the particles arrive at very low concentrations and this, as well as the losses by many different causes, complicates the interpretation of their arrival curves. Recent advances in nanotechnology, however, have led to design of nanoparticles 1 to

100 nm in diameter with differing shape and surface properties [7]. The nanoparticle surfaces can be coated with specific polymers or synthesized with specific functional groups that control their dispersivity in different solvents and reduce or eliminates their tendency to stick to rock minerals. We use a carbon-based nanoparticle with a central spherical carbon core and surface functionalization that make it water dispersible. These nanoparticles named C-Dots, fall in a size range of 2-5 nm that may be optimal for particle tracers (e.g., allows them to avoid eddy traps). In any case they are much larger than molecules (0.1-1 nm) and therefore have a much larger diffusion coefficient, yet they are smaller than all but the very smallest subsurface pores. Our C-Dots are photoluminescent with a high emission intensity that allows them to be detected at concentrations as low as ~0.01 ppm using a spectrofluorimeter.

Previous work with different types of tracers and through different heterogeneous media in the lab and field are reviewed in Chapter 2. Chapter 3 describes the experimental methods used to carry out the tests we have run. The results of the experiments are described in Chapter 4, and the interpretation of these results in Chapter 5. Chapter 6 summarizes the findings and Chapter 7 concludes with future recommendations.

CHAPTER 2

PRIOR WORK

Numerous laboratory studies on homogenous water saturated soils and sand and glass bead packs have focused on understanding the mobility and retention of colloidal size particles (1 nm to 10 microns) in different pore water conditions of impurity and contamination. Reviews [8-11] have summarized what is known about how colloid aggregation, settling, straining and deposition by filtration is induced by physical and chemical heterogeneities, as well as by hydrodynamic, attractive, and repulsive forces which act at different length scales. Experiments have shown how particle tracers differ from chemical tracers on the pore scale [12]. These studies have elucidated how colloids travel through subsurface, interact with different minerals and contaminants, and enhance the transport of contaminants that are adsorbed on their surface.

There have been relatively few studies that have addressed colloidal and bacterial transport in physically heterogeneous environments. The work that has been reported has sought to define the flowing and stagnant (dual) porosity of a porous media, to characterize the flow in artificial and natural fractures, to characterize the flow in fractures under field conditions, and to explain the observation that radionuclides and toxic organic compounds can attach themselves to natural subsurface colloids and be transported faster through fractures as a result [2, 9, 13-15]. We review this work below and then discuss the latest development: the deliberate engineering of nanometer scale tracer particles.

2.1 Particle Transport through artificially-constructed dual porosity/permeability systems

The effort required to construct heterogeneous systems in the laboratory has limited the literature in this area. The experiments that have been described differ primarily in their packing

material, orientation with respect to gravity, and interpretation. The experiments demonstrate channeling by the much earlier arrival of particle compared to chemical tracers. The channeling is attributed to size exclusion of the particles from the fine layers and to a lesser degree to matrix diffusion. The larger colloids seem to be strained out by flow through the porous media, while smaller particles are transported quickly unless rendered immobile by sticking. Hence, surface potentials of the particle as well as the porous media can play a significant role in the deposition as well as the dispersibility of the particles in the pore water suspensions.

Siers et al. [16] continuously injected 100 nm silica particles together with a conservative chloride tracer at a flowrate of one total pore volume per hour into a cylindrical central coarse-grained sand core that was surrounded by an annulus of finer grained sand. They observed that up to 60% of the injected mass of particles and chloride tracer arrived after 0.2 total pore volumes had been injected, indicating preferential flow (bypassing) through the coarse high permeability central core. However, there was very little time separation between the arrival of the particle and chloride tracers, we believe due to their high flow velocity through the core. As reported in Table B.1 (Appendix B), we calculate an Inverse Peclet number (Refer Section 5.2.1, Equation 2) for the chloride tracer to be 0.02. Based on our analysis, this is low to observe any significant separation of the two tracers, which was the case in their results. The authors used a 2D advection-dispersion model with reversible particle attachment and determined the dispersion parameters using the chloride breakthrough curve. The reversible attachment of the silica particles was verified by homogenous column tests. In addition, they showed that by controlling pore water chemistry the chemical interactions that reduce particle concentration by agglomeration and sticking could be eliminated and 100% of the injected colloid recovered.

Nieheren et al. [17] injected 1 micron carboxyl-modified latex microspheres and a uranine chemical tracer at three different flow rates (298, 82 & 55 cm h^{-1}) through a dual porosity laboratory column in which 35 micron cylinders with 10% porosity were regularly placed in a matrix of coarse (250-500 micron) quartz sand with ~25% porosity. The microspheres were labeled with a fluorescent molecule (crimson) that allowed them to be detected using an online custom-built microsphere counter. The uranine was detected with a fluorimeter. With decreasing flow rates, the recovery of the microspheres increased from 14 to 70% of the injected concentration and there was an increasing temporal separation between the early arrival of the microspheres and the later arrival of the conservative uranine tracer. The latter was attributed to size exclusion as well as matrix diffusion into the relatively immobile filter cylinders. The low recoveries were attributed to filtration. The decrease in filtration with decreasing flow rate was attributed to more effective electrostatic repulsion at slower flow rates.

Bradford et al. [18] created dual permeability combinations by packing cylindrical lenses of 710, 360, 240 and 150 micron sand in an annular matrix of another of these grain sizes. They injected 1 and 3 micron carboxylate modified latex colloids with a conservative sodium bromide tracer at ~0.1 cm min^{-1}. Size exclusion of the colloids led to the early breakthrough of the colloids compared to bromide ion. However straining and attachment of colloids reduced the total colloid recovery. A straining and attachment model was used to interpret the results. The results were consistent with previous work that showed straining which was dominant when the ratio of the diameter of the colloid to the porous media grain diameter is greater than 0.005.

Silliman [19] measured transport behavior of very large latex microspheres (2-90 microns) through layers of coarse and fine glass beads. Particle recovery was greater when the layering was parallel to the flow direction. In this configuration the large particles were transported rapidly through the more permeable layers, but at the same time the particle concentration was highly attenuated (2-3% of the injected concentration, C_o) due to settling and straining at the interface between the layers.

2.2 Particle Transport in laboratory-core fractures

Lab scale experiments studying transport of colloids through fractures generally use rock cores to mimic conditions in the field but sometimes utilize deliberately engineered fractures or channels. The cores may include only a single fracture (carbonate rock) or a network of fractures (fractured saprolite) that vary in aperture, length, and matrix mineralogy. The experiments inject, in a pulse or continuously, a variety of colloidal and microbial tracers. Some of the studies control the pore water geochemistry (ionic strength, pH, specific ion concentrations).

Toran and Palumbo [20] studied flow of three different colloids through 0.2-1 mm diameter polyethylene tubes 6-15 cm long in a sand column of 65 cm length and 5 cm diameter cross section. One micron microspheres, bacteria, and colloidal organic matter were injected in a pulse that was 5% of the total pore volume at a flow velocity of 1 m day^{-1} in experiments where the number, aperture and length of the tubes were varied. All tracers arrived earlier and with less retention when the tubes were present. The colloid arrival curves had an irregular shape which was attributed to the differing flow paths through the tubes.

Cumbie & McKay [21] studied the influence of size on the flow of fluorescent latex microspheres through a fractured saprolite soil column. Their cylindrical column was 35 cm long and 22 cm in diameter and consisted of a fracture network varying in orientation, length and aperture. Microspheres ranging from 0.05 to 4.25 microns in diameter were injected along with a conservative bromide ion tracer at a flow rate of 3.9 ml min^{-1}. The colloids were detected by particle counting with a fluorescent microscope that allowed detection to very low concentrations. The maximum concentration of injected colloid at the discharge end was very low (0.0007-1.4% C/C_o) compared to the bromide ion (79-93% C/C_o). The low recovery was attributed to settling and straining for the larger colloid particles and to diffusion into matrix blocks for the smaller colloids. This was confirmed by visual inspection with UV light of the matrix blocks and their surrounding fractures.

The same core sample was studied by McCarthy et al. [22] who showed that apart from the physical heterogeneity, the ionic strength and cation charge of the pore water significantly affected the transit of colloids through the fractured column. Pulses of multiple size colloids (0.1, 0.5, 1 and 2.1 microns) were injected together with bromide tracer at a slower flowrate (2 ml min^{-1}) and flushed with pore water. The experiments were repeated with different influent ionic strength and proportions of calcium and sodium ions. The significant difference in the arrival of the center of mass of colloids compared to the bromide was attributed to matrix diffusion and fluid bypass. However, there was no observable difference in the arrival times of the peak concentrations of the different sized colloids. The peak colloid centration was ~ 10^{-4} % of the injected concentration compared to bromide ion which peaked at ~15 % of the injected concentration. The low recovery of colloids was attributed to the pore structure and as well as

deposition due to pore water chemistry. Increasing the influent calcium ionic strength from 0.1 mM to 1 mM decreased the colloid recovery from 10 % to ~0.01 % C/Co for all colloid sizes, indicating that colloid filtering is very sensitive to changes in divalent cation concentration and ionic strength.

Very few attempts have been made to understand transport through a single natural fracture in laboratory. Zvikelsky and Weisbrod [23] studied the impact of the size of latex microspheres on their passage through a single fracture plane in two carbonate cores. Two cores with diameter 21 cm were obtained from a chalk formation in Israel and cut such that single fracture planes with equivalent hydraulic apertures of 183 and 380 microns respectively bisected the entire length (43.5 and 38.5 cm) of the cores. Carboxyl modified fluorescent latex microspheres 0.02, 0.1, 0.2 and 1 micron in diameter (detected using spectrofluorimetry) were injected with bromide and lithium ion solute tracers through the fractures at 1 mL min^{-1} for 384 and 183 minutes. The cores were then flushed with artificial rain water for ~1500 minutes. The 1 micron colloid arrived earliest, followed by the 0.2 micron colloid, the bromide ion, the 0.02 micron colloid, and the lithium ion. All the colloid tracers achieved 50% of their injected concentrations at more or less at the same time, and the recovery curves for the colloids all lacked a tail. The total recovery of 1 and 0.2 micron colloids were highest (90-95%), followed by the 0.1 micron (86%) and the 0.02 micron spheres (~75%). The recovery of the bromide and lithium ion was 95% and their recovery curves had long tails. The low recovery of the smaller particles was attributed to Brownian motion increasing the wall collision frequency and thereby increasing the deposition on the fracture walls as well as diffusion into the carbonate matrix. The loss in larger colloids was attributed to stokes settling. The authors could not satisfactorily

explain the early arrival of bromide ion compared to 0.02 micron microspheres. The recovery tails on the bromide and lithium ion tracers were interpreted to indicate diffusion into and out of the core from the fractures. The inverse peclet number for chemical tracer of 0.03 suggests that halo diffusion had minimal effect.

Reimus [24] studied the effect of Taylor's dispersion by injecting 1 and 0.3 micron synthetic carboxyl modified latex microspheres as well as silica microspheres tracers through water-saturated fractured granite and tuff. All the breakthrough curves for the continuous injection tests indicated early arrival of colloids when compared to a conservative iodide tracer. He attributed their faster transport to the reduced hydrodynamic dispersion and, at lower flow rates, to matrix diffusion of the iodide tracer.

2.3 Particle Transport in Natural Formations

Flow in fractured formations, aquifers, macropore networks in soils, karst conduits in caves and high permeability layers in sediments are examples of physically heterogeneous subsurface flow networks that have been studied with a host of particle tracers (bacteria, viruses, natural and synthetic colloids, fluorescent dyes, microspheres labeled with fluorescent molecules) ranging in sizes between 0.1 micron to 5 microns. The subsurface rocks tested vary in porosity, permeability, and mineralogy. Highly weathered clay-rich formations have been tested as well as unweathered granular aquifer formations. Most studies aimed at understanding the role of fractures and high permeability layers in transporting colloids and microbes faster than conservative solute tracers, which diffuse into the rock matrix. Large amounts of tracer are required to study large systems, and for this reason most of the field tests employ a slug or pulse injection.

One of the earliest particle tracer experiments was carried out by Cathles et al. [25] to assess the diffusional access of matrix rock to copper leaching. A dual component tracer consisting of 0.5 micron silica particles and sodium chloride was injected into a highly fractured rock in one well and fluid recovered slowly from monitor wells ~50 feet away. The particle tracer was predicted to arrive in a few days whilst the simultaneously-injected chloride tracer was predicted to take about a month to arrive in the monitor well. The particles were detected in the time predicted, but no chloride tracer was detected when the test was terminated one month after it started. The results were interpreted to indicate the chloride tracer had diffused into the matrix while the particle tracer had not, as had been predicted.

Becker et al. [26] conducted laboratory and field-scale tests in naturally-fractured tuff and dense crystalline granite rock using a range of carboxyl modified latex spheres (0.19 to 0.98 microns), that were detected using a flow cell device to sort and count particles and microbes (a method called cytometry). Cytometry is a proven technique to screen biological cells tagged with different fluorophores. It has been adapted to detect colloidal particles tagged with fluorophores as described in this paper. Including the laboratory tests, the experiments spanned three orders of magnitude in length scale (0.11, 0.67, 7.5, 30 & 36 m) and fluid velocity (0.4 – 120 m /day). An early but attenuated arrival of colloids compared to uranine tracer was observed. The early first arrival of colloids (defined as 0.1 % C/Co) compared to solute tracer was attributed to a combination of charge exclusion or repulsion, hydrodynamic chromatography, and taylor's dispersion enhancing the velocity of the colloids. It was also observed that the total recovery of the smaller colloids was greater than larger colloids. The authors suggest colloid recoveries in

long residence time experiments may be low because of settling and aggregation caused by cations in the groundwater. The recovery was an order of magnitude more in lab scale when compared to field results. This discrepancy between lab and field recoveries was attributed to the failure to match laboratory pore water chemistry to that of the ground water.

McKay et al. [27] injected four different colloidal tracers (one microsphere and three bacteria) over a distance of 13.5 meters through a highly fractured and weathered shale saprolite rock formation at the oak ridge reservation. The 100 nm fluorescent latex microspheres were detected by counting particles using a fluorescent microsope. The bacteriophage strains (PRD-1, MS-2, INA) were detected by culturing (plaque formation unit or PFU method). Plaque forming Unit or PFU is a measure of the number of particles which form plaques, per unit volume. Plaques are visible structures formed due to the replication and spreading of bacteriophages and can be used to quantify the number of strains of bacteriophage. Bacteriophages are viruses that feed on bacteria. They are 20 nm to 350 nm in diameter and up to 1000 nm long. The colloids arrived very rapidly suggesting first-arrival migration velocities up to 500 times faster than the chemical tracers (He, Ne, Rhodamine-WT) that had been injected in the same site previously. First arrival migration velocities are dependent on the sensitivity of the analytical instrument used for detection as well as the sampling rate. The difference in arrival time was attributed to diffusion of the chemical tracer (but not the particles) into the matrix. All the colloidal tracers had low recovery (10^{-1}-10^{-2} % C/Co) which was attributed to filtration. The retention rate did not decay exponentially with distance in a uniform manner. The experiments confirmed previous observations that that the travel times of bacteriophages through fractured rock can be 100 to 200 times shorter than a chemical bromide tracer due to low matrix diffusion [28], and that micro-

organisms can help in identifying major flow heterogeneities in the formations [29]. Bacteria can be detected to low concentrations [30], but their complex attachment mechanisms under different pore water conditions [31-35] complicates their use as tracers.

2.4 Engineered Nanomaterials

The above review highlights how diffusion, particle size, filtration, settling, sticking, flow rate, and water chemistry can reduce concentration of particles in solution and complicate the interpretation of particle tracer arrival curves. The rapid arrival of the particles can clearly reveal channelized flow but many of the experimenters conclude that there is significant uncertainty in predicting or interpreting field experiments due to the number of physical and chemical variables involved.

In this context a new sub class of colloids in the size range of 1-100 nanometers has been gaining attention. The nano size of these particles distinguishes them from the larger colloids. Nanoparticles such as metal oxides, carbon soot and other organic complexes exist naturally in the subsurface but can also be engineered synthetically. They can be constructed from a variety of base materials in a wide range of sizes and shapes. Their surface can be decorated by attaching a host of different polymers and functional groups to provide stability in different solvents. If the particles are labeled with a fluorophore molecule or have well defined optical and spectral properties, they can be detected by UV/Visible spectrometry. Refractive index measurements have also been successfully used for high weight percent particle concentrations. Particle counting techniques such as flow cytometry are challenging for particles smaller than 20 nm.

The mobility of these engineered nanomaterials through porous media has been recently assessed. Engineered nanomaterials such as fullerene C-60, single walled carbon nanotubes or SWNTs, alumina, titania and silica have been passed through a host of columns packed with different kinds of soils, sands and glass beads. Their mobility, aggregation, and deposition onto the porous media surface have been evaluated based on DLVO and filtration theory under different physical and geochemical conditions. A recent review by Petosa et al. [36] compiles an exhaustive list of experimental studies carried out to understand and evaluate aggregation and deposition of different engineered nanomaterials in different porous media systems. They also discuss the theoretical approaches to understanding the mechanisms behind the observed transport phenomena.

To our knowledge only a few experiments evaluating nanoparticles as tracers in sedimentary rock cores and bioremediation have been reported. Rodriguez et al. [37] injected high concentration (5 and 20 wt%) 5 and 20 nm silica nanoparticle suspensions into sandstone and limestone cores to study their retention and mobility. The observed transport behavior was different from chemical tracers, with effluent breakthroughs later than one pore volume and a long tailing. The effluent particle concentration plateaued at less than the injected concentration. Mazen et al. [38] injected polystyrene nanoparticles cross-linked with divinyl benzene into limestone cores to study the stability of these particles while being transported through the core and also address the size limitations of the particle to transport through tight pores as found in low permeability hydrocarbon reservoirs. Due to their large surface area, zerovalent iron nanoparticles have been utilized for insitu reduction of toxic chemicals such as TCE [7] and arsenic(III) [39]. There have been only a very few nanomaterials used as tracers in the

subsurface in the size range of 20 nm or less which our experiments suggest may be optimal. These include certain virus strains and fluorescent latex nanospheres [23]. Recently, [40] carried out a push-pull nanoparticle tracer field test in the calcitic Gawahar oil reservoir, and recovered ~86% of injected tracer in ~7000 barrels of recovered water. Unfortunately a chemical tracer was not simultaneously deployed in this experiment.

CHAPTER 3

EXPERIMENT

This Chapter discusses in detail the different column designs we have used to simulate fracture-matrix systems (Section 3.1), how they are packed under water to create a dual permeability media (Section 3.3), the tracers used (Section 3.4), and how the tracer experiments were conducted and the effluent tracer concentrations analyzed (Sections 3.5 and 3.6).

3.1 Column Design

Experiments were carried out in apparatus of four different designs: (i) cylindrical columns (ii) rectangular glass bead packs, (iii) Hele-shaw cells, and (iv) homogenous columns:

(i) Two cylindrical columns with different diameters were used for the flow experiments. One was a 50 cm long acrylic tube with an inner diameter of 4 cm capped on both ends. The centers of the caps were connected to 2-3 mm diameter tubing. The central core of coarse beads was formed by filling a stainless 300-micron steel wire mesh, rolled into a cylindrical tube, with the coarse glass beads. The second column was a stainless steel tube 50 cm long and in 2.54 cm in diameter with the same style end fittings and interior mesh tube filled with coarse beads (Figure 2, Figure 3 and Table 1).

(ii) The apparatus we call the rectangular beadpack was constructed from acrylic and loaded with two layers of beads with the larger diameter bead layer at the bottom. The inlet and outlet were placed at the bottom of the beadpack to promote flow through the coarse bead layer. Slots were machined at regular intervals along the sides of the acrylic cell where they confined the fine bead layer. Thin rectangular sheets of acrylic fitted

into these slots. These barriers, which we call baffles, are intended to impede flow through the fine layer (Figure 4, Figure 5 and Table 2).

(iii) The hele-shaw cells were constructed to simulate flow through a single fracture with diffusion into an adjacent relatively impermeable matrix from a “core” slot with larger dimensions and thus permeability. The equi-dimensional rectangular slot (the core) connected to a planar slit (the matrix halo). The core slot has an internal volume of (1460) micro-liters, and the halo slit (7800) micro-liters. Baffles made of viton divide the halo slit at regular intervals, forming compartments. At the top end of each halo compartment there is an outlet that can be opened or closed. This outlet is used to drain the fluid and chemicals from the halo compartments as well as to remove air bubbles when deionized water is initially introduced into the system (Figure 6, Figure 7 and Table 3).

(iv) A homogeneous acrylic cylindrical columns 54 cm long and 1 cm internal diameter were fitted with end caps connected to 0.5 mm diameter tubing. Stainless steel mesh (100 micron openings) was cut to a circular form with a diameter equal to that of the internal diameter of the tube so it holds the porous media away from the end caps and distributes the flow uniformly across the top and bottom. The column was wet packed with 500 micron glass beads which was used to assess any tendency for particles to stick to the beads used in the experiments (Figure 8).

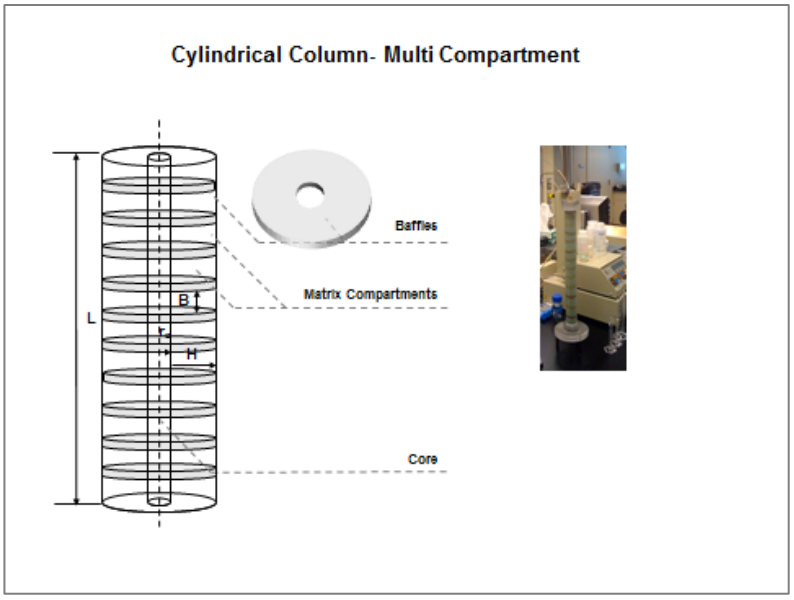

Figure 2: Design and picture of a multicompartment cylindrical column

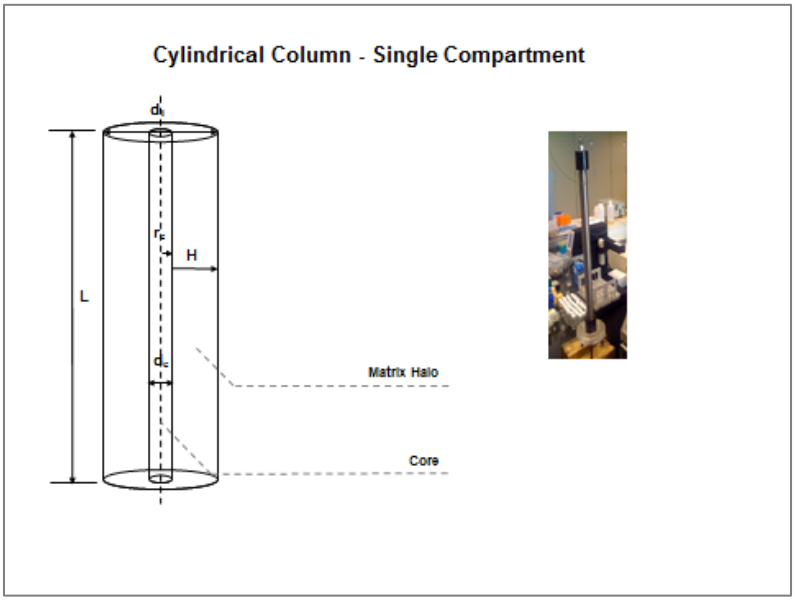

Figure 3: Design and picture of a single compartment cylindrical column

Table 1: Dimensions of cylindrical columns

Column	Length L (cm)	Internal Diameter d_T (cm)	Core diameter d_c (cm)	Halo radius H (cm)	Core Volume (cc)	Halo Volume (cc)	Total Volume (cc)
Stainless Steel	50	2.54	0.7	0.92	19.2	234	253.2
Plexi-glass	50	3.8	1	1.4	39.3	527.5	566.8

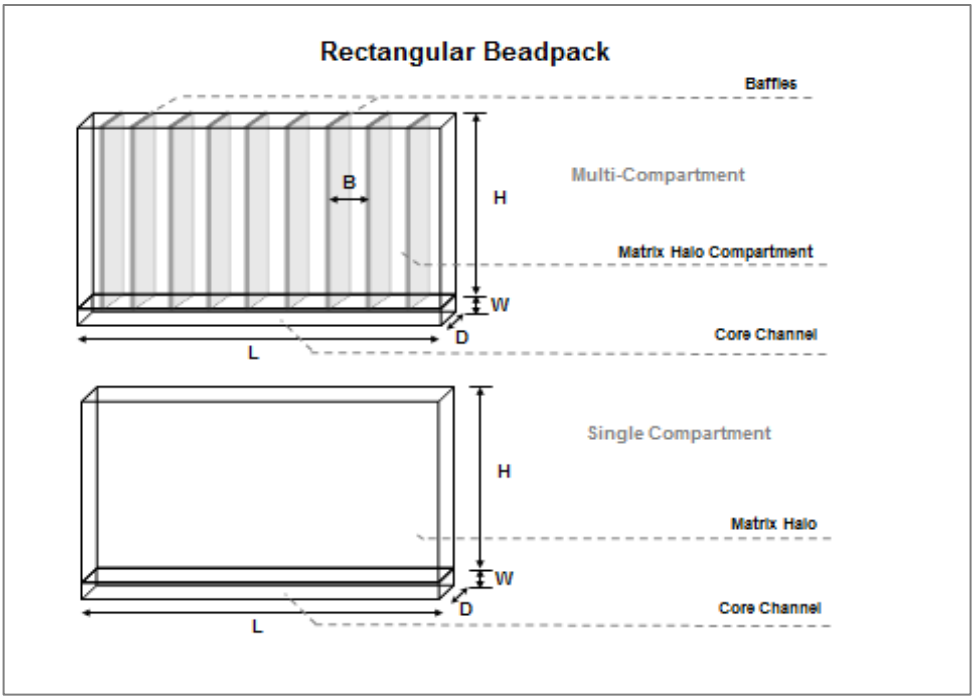

Figure 4: Design of single and multi-compartment rectangular beadpack

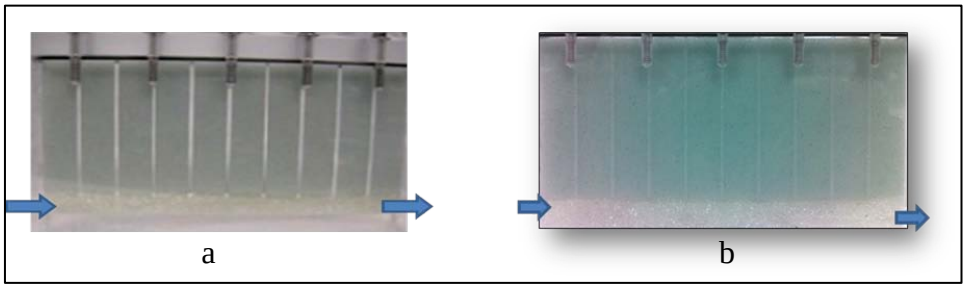

Figure 5: Picture of a)Multi-Compartment b)Single Compartment Rectangular Beadpack

Table 2: Dimensions of rectangular beadpacks

Rectangular Beadpack	Single Compartment	Multi-Compartment
Length L (cm)	15	15
Channel width D (cm)	1	1
Channel Height W (cm)	1	1
Channel depth D (cm)	1	1
Channel Volume (cc)	15	15
Halo height H (cm)	7	7
Halo width L (cm)	1	1
Halo Volume (cc)	105	105
Total Volume (cc)	120	120

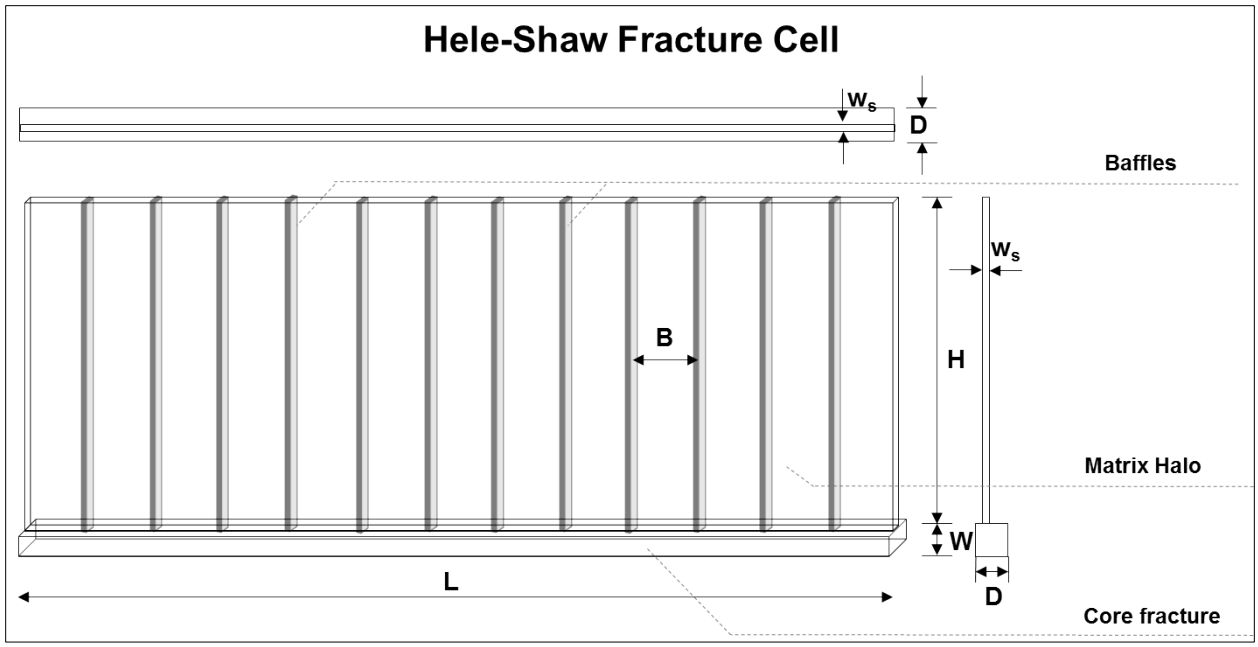

Figure 6: Design schematic of a Hele-Shaw Cell Fracture

Figure 7: Top View of Hele-Shaw Cell

Table 3: Dimensions of Hele-Shaw Cell

Specification	Hele-Shaw Cell
Core slot length L (mm)	200
Core slot width W (mm)	2.7
Core slot depth D (mm)	2.7
Planar slit length L (mm)	200
Planar slit width w_s (mm)	0.635
Planar slit height H (mm)	48
Core volume (cc)	1.46
Planar slit volume (cc)	7.78
Total volume (cc)	9.24

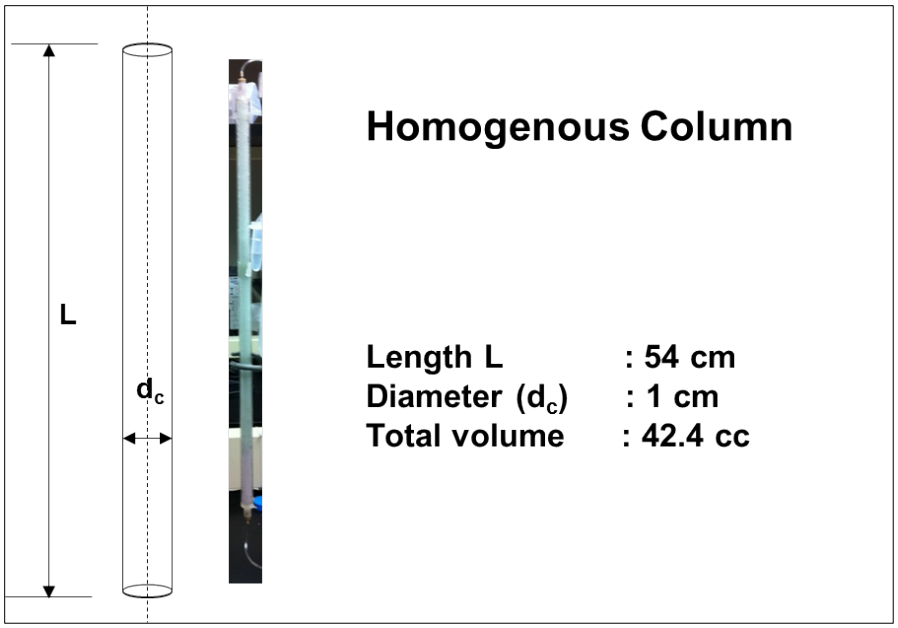

Figure 8: Design and specifications of a homogeneous column

3.2 Porous Media

The cylindrical columns and rectangular beadpacks were packed with fine and coarse beads. The coarse beads were soda lime glass beads 3 mm or 1 mm diameter, uniform in shape and size, and free of any visible stains or coloration. Industrial quartz beads with average diameter of 250 microns and 500 microns respectively were used as the fine beads. These were washed repeatedly in deionized water until the pore water was clear and not turbid, indicating absence of suspended impurities. The pore water pH was 6.8-7.0.

3.3 Column Packing

The packing procedure is critical and differs for cylindrical and rectangular geometry, and also as for single and multiple halo compartments. The objective is to create two different permeability layers using glass beads of different size with minimum intermixing at the interface of the two layers. All the systems were wet packed (e.g., the beads were introduced into a water-filled column) to ensure 100% water saturation.

3.3.1 Packing a Single Compartment Cylindrical Column

A stainless steel wire mesh was used to separate the coarse and fine glass beads. The wire mesh is rolled into a cylinder and fitted into a circular base that just fits into the column. The mesh has pore openings of 300 microns which prevents mixing of the 500 micron fine glass beads with the 3000 micron coarse glass beads. The wire mesh cylinder is placed into the column, and the column is filled with water up to half the height of the column. The coarse glass beads are then poured into the cylindrical wire mesh. Slurry of fine glass beads is then slowly sedimented into the annular space in the column. As the column is being filled with beads, it is important to ensure the cylindrical core is centered. At regular intervals, the entire tube is mechanically vibrated to ensure a dense and uniform packing. Once packed, the top of the column is fitted with a circular wire mesh to ensure the fine glass beads are not entrained into the effluent. A fitting at the top end cap is connected to the effluent plumbing line.

3.3.2 Packing a Multi-compartment Cylindrical Column

The fine glass bead annular section can be divided into compartments by periodically inserting circular brass disks with a hole cut in the center. The circular brass disks (which we call baffles) are designed to slide over the central core and just fit into the column. A baffle is inserted at the bottom of the column. The slurry of fine glass beads is then slowly introduced into the annular space in the column, and additional baffles are inserted at regular intervals as the annulus is filled. The tube is mechanically vibrated as it is filled to ensure tight and uniform packing. Once packed, the top of the column is fitted with a circular wire mesh and connected to the effluent plumbing line.

3.3.3 Packing a Multi-compartment Rectangular Beadpack

As above the beadpack is filled with deionized water up to half the total volume of the beadpack, and the 1000 micron coarse glass beads are introduced so that they form a layer one cm thick at the base. The baffles are then slid into the slots provided in the beadpack. The fine glass beads are then sedimented in each individual compartment.

3.3.4 Packing a Single Compartment Rectangular Beadpack

Unlike the cylindrical column where the flow is vertical, the rectangular beadpack is designed such that the flow is horizontal. The empty cell is filled with deionized water up to half its total volume. A 1 cm layer of 1000 micron coarse glass beads is then introduced. The 250 micron fine glass beads are then sedimented on top of the coarse layer to form a dual permeability system. Fast and irregular addition of the fine glass beads can lead to significant intermixing with the coarse glass beads and development of air pockets. Unlike the cylindrical column, no mesh separates the coarse and fine layers. Once the packing is completed, a lid is fitted to the top of the cell so that the cell is sealed.

3.3.5 Packing the Cylindrical Homogenous Column

The homogenous columns are filled with deionized water to half the column height and the glass beads are sedimented into the column. At regular intervals, the column is mechanically vibrated to ensure tight and uniform packing. The top and bottom end caps are fitted with stainless steel mesh to prevent entrainment of glass beads into the plumbing system.

3.3.6 Setting up a Hele-Shaw Cell

The hele-shaw cell has to be free of air bubbles and completely water saturated. As seen in Figure 9, a three-way valve is used to bypass the air bubble that develops from the leur lock when switching the syringe. Any bubble entrained in the water-saturated cell, can be removed through the halo slit by tilting the cell such that the bubble is removed through the effluent plumbing.

Figure 9: Picture of a 3-way valve

3.4 Tracers

Carbon Dots (C-Dots) are functionalized nanoparticles which are hydrophilic in nature. The particles we use in the experiments discussed below are spherical in shape with a diameter in the range of 2-5 nm as seen in Figure 10. The zeta potential at pH 7 is -5 mV (Malvern Zetasizer). The C-Dots are inherently photoluminescent with high emission intensities enabling their detection at low concentrations of 0.01 ppm. In some experiments we use silica nanoparticles (S-100). These commercially available particles have an average diameter of 92 nm and are labeled with green fluorophore.

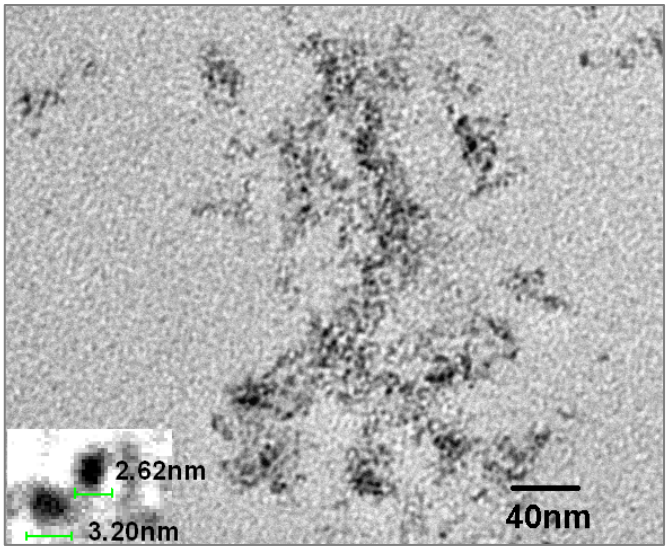

Figure 10. TEM image of C-Dots

Our experiments have been carried primarily out with C-Dots as the nanoparticle tracer and potassium bromide as a conservative chemical tracer. The aqueous suspension of C-Dots was mixed with potassium bromide to form a dual tracer suspension. The injected concentrations used are 50 and 1000 ppm for C-Dots and bromide ion respectively. Silica nanospheres and rhodamine 6G were also used in some experiments. Table 4 shows the properties of all the tracers employed in our experiments.

Table 4: Tracer properties

Tracer	Size (nm)	Fluorophore Label	Zeta Potential (mV)
C-Dots	2-5	Inherent	-5
S-100	92	Fluorescein	-40
Rhodamine-6G	0.9	Inherent	n.a
KBr	0.1	None	n.a

3.5 Experiment Operation

The packed columns are flushed with deionized water for five to ten pore volumes to ensure that the medium is completely saturated with water. The effluent pore water is visually inspected

for turbidity and impurity entrainment. The procedures followed for continuous or pulse injection experiments are outlined below. A syringe pump, connected to a three-way valve, pushes water containing the tracers through the packed column, which in turn is connected, to a fraction collector. As seen in Figure 11, experiments are carried out in continuous or step injection modes:

(i) Upon completion of the experiment, deionized water is injected through the column for at least 5-6 total pore volumes or until the effluent concentrations reach the baseline levels for the tracers. If the concentration does not drop to baseline levels even after sustained injection of deionized water or if we are testing a new particle tracer, the column is repacked.

(ii) Continuous injection - Around one total pore volume of tracer solution is injected through the column at a constant flow rate with a syringe pump.

(iii) Pulse Injection - A known quantity of tracer solution (generally about one-fourth of a core pore volume) is injected into the column as a pulse that is followed by injection of DI water at the desired flow rate.

(iv) Effluent samples are collected over regular time intervals by an automatic sampler. The sampling interval is determined by the duration of the experiment, the expected transit time through the core, and the sample volume required for analysis.

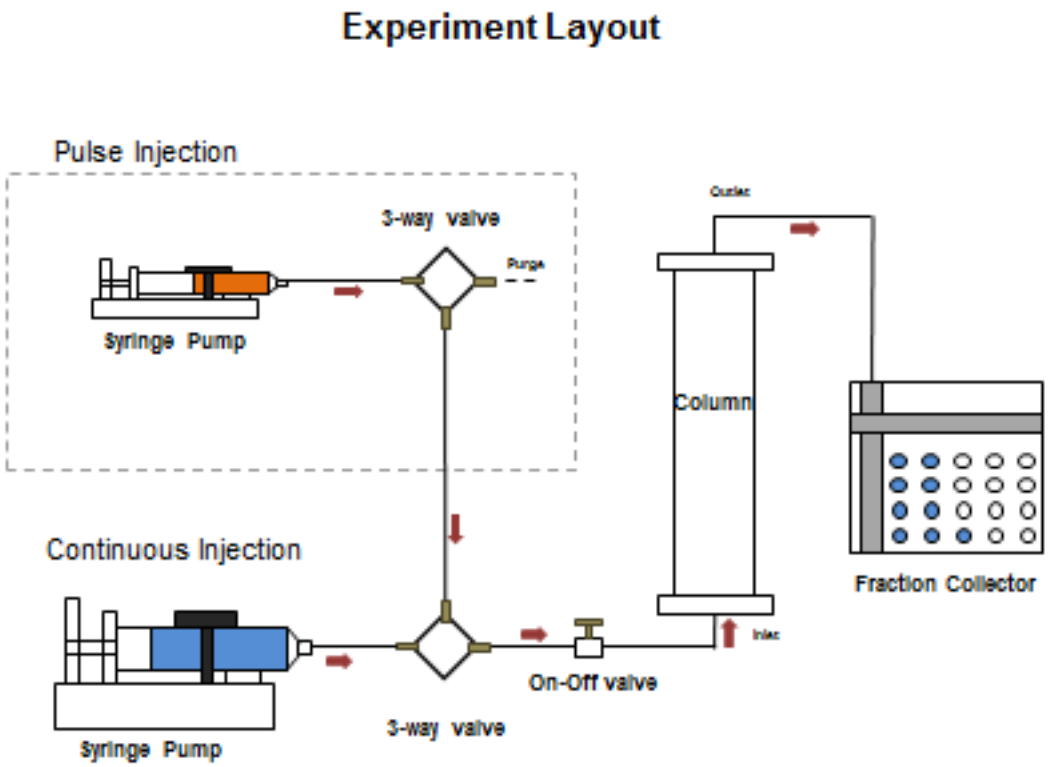

Figure 11: Experiment layout for continuous and pulse injection

3.6 Tracer Analysis

The C-Dots, fluorescent silica and rhodamine 6G have characteristic spectral signatures that can be detected using a Molecular Devices M2E Spectrophotometer which excites the tracers at their excitation wavelength and records the intensity at the corresponding peak emission wavelength. Within the dilute concentration regime, the emission intensity increases linearly with increasing concentration. The emission intensity of standards tracer concentrations (ranging from 0.1% to 100% of injected tracer concentration) was measured and a calibration curve relating emission intensity to tracer concentration was derived. The intensity of the signal generally remains stable but the calibration is done periodically to ensure the correct concentration measurements. Bromide ion concentration was measured using an Ion Selective Electrode Meter fitted with a bromide ion specific electrode. The voltage measured is related to the concentration using a set of concentration standards. The calibration curves mostly remain stable, however it is good practice to calibrate every time a set of unknown concentrations is measured – both for fluorescence intensity and voltage measurements.

CHAPTER 4

RESULTS

The tracer tests carried out can be largely classified into experiments which screened particles for stickiness by passing particle solutions through a homogeneous porous media column (Section 4.1), and experiments that sought to measure fluid bypass by simultaneously injecting nanoparticle and chemical tracers through heterogeneous systems. Sections 4.2 to 4.5 discuss the effluent breakthrough curves of tracer tests through the Hele-Shaw Cell (fracture-matrix), Rectangular Beadpacks, and Cylindrical Beadpacks (dual permeability).

4.1 Homogeneous Column

The first issue is whether the particle or chemical tracers adhere or sticks to the glass beads in an obvious fashion. Figure 12 shows the arrival curves when 4 total pore volumes of water containing C-Dot, KBr, Rhodamine-6G, and 100 nm SiO_2 tracers were passed through a 500-micron homogeneous (no permeable core) glass beadpack at 0.1 cm^3 min^{-1}. The C-Dot and bromide tracer breakthrough at ~1 pore volume and reach 100% of injected concentration by 1.1 pore volumes. The Rhodamine-6G breakthrough is delayed by nearly a full pore volume, however, and ultimately reaches only ~80% of the injected concentration. The 100 nm silica bead tracer is also delayed but less so than the rhodamine tracer. When a 3 cc (~$1/5^{th}$ of a pore volume) tracer pulse is injected at 0.1 cm^3 min^{-1} followed by DI water (Figure 13), the C-Dots have a breakthrough curve almost identical to that of the bromide tracer, and again the Rhodamine-6G tracer arrival is delayed, and the S-100 particle tracer is delayed, but delayed less. The SiO_2 tracer is delayed about half as much as the Rhodamine-6G tracer in both the continuous and pulse experiments.

The rhodamine tracer is clearly sticking to the glass beads. After injection the beads can be seen to have a distinct red tint. We did not check for adhesion of the S-100 particles. Because of the clear delay, neither the S-100 nor rhodamine tracers are suitable for experiments where the flow is through glass beads, and for the most part, these tracers were not used in the experiments reported below.

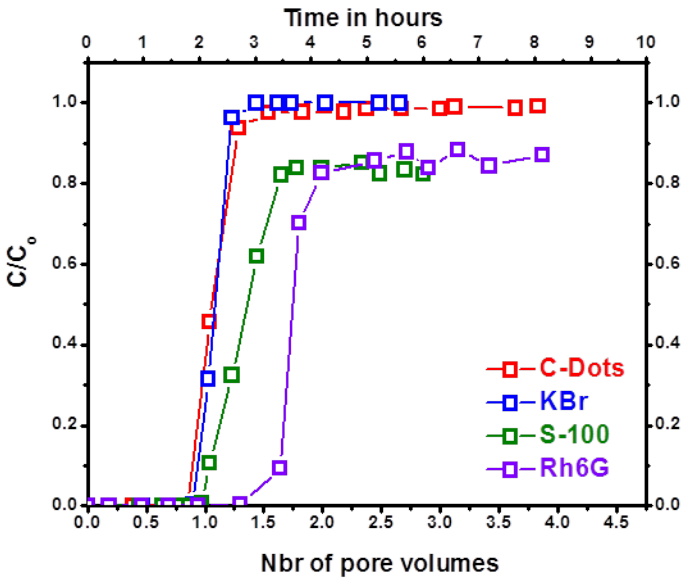

Figure 12: Effluent tracer concentrations as a fraction of injected concentration (C/C_o) vs number of pore volumes and time through a 500 micron glass bead homogeneous column. Continuous injection at flowrate of 0.1 mL min^{-1}

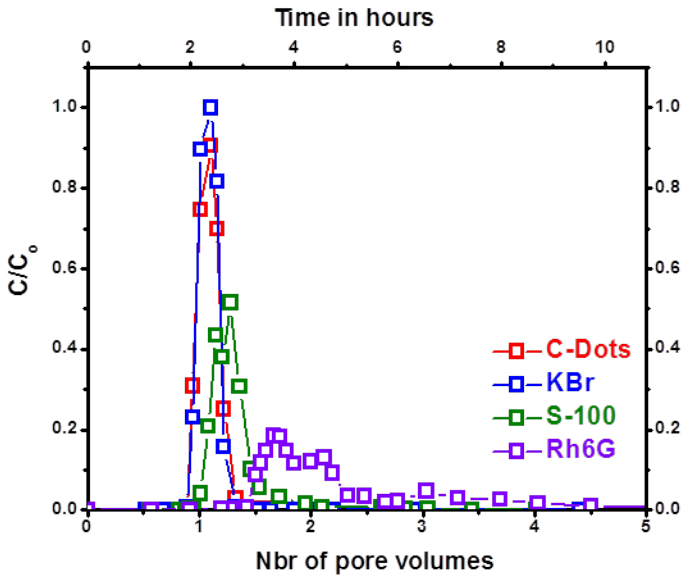

Figure 13: Effluent tracer concentrations as a fraction of injected concentration (C/Co) vs number of pore volumes and time through a 500 micron glass bead homogeneous column. Pulse injection at flowrate of 0.1 mL min^{-1}

4.2 Hele Shaw Cell Experiments

The flow parameters for the Hele Shaw experiments discussed here, as well as the parameters for experiments discussed in subsequent paragraphs, are given in Table 5. Figure 14 plots the concentration of bromide and C-Dot tracer in the effluent from the Hele Shaw cell as a function of time and the number of core pore volumes injected. The vertical line shows when one total pore volume has been injected. The tracers were simultaneously injected through the channel of the Hele Shaw channel-slit system at two very different flow rates. The first breakthrough of tracer occurs at one core pore volume. The pore volume of the matrix slit is 5.32 core pore volumes. When the tracers are injected at a low flow rate of 0.17 core pore volumes per day (~0.24 cc day^{-1}) for 40 days, the breakthrough of the bromide tracer is significantly delayed compared to the C-Dot tracer (Figure 14). In contrast when the tracers are injected at a fast flow rate (8 total pore volumes injected at 496 core pore volumes per day or ~720 cc day^{-1}), the C-Dot and bromide tracers break through at around one core pore volume and plateau to 80% of the injected tracer concentration (C_o) by 3 core pore volumes (Figure 15). The curve then gently rises to close to 100% of the injected concentrations of both tracers when around 20 core pore volumes have been injected.

Figure 16 shows when SiO_2 and KBr tracers are injected continuously at 0.6 cm^3 day^{-1} for 14 days the S-100 starts arriving at ~ 1 core pore volume and earlier than the bromide tracer. The bromide tracer breaks through at around 2 core pore volumes but rises sharply and begins to plateau and by the end of the experiment both the tracers have reached ~55% of injected concentration with the S-100 arrival curve remaining distinct from the bromide tracer arrival curve.

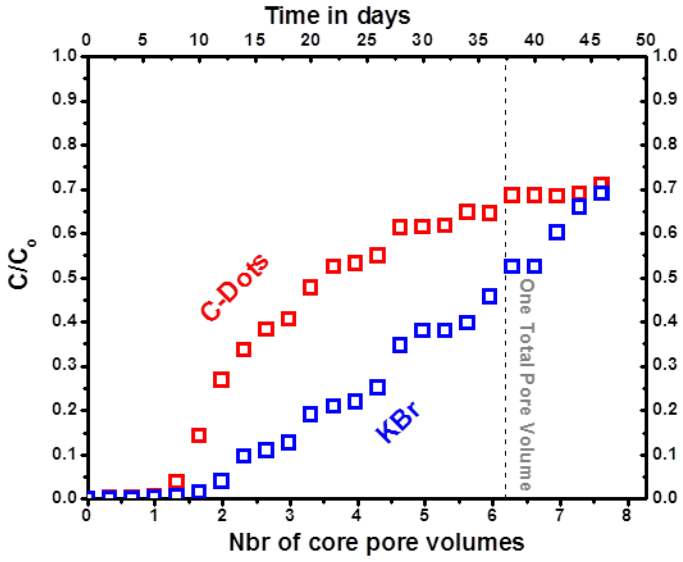

Figure 14: C-Dot and KBr tracer effluent concentration as a fraction of injected concentration (C/C_o) vs number of core pore volumes through a Hele-Shaw Cell injected continuously at flowrate of 0.24 mL day^{-1}

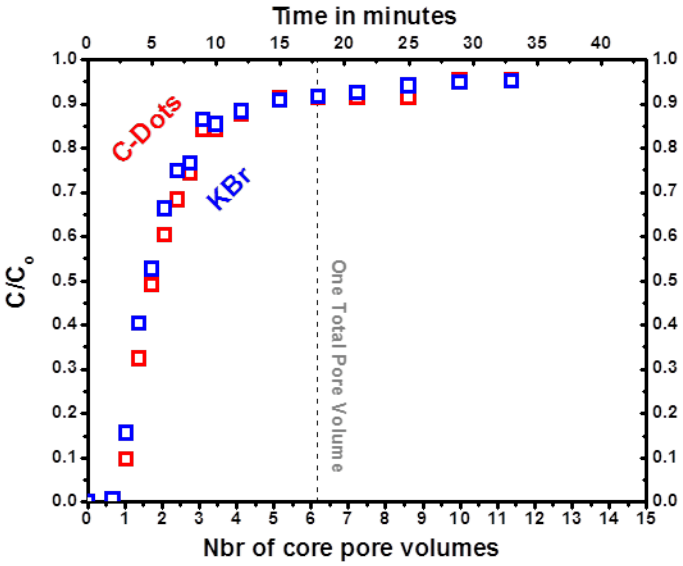

Figure 15: C-Dot and KBr tracer effluent concentration as a fraction of injected concentration (C/C_o) vs number of core pore volumes through a Hele-Shaw Cell injected continuously at flowrate of 720 mL day^{-1}

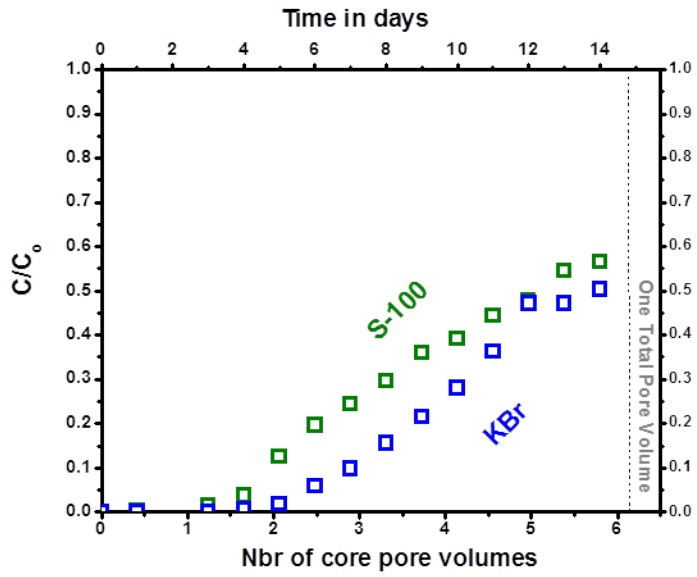

Figure 16: S-100 and KBr tracer effluent concentration as a fraction of injected concentration (C/C_o) vs number of core pore volumes through a Hele-Shaw Cell injected continuously at flowrate of 0.6 mL day^{-1}

Table 5: List of flow parameters for experiments; C - Number of compartments, Injection (c) continuous, Injection (p) Pulse, Q - Flowrate

Geometry	Ref. Fig	C	Inj.	Q (cm^3 d^{-1})	Core vol. (cm^3)	Total fluid vol. (cm^3)	Duration (days)
HS Cell	14	13	C	720	1.45	9.24	0.069
HS Cell	15	13	C	0.24	1.45	9.24	46
HS Cell	16	13	C	0.6	1.45	9.24	14
Rect. Beadpack	20	1	C	5.06	5.06	35.46	22.5
Rect. Beadpack	17	10	C	5.06	4.5	36.8	5.5
Rect. Beadpack	18	10	C	5.06	4.5	36.8	10
Rect. Beadpack	19	10	C	5.06	4.5	36.8	10
Rect. Beadpack	21	10	p (2cc)	5.06	4.5	36.8	9
Plexi-column	22	11	C	28.8	15.7	210.9	19
Plexi-column	23	11	C	28.8	15.7	210.9	12
SS Column	24	1	P	12	7.7	81.9	30
SS Column	25	1	P	28.8	7.7	81.9	18

4.3 Rectangular Beadpack

Figure 20 and Figure 17 show C-Dot and bromide effluent tracer concentration for a single compartment experiment run for 20 days and a multi-compartment experiment run for 6 days. In both the cases the injection rate was ~1 core pore volume per day and the C-Dots arrive earlier than the bromide ion tracer, but plateau at ~70-80 % of their injected concentration. Generally the C-Dot tracer concentrations are greater than the bromide, but the bromide tracer reaches higher concentrations than the C-Dots in the later stages of the single compartment experiment (Figure 20).

Figure 18 and Figure 19 show S-100 and rhodamine tracers injected at ~1 core pore volume per day for 10 days break through at 1.5 to 2 core pore volumes and plateau at concentrations of ~70% and ~55% and of their injected concentrations, respectively. The delay in arrival of these tracers is expected because the homogeneous column experiments showed these tracers adhere to glass beads.

Figure 21 shows the C-Dots and bromide tracer concentrations in the effluent when a pulse of 2 cc (~2/5 core pore volume) was injected and followed with ~7 days of water injection at one core pore volumes per day. The peak concentrations for the C-Dots and the bromide were 25% and 15% of the injected concentration respectively.

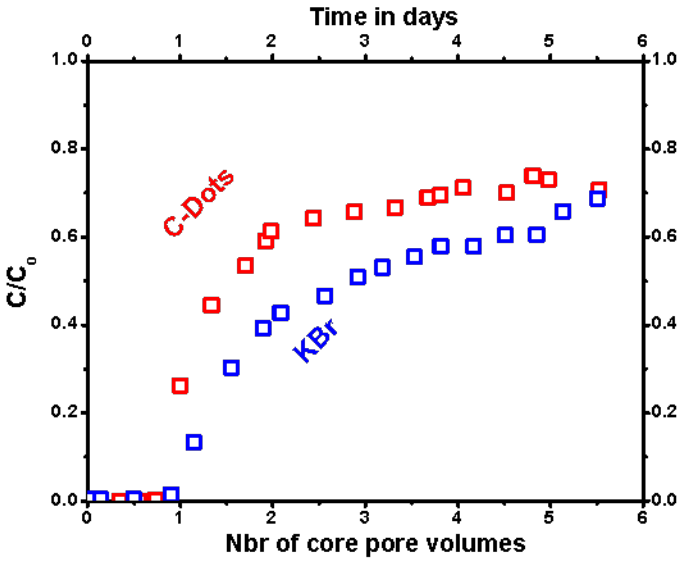

Figure 17: C-Dot and KBr effluent concentration as a fraction of injected concentration (C/C_o) vs number of core pore volumes through a ten compartment rectangular beadpack injected continuously at flowrate of 5.06 mL day^{-1}

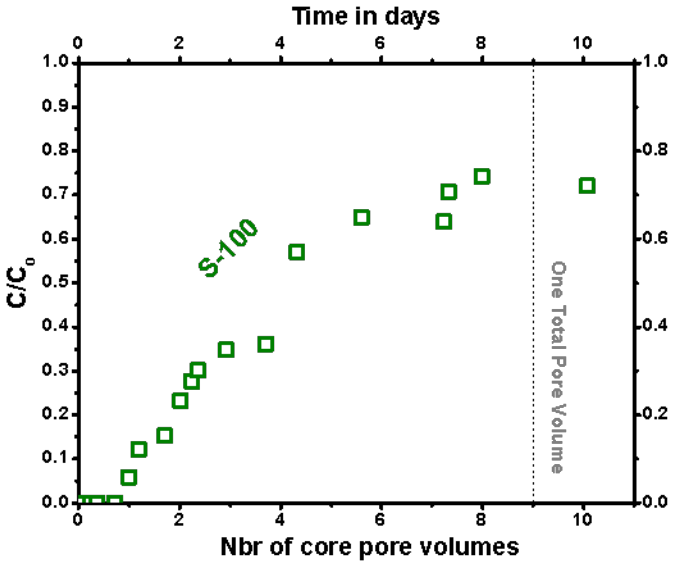

Figure 18: S-100 effluent concentration as a fraction of injected concentration (C/C_o) vs number of core pore volumes through a ten compartment rectangular beadpack injected continuously at flowrate of 5.06 mL day^{-1}

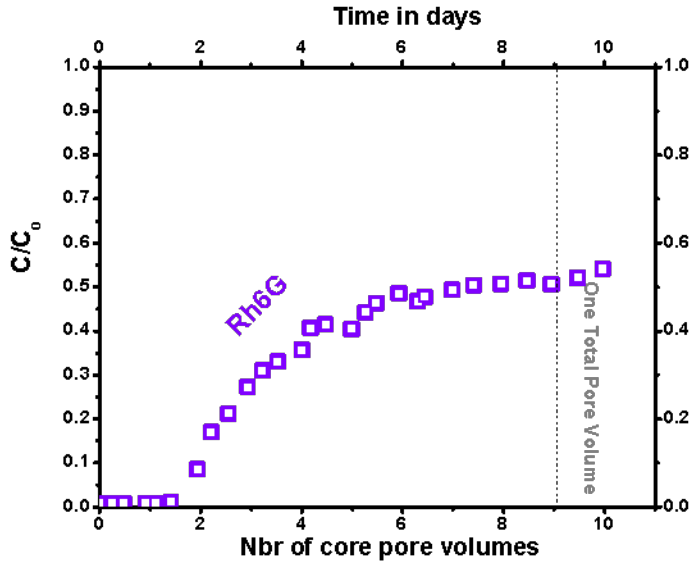

Figure 19: Rhodamine-6G effluent concentration as a fraction of injected concentration (C/C_o) vs number of core pore volumes and time through a ten compartment rectangular beadpack injected continuously at flowrate of 5.06 mL day^{-1}

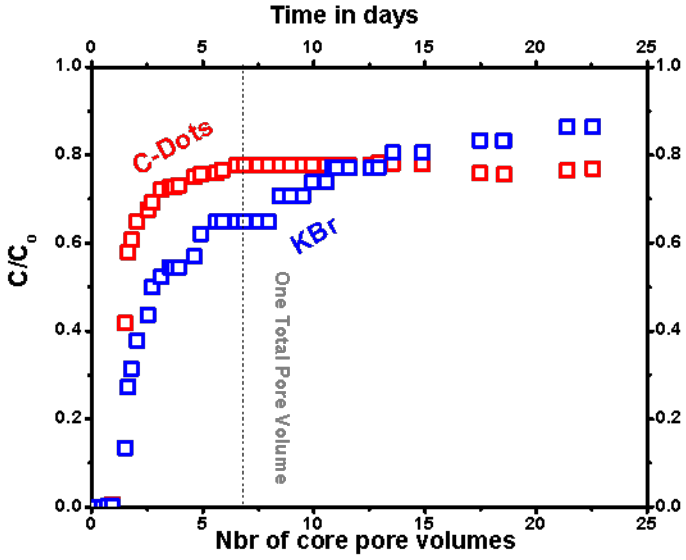

Figure 20: C-Dot and KBr effluent concentration as a fraction of injected concentration (C/C_o) vs number of core pore volumes through a single compartment rectangular beadpack injected continuously at flowrate of 5.06 mL day^{-1}

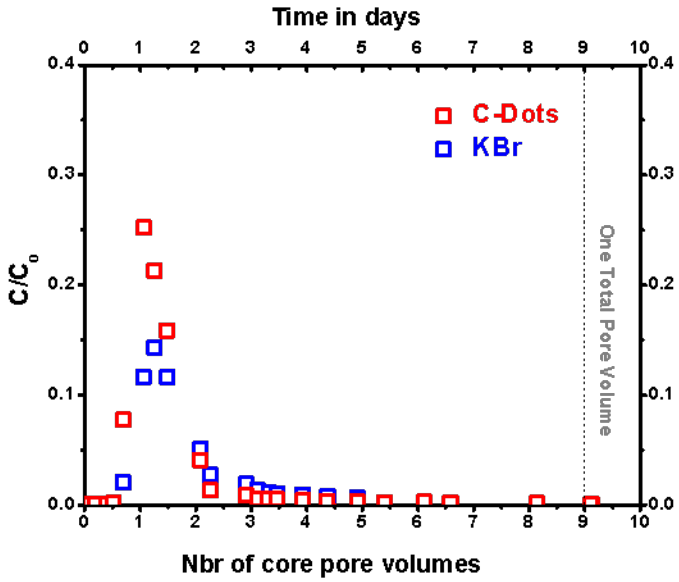

Figure 21: C-Dot and KBr effluent concentration as a fraction of injected concentration (C/C_o) vs number of core pore volumes through a ten compartment rectangular beadpack injected as a2 cc pulse followed by DI water at flowrate of 5.06 mL day^{-1}

4.4 Plexiglass Column

Figure 22 shows that when C-Dot and bromide tracers are injected through a plexi-glass column with baffles at rates of ~ 1.8 core pore volumes per day, the C-Dots arrive earlier than the bromide tracer but plateau at ~60-70% of their injected concentration whereas the bromide tracer reaches the injected concentration levels. Figure 23 shows an S-100 tracer arrives earlier than the bromide and plateaus at ~80% of the injected concentration.

4.5 Stainless Steel Column

Figure 24 and Figure 25 show that when a 2 cc slug (~ 1/4 of the core pore volume) of water containing both KBr and C-Dot tracers (a dual tracer pulse) is injected at 0.5 and 1.2 cm^3 h^{-1} followed by DI water, the arrival peak for the C-Dots is at ~0.7 core pore volumes, while of

the peak of the bromide tracer occurs at ~2 total pore volumes. The peak concentrations the C-Dots and bromide tracers are 2% and 1% of the injected concentrations respectively.

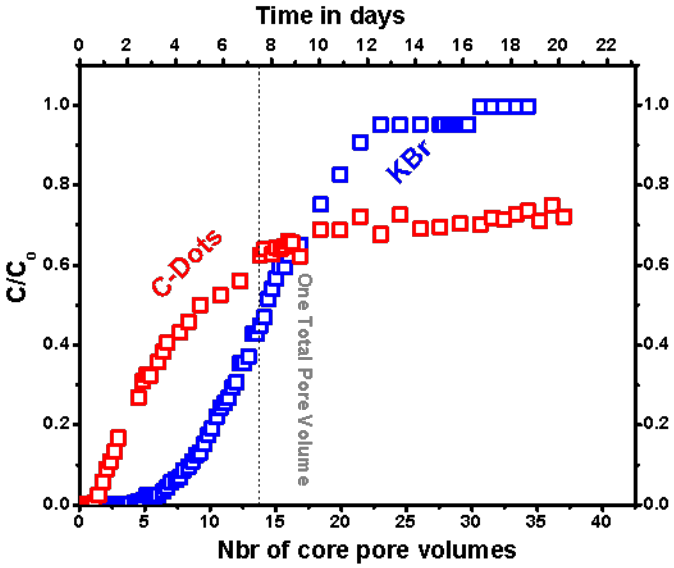

Figure 22: C-Dot and KBr effluent concentration as a fraction of injected concentration (C/C_o) vs number of core pore volumes through a 11 compartment plexi-glass cylindrical column injected continuously at flowrate of 28.8 mL day^{-1}

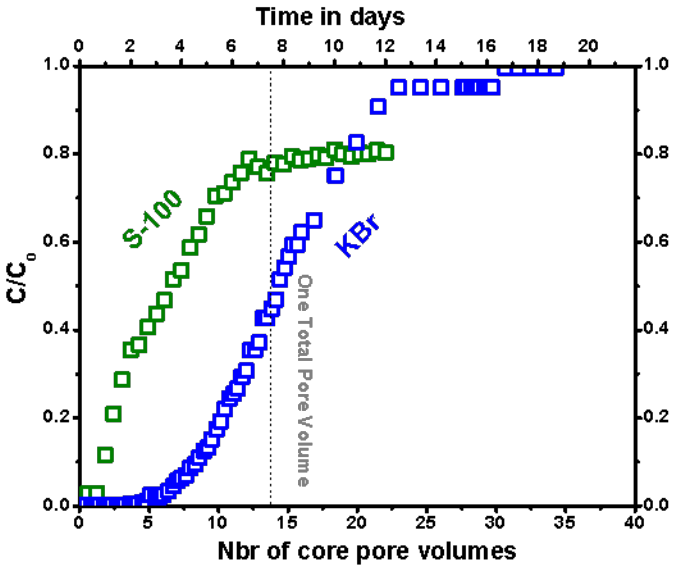

Figure 23: S-100 and KBr effluent concentration as a fraction of injected concentration (C/C_o) vs number of core pore volumes through a 11 compartment plexi-glass cylindrical column injected continuously at flowrate of 28.8 mL day^{-1}

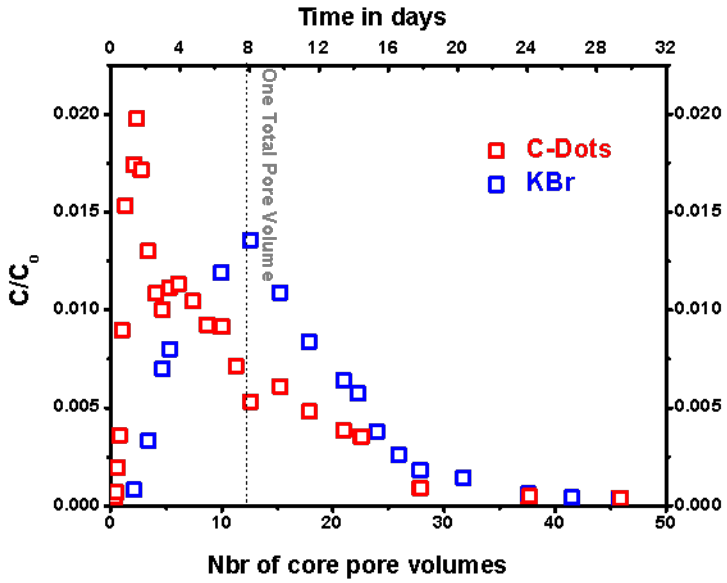

Figure 24: C-Dot and KBr effluent concentration as a fraction of injected concentration (C/C_o) vs number of core pore volumes through a single compartment stainless steel cylindrical column injected as a 2 cc pulse followed by DI water injection at flowrate of 12 mL day^{-1}

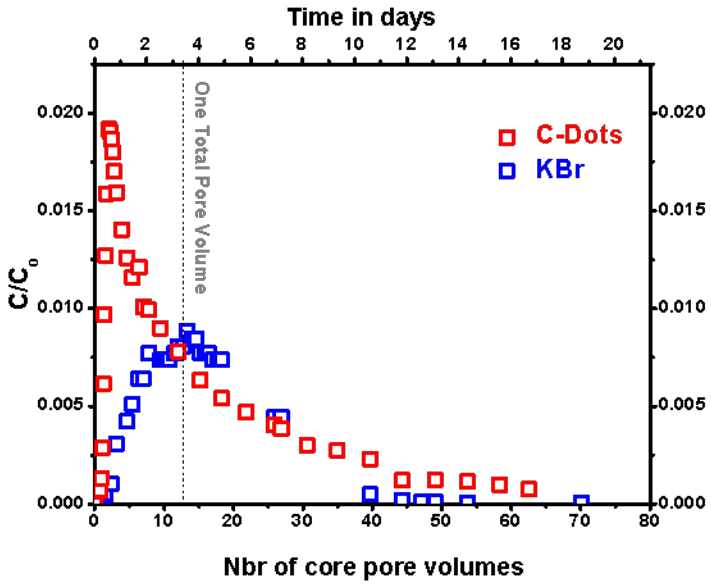

Figure 25: C-Dot and KBr effluent concentration as a fraction of injected concentration (C/C_o) vs number of core pore volumes through a single compartment stainless steel cylindrical column injected as a 2 cc pulse followed by DI water injection at flowrate of 28.8 mL day^{-1}

CHAPTER 5

INTERPRETATION

The experimental results presented above are interpreted in this chapter by (1) first comparing the tracer stored in the diffusion halo to the amount of storage expected based on an inverse Peclet number, and (2) by then comparing the observed effluent concentration curves to those predicted by finite element models.

5.1 Diffusion Constants

Aqueous diffusion constants can be calculated using the Stoke-Einstein equation, which relates the diffusion coefficient to the inverse of the diameter of the particle or molecule.

$$D_\infty = \frac{k_B T}{3\pi\mu d_p} \qquad \ldots\ldots \quad (1)$$

where is the aqueous diffusion coefficient in $cm^2\ s^{-1}$, is the Boltzmann constant (1.38065×10^{-23} J K^{-1}), T is absolute temperature (293.15 K), and is the diameter of the nanoparticle in nm.

Based on this equation, nanoparticles in the range of 1-10 nm should have diffusion coefficients in the range of 4.3×10^{-6} to 4.3×10^{-7} $cm^2\ s^{-1}$, while colloids in the size range of 100 – 1000 nm should have diffusion coefficients in the range of 4.3×10^{-8} to 4.3×10^{-9} $cm^2\ s^{-1}$. Solutes such as bromide ion and large molecules such as rhodamine have diffusion coefficients between 1.4×10^{-5} to 4.3×10^{-6} $cm^2\ s^{-1}$ [41]. The KBr diffusion constant is known from direct measurement and is about 2×10^{-5} $cm^2 s^{-1}$[42]. The diffusion constants used in our modeling are listed in Table 7. The model assumes that the effective diffusion constant is the aqueous diffusion constant

given in Table 7 multiplied by the beadpack porosity and divided by a tortuosity. For a bed of uniform spheres [43] [44] a tortuosity of 1.5 is appropriate.

5.2 Inverse Peclet Number and Storage Analysis

5.2.1 Inverse Peclet Number

The experiments described above show that, depending on the flowrate, diffusion coefficient, and geometry, tracers will arrive at close to one *core* pore volume or one *total* pore volume. For slower flow rates there is more time for tracer to diffuse into those parts of the system where the flow is relatively stagnant (the Hele Shaw slit or the beadpack/column halos), thereby delaying their breakthrough. This can analyzed using an inverse Peclet number, N_{iPe}, defined by the ratio of the advection time constant through the entire core to that of diffusion time through the matrix halo:

$$N_{iPe} = \frac{Advection\ time\ constant}{Matrix\ diffusion\ time\ constant} = \frac{\tau_{adv}}{\tau_{diff}}$$

$$\tau_{adv} = t_c \frac{V_t}{V_c}, \tau_{diff} = \frac{H^2}{D_{eh}}, and \begin{Bmatrix} D_{ec} \\ D_{eh} \end{Bmatrix} = \frac{D_\infty}{\tau} \begin{Bmatrix} \Phi_c \\ \Phi_h \end{Bmatrix} + \begin{Bmatrix} a_L \Phi_c v_c \\ a_T \Phi_h v_h \end{Bmatrix} \quad \ldots\ldots\ldots \quad (2)$$

Here the advection time constant is the time for the tracer to move across the system assuming tracer fills the total porosity (the porosity of the channel and the matrix or halo) as it progresses, t_c is the transit time of fluid in the channel ($=L/v_c$, where L is the length of the channel and v_c is the true velocity of fluid in the channel), V_t is the total pore volume of the whole system (core and matrix), V_c is the pore volume of the core channel, H is the width of the matrix halo, D_{eh} and D_{ec} is the effective diffusion coefficient in the matrix and core channel respectively, τ is the tortuosity of the diffusion pathways around the beads (assumed to be the

same in the matrix and channel), D_∞ is the aqueous diffusion constant of tracer, Φ_c and Φ_h are the porosities in the channel and matrix, v_h is the true velocity of the fluid in the matrix, and a_l and a_T are the longitudinal (parallel to flow) and transverse (perpendicular to flow) dispersion coefficients. In the finite element modeling, we use the effective diffusion constant in the channel to compute the diffusion and dispersion parallel to the flow direction in the channel after each advective advance of the fluid.

At fast flow rates (low system residence times) or small diffusion constants, there is no time for a tracer to diffuse into the halo during its transit through the core, and $N_{ipe} << 1$, If both the nanoparticle and chemical tracers have very small values of N_{iPe} they will have similar breakthrough curves. When the peclet number is 1 or more for the KBr tracer, and ~0.1 for the nanoparticles tracer, and chemical tracer arrival will be delayed relative to the particle tracer. The tracers begin to be distinguishable when one of the tracers has a N_{iPe} more than about 0.1 or more.

At very low peclet numbers, tracers arrive when the flow channel volume is displaced once. At peclet numbers close to 1 or more a tracer arrives when one total pore volume (flow channels plus stagnant matrix) is displaced once. The total concentration at peak arrival is similar in both cases (providing the tracers to not stick to the pore surfaces or become stuck in the pore throats). For example, the similar peak concentrations in Figure 13 suggest neither the C-Dot nor KBr tracers stick to the pore surface.

Table 6: Peclet Numbers for the selected experiments in Figures 13-24. $D_{e\text{-}c}$ and $D_{e\text{-}KBr}$ are effective diffusion coefficients and $N_{iPe\text{-}c}$ and $N_{iPe\text{-}KBr}$ are the peclet numbers for C-Dots and Bromide respectively

Geometry	Fig	Tracer Separation	H (cm)	L (cm)	τ	Φ_c	Φ_h	u (cm d^{-1})	$D_{e\text{-}c}$ (cm^2 d^{-1})	$D_{e\text{-}KBr}$ (cm^2 d^{-1})	$N_{iPe\text{-}c}$	$N_{iPe\text{-}KBr}$
H-S Cell	14	yes	4.8	20	1	1	1	3.31	0.053	1.74	0.21	2.81
H-S Cell	15	no	4.8	20	1	1	1	9931	0.053	1.74	$7x10^{-5}$	$9x10^{-4}$
Rect. Beadpack	17	a bit	7	15	1.5	0.35	0.3	5.25	0.015	0.35	0.004	0.06
Rect. Beadpack	20	a bit	7	15	1.5	0.35	0.3	5.25	0.015	0.35	0.004	0.06
SS Column	24	yes	0.92	50	1.5	0.4	0.3	31.1	0.015	0.35	0.23	3.10
SS Column	25	yes	0.92	50	1.5	0.4	0.3	74.8	0.015	0.35	0.09	1.29
Plexicolumn	22	Yes	1.4	50	1.5	0.4	0.4	36.6	0.007	0.23	0.11	1.42

5.2.2 Sequestration Analysis

The breakthrough curves for continuous injections can be used to measure the mass of tracer sequestered into the matrix. The fraction, *f*, of the total pore volume of the experimental system filled with tracer can be determined by integrating the flow rate through the system times $(1\text{-}C(t)/C_o)$ over the duration of the experiment and dividing by the total pore volume of the system:

$$f = \frac{\int_0^t Q\left(1 - \frac{C(t)}{C_o}\right) dt}{V_{tot}} \qquad \ldots\ldots\ldots \quad (3)$$

If the peclet number is very small, *f* should never significantly exceed the volume fraction represented by the core channel. If the peclet number is around 1, the fraction will approach the total pore volume of the system.

The plots in Figure 26 show the fraction of the total fluid volume that is filled with KBr (blue) or C-Dot (red) tracer as a function of the number of core pore volumes injected. Between 0 and 1 core pore volumes injected, the fraction of both tracers sequestered (*f*) increases linearly to the fraction of the total pore volume that is represented by the core channel. This just represents the filling of the core channel. For injected volumes greater than one core pore volume, the sequestration curves depart from one another if diffusion into the halo is more significant for one of the tracers. If the tracers moved uniformly through the whole pore volume, the sequestration curves would both follow the dashed extension of the solid one-pore-volume curve. If the tracers did not diffuse into or pass through the halo at all, the curves would follow the horizontal dashed line. Tracer sequestration would never exceed a single core pore volume. Tracers that enter the halo a bit, but not fully, will lie somewhere between these two dashed guide curves. If the tracers enter the halo by diffusion, and one diffuses in more than the other, the sequestration curves of the two tracers will diverge.

The plots in Figure 26 are ordered so the N_{iPe} (the ratio of diffusion to flow rate) decreases from top to bottom. The N_{iPe} for each tracer (KBr blue and C-Dots red) is indicated on each plot. A brief caption characterizes the experiment, and a reference is given to the data figure in the previous section that shows the arrival curves that correspond to the sequestration plot. More information for each case is provided in Table 6.

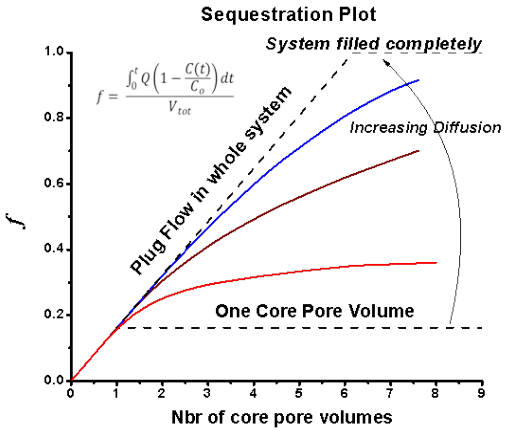

f-Plot Illustration

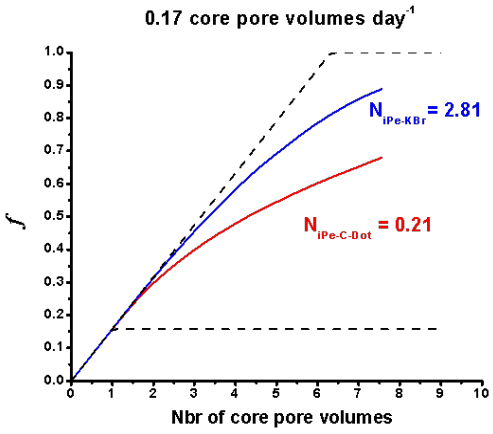

A: Reference Figure 14

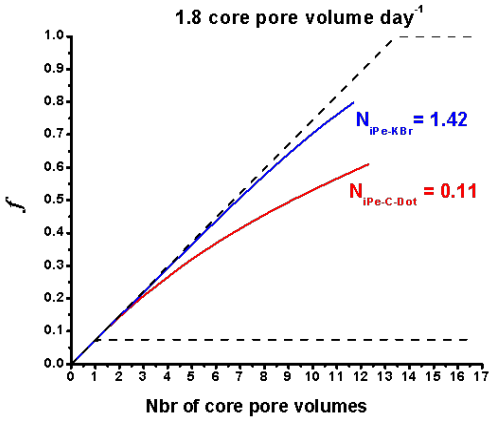

B: Reference Figure 22

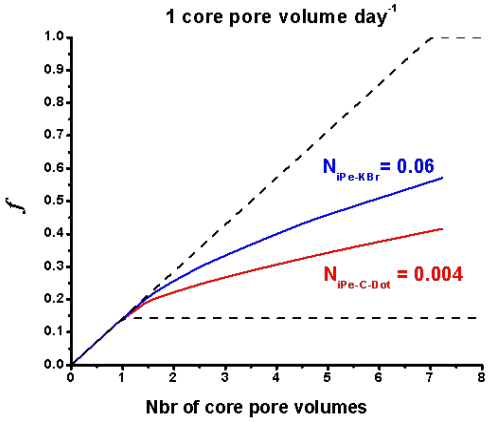

C: Reference Figure 20

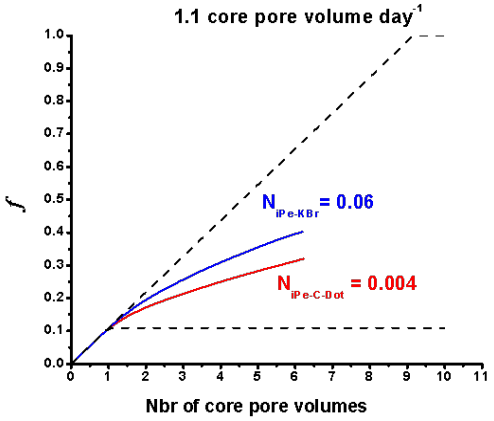

D: Reference Figure 17

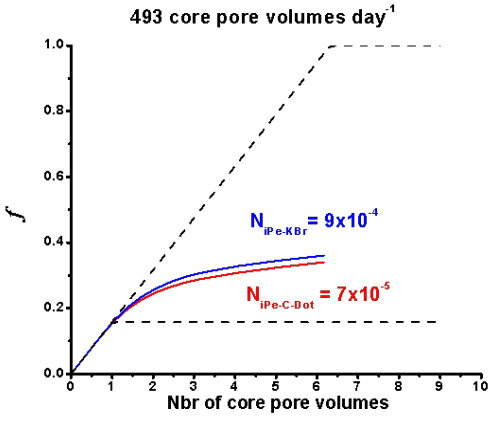

E: Reference Figure 15

Figure 26: Storage and peclet number analysis of tracer bypass for C-Dots and KBr. Figures A to E show the fraction of tracer total pore volume sequestered as a function of the number of core pore volumes and is in the decreasing order of inverse peclet number. Figure Number corresponds to breakthrough results in chapter 4

Several important features of the flow experiments are immediately apparent from Figure 26. First, except for the very fastest flow case at the bottom, the mass sequestered for bromide is more than that for C-Dots. Second, the fraction of tracer sequestered increases as the peclet number increases (e.g., is greatest for the slowest flow case at the top). Finally, Figure 26 shows that there is some tracer sequestration in the matrix even if N_{iPe} is very low (bottom panel).

The last observation might be unexpected. At very fast flow, the tracers should ignore the halo and move entirely through the channel. This will probably be the case in natural systems, but is not the case in our laboratory system because the contrast in permeability between the channel and the matrix is not big enough that flow in the matrix is negligible. The flow rate through the matrix is proportional to the permeability ratio of the core and matrix, and is independent of the flow rate through the cell. The fraction of flow through the matrix (e.g., halo or diffusion slit) is therefore not changed as the flow rate in the channel becomes very large. The rise in the tracer curves above the dashed channel box in the bottom right image of Figure 26 shows this flow in the matrix halo directly. This flow must be addressed by our modeling and we describe how this is done in the next section.

Before proceeding to describe the modeling, we would comment that plotting the tracer arrivals in the fashion illustrated in Figure 26 has proven to be very useful. For example, if the fraction of tracer sequestered is greater than 1, it is immediately apparent that the porosities for the halo or channel have been assigned incorrectly.

5.3 The Flow Model

The flow and transport of the tracers through the dual permeability core-slit and core-halo systems is modeled by calculating diffusion and flow separately using an operator splitting

approach. The fluid and tracer are moved in small discrete steps along the core channel. At each step, diffusion into the matrix is calculated using finite element methods and the concentration in the channel appropriately reduced. Longitudinal dispersion and adsorption on the solid surface are included in the channel. Dispersion is calculated in the halo using the fluid velocity profile in the halo calculated as described below. The longitudinal dispersion (D_L) is calculated from the longitudinal (core-flow parallel) true fluid velocity, v_L: $D_L=a_L\ v_L$. The transverse (perpendicular to the flow velocity) dispersion in the halo is calculated: $D_T=(a_T/a_L)\ a_L\ v_L$, where a_T/a_L is the ratio of transverse to longitudinal dispersion, usually ~0.1.

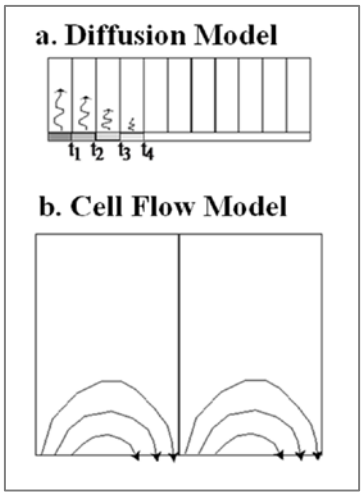

Figure 27: (a) Diffusion Model (b) Cell Flow Model

Our analysis shows that even when the slit is divided into sections by baffles, there is significant flow in the slit compartments. Flow from the channel enters the slit at the upstream end of each compartment and exits the slit at the downstream end of each compartment, as shown in Figure 27. Until the entering fluid completes its circuit through the compartment, the entering fluid carries the tracer in but the exiting fluid delivers no tracer out of the compartment. This dilutes the tracer concentration in water flowing through the channel. Our model computes this flow using the methods of Toth [45]. We calculate the flow along a number of flow

streamlines in the halo slit (as illustrated in Figure 27) and determine the time the flow takes to make the circuit along each streamline. The dilution is turned off for each streamline as the flow along that streamline completes its circuit through the compartment. The process starts when the tracer in the channel reaches each compartment by plug flow (e.g., assuming no losses by diffusion or flow have occurred to the halo- an approximation that is strictly speaking not valid but is good enough to be useful), and tapers off as each streamline in that compartment completes its circuit. The flow in the channel and halo are apportioned according to their relative permeability. The permeability of the packed beads is calculated from the porosity and the bead diameters in the channel and halo using the Carmen Kozeny equation. For the Hele Shaw cell the permeability of the square channel is the width squared divided by 32, and the permeability of the slit is its width squared divided by 12.

The model accounts for tracer adhesion using a sticking factor. We simply assume that a fraction of the tracer in the pore fluid sticks to the solid surface, and do not allow tracer to advance to the next computational node along the channel until this adsorption toll is paid. For the C-Dots and bromide ion the sticking factor is assumed to be zero, as suggested by the homogeneous column tracer experiments.

5.4 Modeling Analysis

The model described in Section 5.3 is used to interpret the experimental tracer breakthrough curves in Chapter 4. The experimental data are well matched by the model in the Hele Shaw, Rectangular Beadpack, and Plexiglass and stainless steel cylindrical column experiments. The solid model curves in Figures 29 to 37 (blue for the KBr and red for the C-Dot tracers) demonstrate the quality of the match between the experimental data and the model predictions that can be achieved with the parameters recorded in Table 7. The dashed lines (labeled no compartment flow) show the importance of taking into account flow in the matrix as is done for the solid lines. The parameters that remain to be constrained by the experimental data are the porosity of the channel and halo and the dispersion constants in the channel and halo (ϕ_c, ϕ_m, a_l, and a_T) as indicated in Table 7.

5.4.1 Diffusion Constant Variation for C-Dots

The aqueous diffusion constant of KBr is known and has a value of 2×10^{-5} cm^2 s^{-1}, as reviewed in Section 5.1. This diffusion constant matches the KBr tracer data in the Hele Shaw cell experiments (as well as the other experiments). This provides some confirmation of our methods of analysis and justifies using the Hele Shaw data and the effluent curve for the C-Dot tracer to refine the aqueous diffusion constant for the C-Dots from their size and the Stokes-Einstein equation. Figure 28 shows the best-fitting aqueous diffusion constant of the C-Dots is 1.5×10^{-6} cm^2 s^{-1}, and we use this value in the analysis of our experimental data. As reviewed above, the diffusion tortuosity of a spherical beadpack is known to be 1.5 and we use this value

in both the channel and matrix for the experiments where the apparatus was filled with glass beads. For the fracture cell tortuosity is assumed to be 1. In other words, in our interpretation of the experimental data, we assume that $D_{\infty-C-Dot} = 1.5\times10^{-6}\,\mathrm{cm}^2\,\mathrm{s}^{-1}$, $D_{\infty-KBr} = 2\times10^{-5}\ \mathrm{cm}^2\,\mathrm{s}^{-1}$, and $\tau = 1.5$ (beadpack) and $\tau = 1$ (fracture).

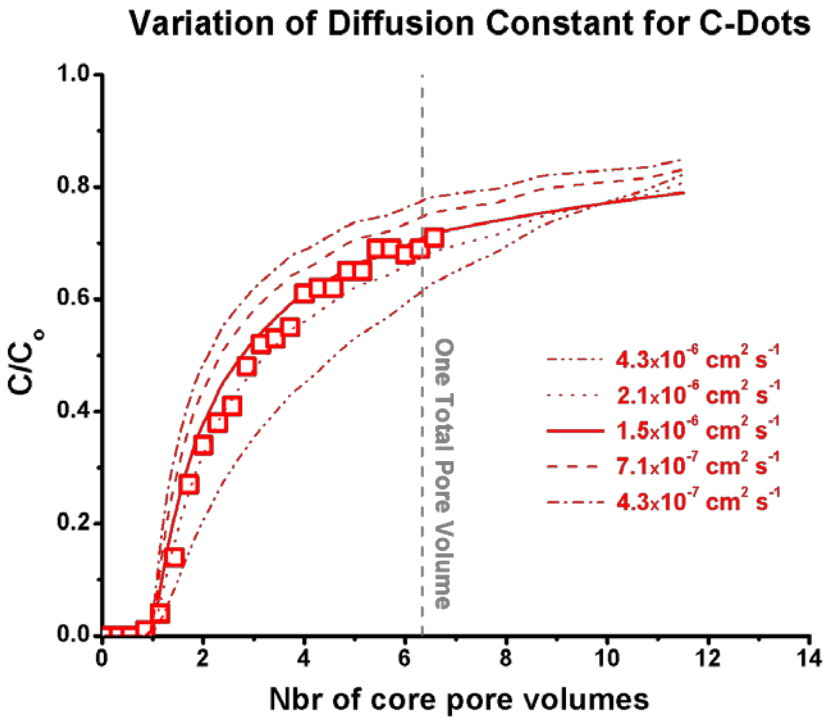

Figure 28: The Hele Shaw effluent C-Dot concentration curve indicates the best-fitting aqueous diffusion constant is 1.5x10-6 $cm^2\ s^{-1}$. This is within the range expected from the size of the particles according to the Stokes-Einstein equation and is the single value of the C-Dot diffusion constant we will use in analyzing the experimental data, and is probably the best indication of particle size.

Table 7: Modeling data and best fit parameters, Abbreviations used: C – No of compartments; Q-flowrate, τ – toruosity, Φ_c-porosity of core, Φ_h - porosity of the matrix halo, (c) – continuous, (p)-pulse injection, a_L – longitudinal dispersivity; a_L/a_T – ratio of transverse and longitudinal dispersivity

Geometry & Injection	Ref. Fig.	C	Q ($cm^3\ d^{-1}$)	τ	Φ_c (%)	Φ_h (%)	a_L (mm)	a_T/a_L
HS Cell (c)	29	13	720	1	99	30	0.1	0.1
HS Cell (c)	30	13	0.24	1	99	30	0.1	0.1
HS Cell (c)	37	13	0.6	1	99	30	0.1	0.1
Rect. Beadpack (c)	32	1	5.06	1.5	35	30	4	0.1
Rect. Beadpack (c)	31	10	5.06	1.5	30	35	4	0.1
Rect. Beadpack (p)	33	10	5.06	1.5	30	35	4	0.1
Plexi-column (c)	34	11	28.8	1.5	40	37	4	0.25
SS Column (p)	35	1	12	1.5	40	35	4	0.25
SS Column (p)	36	1	28.8	1.5	40	35	4	0.25

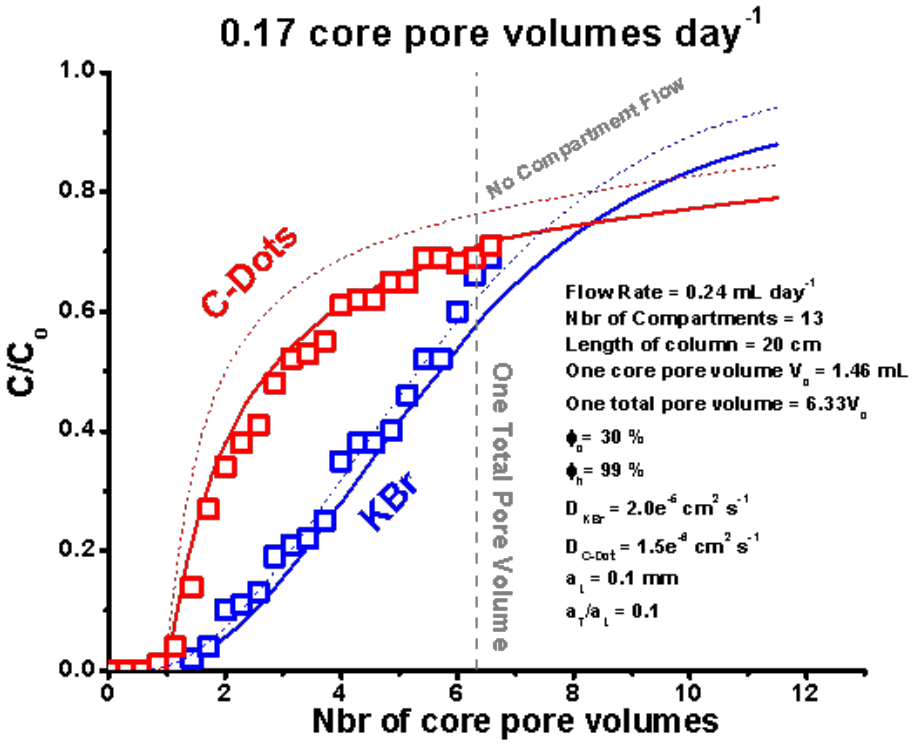

Figure 29: Hele-Shaw Fracture Cell at flow rate - 0.24 mL day^{-1}

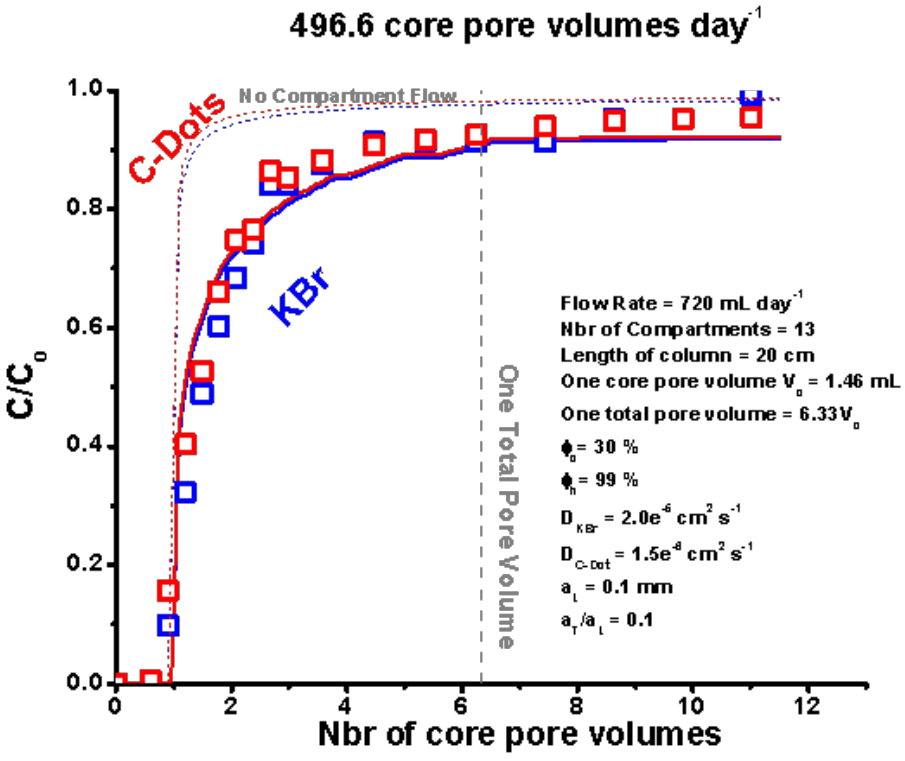

Figure 30: Hele-Shaw Fracture Cell at flow rate - 720 mL day^{-1}

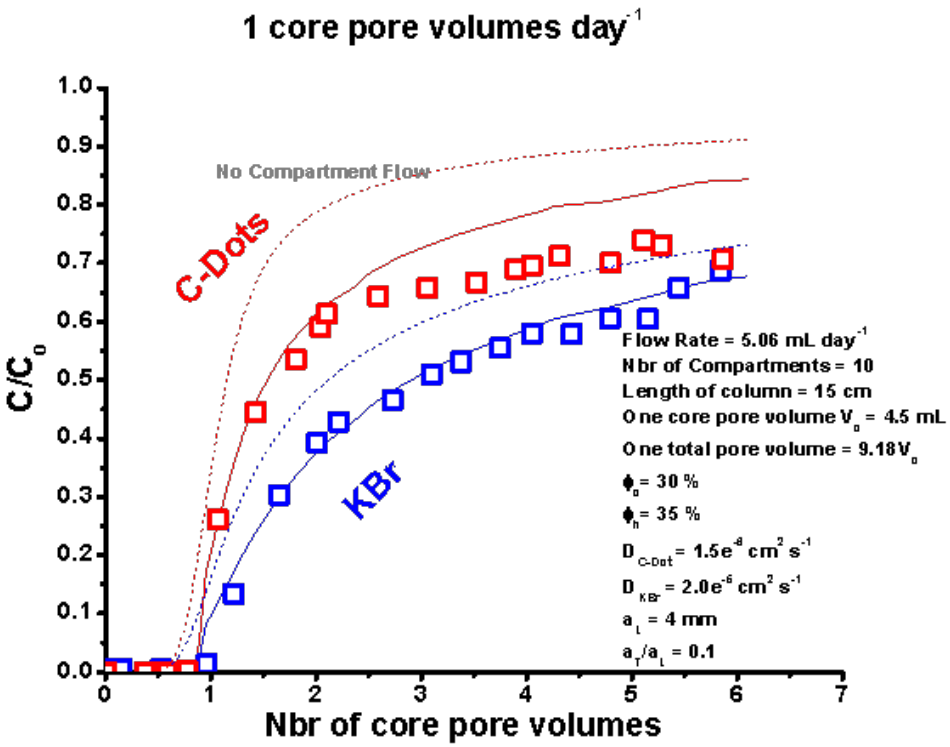

Figure 31: Rectangular Beadpack - multi compartment at 5.06 mL day^{-1}

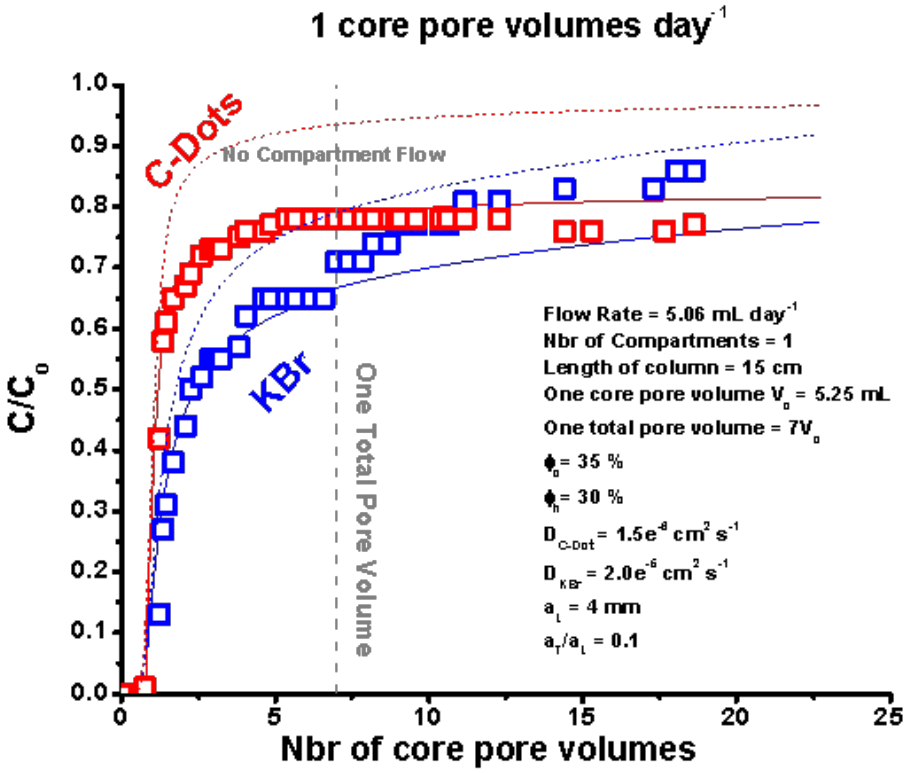

Figure 32: Rectangular Beadpack - single compartment at 5.06 mL day^{-1}

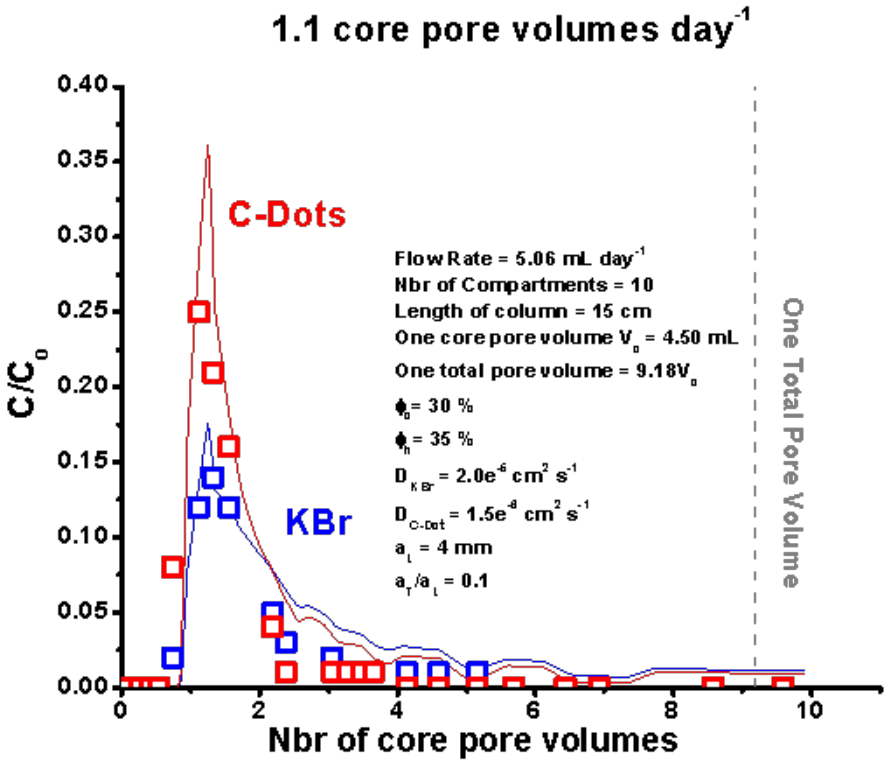

Figure 33: Rectangular Beadpack multi compartment - 5.06 mL day^{-1}

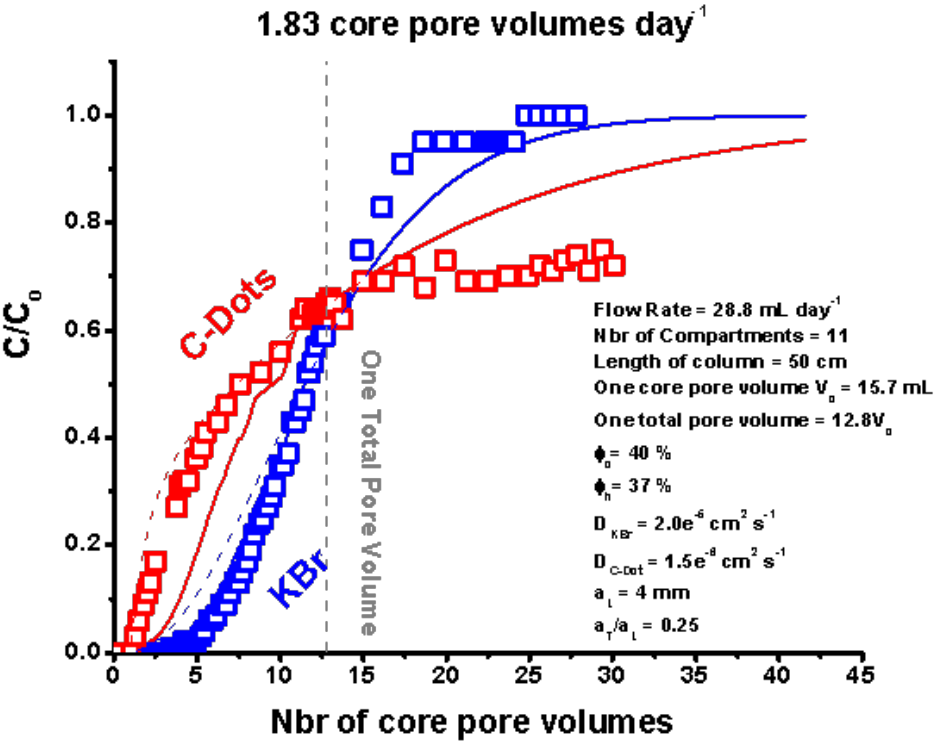

Figure 34: Plexi-Column - multi-compartment - Flow rate 28.8 mL day^{-1} with C-Dot and KBr

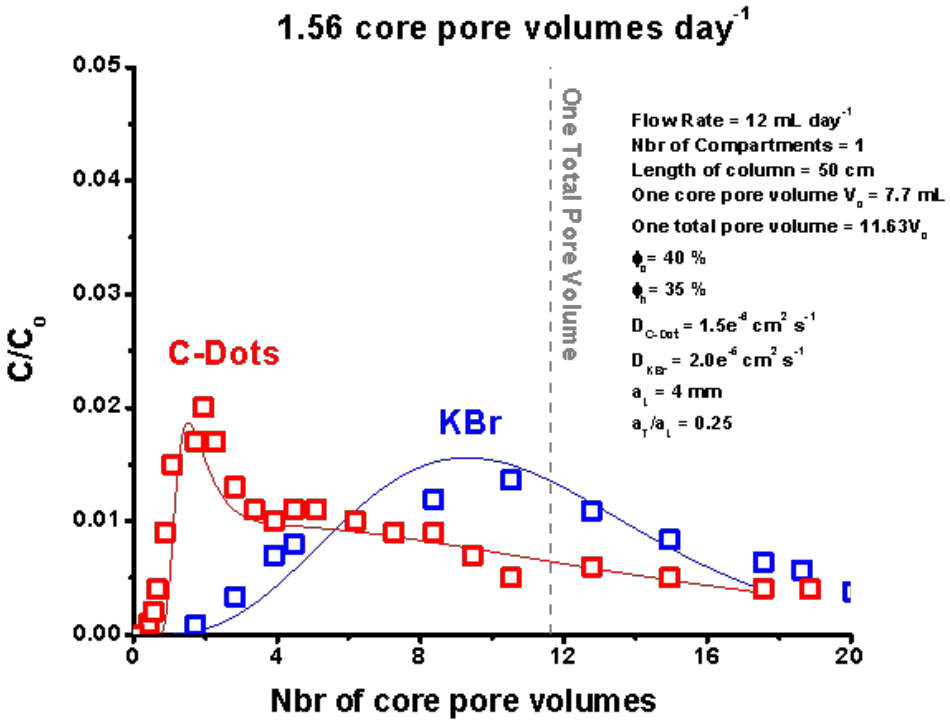

Figure 35: Pulse Injection through Stainless Steel Cylindrical Column at 12 mL day^{-1}

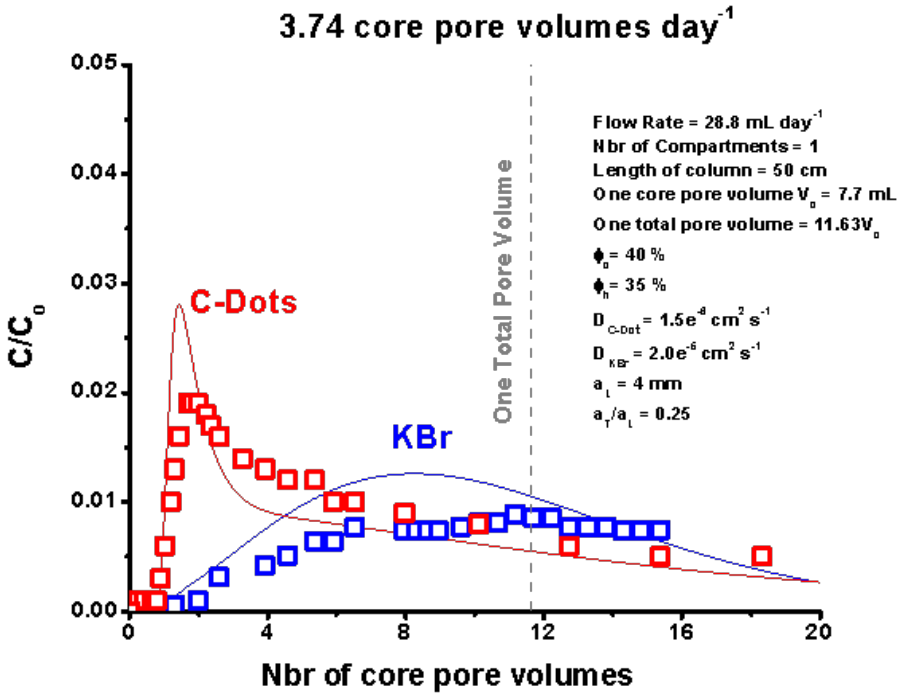

Figure 36: Pulse Injection through Stainless Steel Cylindrical Column at 28.8 mL day-^{1}

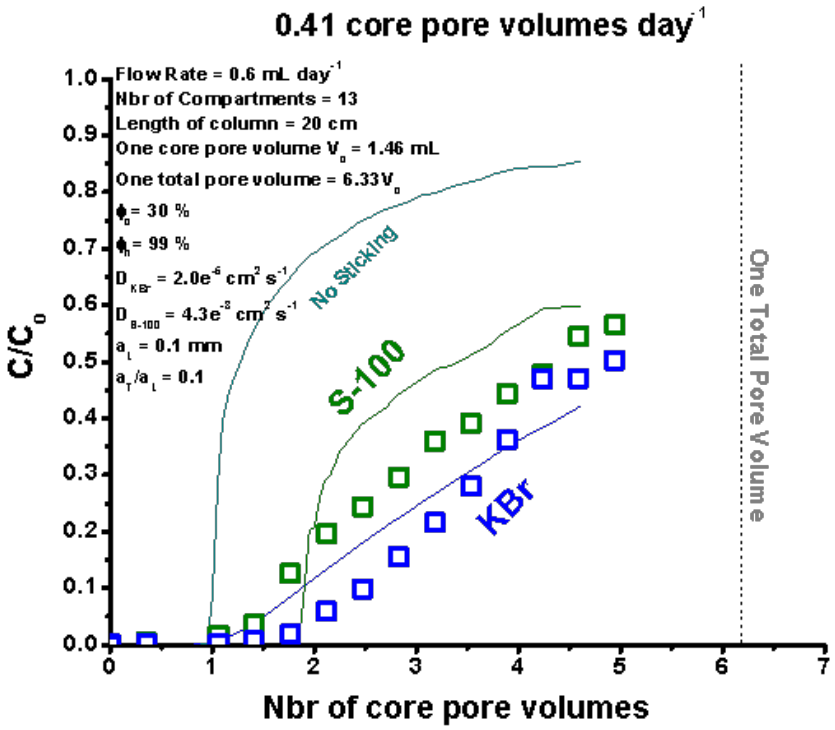

Figure 37: Hele-Shaw Cell - 0.6 mL day^{-1}

5.4.2 Hele-Shaw Cell

The model curves as seen in Figures 29, 30 and 37 fit very well with the experimental data points. Both the fast and slow flow rate fit well. The dashed lines in Figures 29 and 30 shows the importance of taking into account the flow in the halo, without which there is a significant deviation from the experimental data. The best fit data for C-Dots (Figure 28) is obtained for a diffusion coefficient of ~1.5x10^{-6} which corresponds to ~3 nm based on Stoke-Einstein Equation. From TEM image analysis we estimate the C-Dot size to be ~7 nm which corresponds to a diffusion coefficient of 6x10^{-7} cm^{2}s^{-1}. From figure 37, we observe that the S-100 particles stick as if ~80% of the injected concentration had to be adsorbed to the channel walls.

5.4.3 Rectangular Beadpack

The model curves as seen in Figures 31 and 32 fit very well with the experimental data points for continuous injection of tracers. Comparing the dotted vs solid lines in the Figures 31 and 32 again highlights the significance of flow in the halo. The pulse data (Figure 33) is simulated by same model parameters used in Figure 31 and shows an excellent fit. The longitudinal dispersivity a_L~4 mm gives the best fit to the experimental data. The best-fitting porosity of the channel is greater than the porosity in the halo in the single compartment case, whereas in the multi-compartment cases the reverse is true. As long as this is the case the curves fit the experimental data well. These cases have been highlighted in the parametric analysis for the model in the appendix section. The differences in porosity could be due to the different packing methods described in the experiment section above. In multi-compartment cell there may be more entrainment of fine glass beads into the channel because the baffles only permit fine glass bead to be packed into one compartment at a time. In the case of a single compartment this entrainment would be minimized and therefore not decrease the channel permeability so much. Intermixing has been observed while packing the columns. Quite often visible intermixing has required repacking.

5.4.4 Plexi-glass Column

The model fits well for KBr and C-Dot experimental curves as observed in Figure 34. The porosity of the core is greater than that of the beadpack and this is reasonable because it is protected (and its porosity increased) by the screen that contains it.

5.4.5 Stainless Steel Column

Both the 12 and 28.8 mL d^{-1} flow rate pulse experiment can be fit (Figures 35 and 36) by a column with 40% porosity core and a 35% porosity halo, provided the ratio a_T/a_L is 0.25. The

higher flow rate KBr data does not match the model. In all cases the model fits the early part of the breakthrough curves very well.

CHAPTER 6

SUMMARY AND DISCUSSION

We have carried out experiments at a range of flow rates and laboratory scale geometries to investigate whether dual tracer experiments can measure flow short-circuiting from channel transit times and the degree of matrix diffusion.

There has been considerable debate on the interpretation of tracer breakthrough curves in the literature and the impact of matrix diffusion on the delay in chemical tracer arrival [1, 46, 47]. Several researchers have suggested that experiments with multiple tracers of varying diffusivity are needed to better interpret matrix diffusion in fracture networks and delineate the various flow mechanisms in the heterogeneous media [46, 47]. Limited data is available in this regard. Callahan [48] and Jardine et.al [49] have combined solute ions and large molecule tracers varying in diffusivity, and several other researchers (as highlighted in the literature review) have utilized colloids and bacterial tracers but have had effluent concentrations so low that they could not be interpreted easily. In contrast, with the C-Dot-KBr experiments in the hele-shaw cell at very slow and fast flow rates (Figure 14 & Figure 15), we have been able to distinguish flow channeling from matrix diffusion without having to define a range of particle sizes (diffusion constants) in our interpreting models.

First we interpreted our experiments by constructing plots of matrix sequestration as a function of core pore volumes injected. As far as we know this kind of plot has never been constructed before, but it is clearly useful. There is greater sequestration into the matrix from the flow channels as the flow rate slows to the point that the time to fill the total pore volume with fluid approaches and becomes less than the time required for the tracer to diffuse fully into the

matrix. If this ratio is characterized by an inverse Peclet Number, the explanation for systematic changes in the sequestration plots can be clearly seen to be related to diffusion into the matrix. The plots also show however, that tracer in invading the matrix. This interpretation method shows that we must model the flow through the matrix as well as the high permeability channel. The inverse Peclet number we define can also be usefully applied to interpreting experiments reported in the literature (refer Appendix Table B.1). The analysis shows that there have been very few experiments conducted in the laboratory in which significant tracer diffusion into a matrix can be expected. This may be the reason that the phenomenon we focus on here (measuring fluid bypass with dual tracers) has not been as appreciated as fully as it might have been.

Modeling the experimental data with more sophisticated (but still approximate) finite element methods that take into account flow in the matrix, we find that we can model and explain all the experimental data quite well. It is clearly important to take into account flow in the halo (our Toth models). With this flow accounted for, all the experimental data is fit with a narrow and reasonable range of parameters as summarized at the end of the preceding section. Variations in column porosities and dispersion constants are reasonable and within the limits of the construction methods. Slight parameter differences (such as the transverse dispersion in the halo and slightly different halo and core porosities) that are required to fit the cylindrical column results probably arise from the difficulty in uniformly packing these columns because the interface between the halo and core cannot be seen during filling. The difficulty of packing may also explain the very limited laboratory experiment data available with structured heterogeneity compared to homogeneous packings.

The best fit diffusion constant for C-Dots ($1.5x10^{-6}$ cm^2 s^{-1}) suggests a particle size ~3 nm which is within the 2 to 5 nm size range indicated in TEM images of the C-Dots. The lower-than-modeled concentration of the C-Dots at the later times in the continuous injection glass bead experiments may indicate the slight sticking of the particles. The match in early times can be slightly improved by adding a small degree of sticking. The lower-than-predicted effluent concentration at the later times almost certainly indicates a slight particle loss during flow through the halo, which our model does not account for. Overall, what is remarkable is how well the data can be modeled with only minimal and reasonable variations of a common set of parameters.

For most of the experiments the C-Dot tracer performs remarkably well and provides data that is consistent across three completely different kinds of apparatus and interpretable with the same parameters and models. This is not the experience that we have seen reported in the literature before. The C-Dots in our experiments show very low retention compared to colloids transported through different porous media systems which we reviewed in the introduction. Our C-Dots are 2-5 nm in diameter and have diffusion coefficient between that of chemical (solutes, large molecules) and colloidal tracers (colloids and bacteria). Their relatively small size places them on the lower end of nanoparticle size spectrum (1-100 nm) and allows them to migrate through the smallest pores that could accommodate flow in subsurface rocks and sediments. We have examined quite a number of particles, and only these C-Dots perform well. In the next section we examine possible reasons for the remarkable success of our C-Dot particles.

Mechanisms of retention

Physical Processes

Particle retention mechanisms can be broadly classified as resulting from purely physical or physico-chemical interactions. Filtration theory explains how particles are physically trapped in a porous media, while DLVO and other theories address the physico-chemical interaction between two particles and between a particle and a mineral surface.

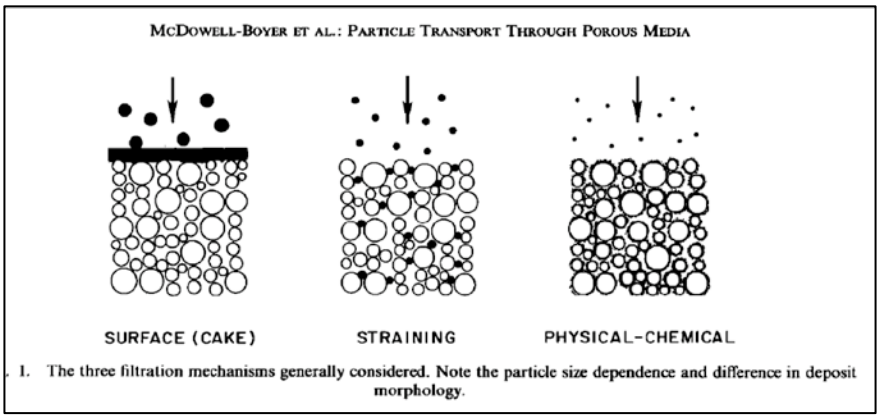

Figure 38: Filtration Mechanisms (Source: McDowell-Boyer et.al)

Filtration theory [50, 51] addresses how particles are removed as the result of settling, interception, Brownian motion, and straining, as illustrated by Figure 40 and Figure 41. Settling and interception generally decreases as the particle size becomes smaller, while Brownian motion increases with decreasing particle size. The filtration theory assumes that under favorable conditions the particles are completely removed when they contact a mineral surface. Under this principle smaller particles (<100 nm) having faster Brownian motion would contact the pore surface more frequently and would have lower mobility compared to larger particles. All factors equal, present models would predict that nanoparticles should stick more than colloid-size

particles because they are smaller. It is thus surprising that we have found the reverse appears to be the case- that our small C-Dot particles are particularly non-sticky.

On the other hand, nanoparticles should settle negligibly compared to colloidal size particles and thus be better tracers. Also, remobilization of a settled nanoparticle requires less energy. These theories are valid under certain conditions such as flow rates, the size of particles, surface functionalities or coatings [9, 52-54].

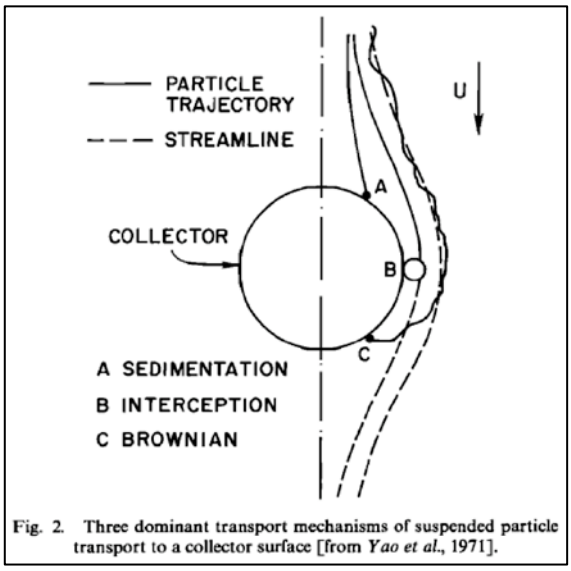

Fig. 2. Three dominant transport mechanisms of suspended particle transport to a collector surface [from *Yao et al.*, 1971].

Figure 39: Particle - Collector Surface Interaction Mechanisms (Source: Yao et.al)

Size exclusion is a phenomenon wherein the particles do not enter a pore throat due to their larger size, and are advected in the direction of the fluid flow. This is thought to be a mechanism which causes colloid-size particles to arrive earlier than expected. C-Dots have the ability to pass through most of the pores that exist in the subsurface and would not be affected by this kind of size exclusion. As observed in the literature review section, colloids do travel faster in macropores and fractures due to this volume exclusion. Although they travel faster than chemical tracers, they are highly attenuated in concentration due to filtration mechanisms. At

high flow velocities, they suffer filtration and straining in the pore throats, and for long residence times settling reduces their mobility.

In addition to size exclusion, the transport of nanoparticles could be affected by the nature of their dispersion in fractures. Larger particles tend to reflect the maximum velocity in a fracture whereas a solute tracer diffuses into the slowly flowing waters nearer the fracture walls. This is a process called Taylor's dispersion. Since the C-Dots are small compared to colloids, we would expect them to be delayed in arrival compared to colloids, because, like solutes, their Taylor dispersion would be greater than colloids. Reimus [24], demonstrated this with colloids and iodide tracers and show early arrival of colloids compared to iodide. Taylor dispersion is applicable for a single fracture and depends on the fracture aperture, length, fluid velocity and residence time. In porous media this effect is probably not significant because tortuous pathways create inter-mixing and this mixing dominates any Taylor dispersion effects (hydrodynamic separation).

Physico-Chemical Processes

The chemical interaction potential between particles and mineral surfaces is described by the DLVO theory [55] which combines the interaction potentials of Van der Waals and Electrostatic forces. The extended DLVO theory includes the effect of Born, Steric and Acid-Base interactions. Born repulsions arise out of strong repulsive forces between atoms as their electron shell begin to overlap [7]. Steric interactions arise from adsorption or chemical attachment of polymers and other long chained molecules which can stabilize or destabilize a particle suspension [7]. Acid-Base interactions characterize the hydrogen bonding properties of a surface or interacting surfaces and thus describes how that surface interacts with water [7]. Classical DLVO theory has an attractive primary minimum, a repulsive barrier and an attractive

secondary minimum. Both the Van der Waals as well as electrostatic potential profiles vary in magnitude with particle size, as is evident from the equations that describe the interaction energies. As seen in Figure 40, with decreasing particle size there is a decrease in the magnitude of both Van der Waals and electrostatic interactions. Hence, for nanoparticles the magnitudes of the potentials are small compared to that of larger colloids. Small particles tend to have almost no secondary attractive minima and the repulsive barrier is also small[7, 36].

$$V_{EDL} = 64\pi\varepsilon_0\varepsilon_r a_p (k_B T/ze)^2 \Gamma_1 \Gamma_2 \exp(-\kappa h)$$

$$V_{VDW} = -\frac{A_{123} a_p}{6h(1 + 14h/\lambda)}$$

Figure 40: Equations describing the electrostatic and Vander Waal's interactions (Source: Petosa et.al). a_p is the particle radius.

It is important to consider the chemical environment. The stability of particles is governed by the interaction potentials between particles and between particles and the pore surface. Stability of nanoparticles can be severely impacted by changes in the chemistry of the pore waters and especially counter-ion valence. Agglomerations of particles have very different characteristics from that of the original un-agglomerated nanoparticles. The larger size of the agglomerations could cause stokes settling, straining, and other filtration effects to becoming important, for example.

C-Dots with their surface functionalized hydrophilic surface might provide more stability and non-stickiness. This might explain their relatively low retention. The combination of <10 nm size, spherical shape and closeness to the molecular size range gives some unique properties to C-Dots which might eliminate any physical retention mechanisms as well offer stability and non-

stickiness. Within the nano domain (1-100 nm), studies done by Kobayashi et.al [56] have shown that, all conditions being the same and chemistry being the same, smaller particles are more stable than larger ones. They found 30 nm particles to have relatively less aggregation compared to larger particles, under strong ionic conditions. The stability of the smaller particles was explained by the interfacial interactions such as hydration forces. Hence we can expect more stability as we decrease the size of the particles and this might be the reason that our C-Dots perform so well. Since most of the particle-particle interactions are also applicable for particle-surface interactions, the small size could explain the stability and non-stickiness of the C-Dots. Unlike several nanoparticles which are tagged with molecular fluorophores for detection, the C-Dots are inherently photoluminescent which eliminates any potential interactions that are governed by the fluorophores.

Our experiments have been carried out in low salinity DI water pore solution and at close to pH 7. Perhaps this might explain the unfavorable sticking conditions which exist and make the C-Dots relatively mobile. The stability at a zeta potential close to zero (-5 mV) combined with the small size might explain why they are relatively non-sticky compared to silica nanospheres tested in our experiments.

CHAPTER 7

CONCLUSIONS AND RECOMMENDATIONS

Tracer experiments carried out in dual-permeability beadpack columns and single fracture Hele-Shaw cells have demonstrated that flow channeling and matrix diffusion can be measured by comparing the arrival curves of an inert bromide tracer and carbon based 2-5 nm sized particles. The fluid residence times in our experiments were much longer than in previous laboratory scale literature studies (literature flow rates are least 10-100 times faster than ours). The degree of bypass is immediately sequestration plots and changes in the nature of these plots are readily explained by changes in an inverse Peclet number that characterizes the experiment and reveals the extent of fracture – controlled flow. The storage plots indicate that flow is occurring in the matrix as well as the high permeability channel. Refined interpretation is possible with finite element models, and models that take into account matrix flow are shown to match the experimental data well. These methods can be immediately transferred to the interpretation of field experiments. The lab data together with two successful field experiments [25, 40] give strongly suggest that nanoparticles can be used to measure fluid bypass in the field. The small size of our C-Dot particles appears to allow them to avoid sticking and filtration and explain the high recoveries obtained in our experiments.

For the future, the main need is to understand better the reasons that nanoparticles do not stick. Nanoparticles of different sizes (within 1-100 nm domain) but with same surface charge and chemistry should be explored to evaluate effect of size on the retention under constant geochemical conditions. Pore Water Geochemistry plays a significant role in the stability and retention of nanoparticles by sticking. Our experiments have been carried out in low salinity DI

water pore solution and at close to pH 7. Particle stickiness as a function of fluid parameters such as pH, Ionic strength and concentration and charge of specific counter-ions could give more insight into the stability and transport of C-Dots. Glass beads are a poor proxy for carbonates, silicates and clays. Stickiness should be investigated for a wide range of minerals.

Special surface coatings that add a layer of molecular chains (steric) as well as tunable charge (electrostatic) can significantly enhance the stability of the particles, and this enhancement is more significant for smaller particles (sub 10 nm) than particles which are larger. Studies have shown that these kinds of coatings can reduce sticking to surfaces[8]. A more detailed study in various degrees of favorable sticking conditions and surface coated C-Dots might help in better understand the stability and non-sticky nature of 1-10 nm sized particles. As highlighted by Petosa et.al [36], there is a need to bridge the gap between the theories applied to colloids and molecules to better understand and evaluate the stability and transport of nanoparticles in the 1-10 nm size range.

The use of nanaparticles to identify flow in natural fractures and sediments would find many applications in enhanced oil recovery, geothermal engineering, soil science. Defining matrix diffusion and storage would find applications in contaminant transport, radionuclide waste management. Knowing the nature of flow in the subsurface by defining fracture flow would enable better subsurface flow engineering and remediation. For all these reasons the ultimate goal must be to run dual tracer nanoparticle experiments in the field. A principle goal must be to create field-capable nanoparticle tracers. The relatively low retention of inert C-Dots (compared to other literature studies) and the evaluation of fluid bypass in the lab scale in this study gives us significant encouragement that such efforts will be successful.

APPENDIX A: PARAMETRIC ANALYSIS

Appendix A presents four summary Tables A.1 to A.4 and 56 plots (Figure A.1 to Figure A.56) documenting how the experiments constrain the porosity of the core and halo, the longitudinal dispersivity in the channel, and the transverse dispersivity in the matrix halo. Each table cell has a reference parametric figure number inserted for reference. The best-fitting matrix halo porosity (Φ_h) ranges from 30 to 37%. The best-fitting core porosity (Φ_c) varies with experiment type and number of compartments between 30 and 40% and is less well constrained than the halo porosity. The longitudinal dispersion parameter is 0.1 mm for the Hele Shaw experiments and 4 mm for all the experiments involving glass beads. This dispersion in the Hele Shaw case is constrained only by high flow rate C-Dot and KBr experiment, as expected from Equation 2. The longitudinal dispersion in the bead experiments is constrained best by the C-Dots in pulse experiments. The same is true for the a_T/a_L ratio. Overall, most of the cases are well constrained. The cases which are not as well constrained are highlighted in blue and italics.

1. **Effect of Toth flow**

   Toth flow has been highlighted in the model plots and this accounts for the flow in the halo which is significant in our experiments. The toth flow is included for all the parametric cases studied. No toth flow cases have been highlighted in the best fit model results under Interpretation section

2. **Effect of Longitudinal Dispersivity (a_L)**

We observe the increase in longitudinal dispersivity tends to dilute the concentration of the tracers. The C-Dot tracer seems to be more sensitive to change in dispersivity, especially at slower flow rates in the rectangular beadpacks. Exceptionally slow flow rates (Hele-Shaw Cell) does not show any impact of longitudinal dispersivity and seems to be not so well constrained.

3. **Effect of Transverse Dispersivity (a_T/a_L)**

In all geometries, the effluent concentration drops with increasing transverse dispersion tends to reduce the concentration of the tracers. For instance, in the Hele-Shaw Cell, the transverse dispersivity is not well constrained at slow flow rate case but at high flowrate, we see decrease in effluent concentration with increasing transverse dispersion as expected with both tracers having the same trend. KBr tracer seems to have lesser impact in high residence time experiments as observed by the slow flow rate experiments in the stainless steel cylindrical column tests.

4. Effect of Core Porosity

Increase in core porosity increases the transit time in the core. For instance, in the rectangular beadpacks, we notice that there is some early arrival difference in the breakthrough curves and shifts the curves to the right for both tracers. Except the C-Dot and KBr, tracers in the plexi-glass column tests and Kbr tracer in rectangular beadpack (Figures A.22, A.37 and A.38) all the cases are well constrained.

5. Effect of Halo Porosity

High halo porosity increases the diffusion through the halo thereby impacting KBr breakthrough more than the C-Dot tracers as observed in all the cases. Decreasing halo porosity leads to early arrival (Beadpacks and Cylindrical Columns).

Table A.1: Hele-Shaw Cell model parameters. Reference figure numbers are inserted in parenthesis. Not well constrained cases are in italics and blue

Parameter	**Hele-Shaw Cell**			
Q (mL /day)	0.24		720	
Tracer	KBr	C-Dot	KBr	C-Dot
Φ_c	99	99	99	99
Φ_h	30	30	30	30
a_L (mm)	0.1 *(A.2)*	0.1 *(A.1)*	0.1 (A.6)	0.1 (A.5)
a_T/a_L	0.1 *(A.4)*	0.1 *(A.3)*	0.1 (A.8)	0.1 (A.7)

Table A.2: Rectangular beadpack model parameters. Reference figure numbers are inserted in parenthesis. Not well constrained cases are in italics and blue

Parameter	**Rectangular Beadpack-10C**				**Beadpack HS-1C**	
Q (mL /day)	5.06 - pulse		5.06		5.06	
Tracer	KBr	C-Dot	KBr	C-Dot	KBr	C-Dot
Φ_c	30 (A.14)	30 (A.13)	30 *(A.22)*	30 (A.21)	35 (A.30)	35 (A.29)
Φ_h	35 (A.16)	35 (A.15)	35 (A.24)	35 (A.23)	30 (A.32)	30 (A.31)
a_L (mm)	4 (A.10)	4 (A.9)	4 (A.18)	4 (A.17)	4 (A.26)	4 *(A.25)*
a_T/a_L	0.1 (A.12)	0.1 (A.11)	0.1 (A.20)	0.1 (A.19)	0.1 *(A.28)*	0.1 (A.27)

Table A.3: Plexi-glass cylindrical column model parameters. Reference figure numbers are inserted in parenthesis. Not well constrained cases are in italics and blue

Parameter	**Plexi Column**	
Q (mL /day)	28.8	
Tracer	KBr	C-Dot
Φ_c	40 *(A.38)*	40 *(A.37)*
Φ_h	37 (A.40)	37 (A.39)
a_L (mm)	4 *(A.34)*	4 (A.33)
a_T/a_L	0.25 *(A.36)*	0.25 (A.35)

Table A.4: Stainless Steel column model parameters. Reference figure numbers are inserted in parenthesis. Not well constrained cases are in italics and blue

Parameter	**SS Cylindrical Column**			
Q (mL /day)	12		28.8	
Tracer	KBr	C-Dot	KBr	C-Dot
Φ_c	40 (A.46)	40 (A.45)	40 (A.54)	40 (A.53)
Φ_h	35 (A.48)	35 (A.47)	35 (A.56)	35 (A.55)
a_L (mm)	4 *(A.42)*	4 (A.41)	4 *(A.50)*	4 (A.49)
a_T/a_L	0.25 *(A.44)*	0.25 (A.43)	0.25 *(A.52)*	0.25 (A.51)

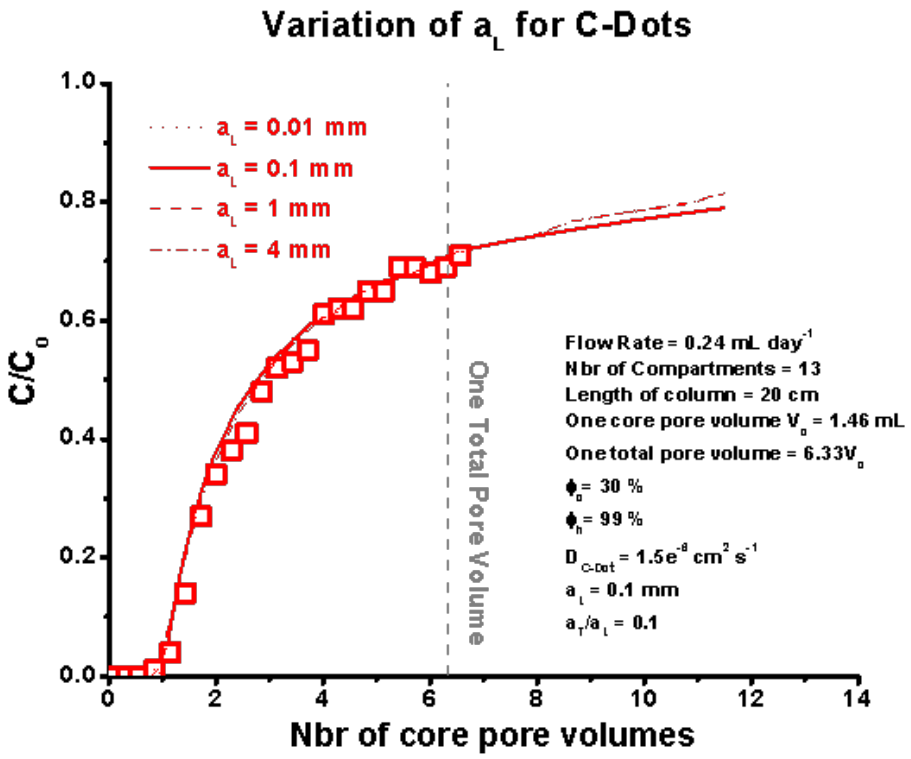

Figure A.1: Hele-Shaw Cell (slow flow) - Variation of a_L for C-Dots

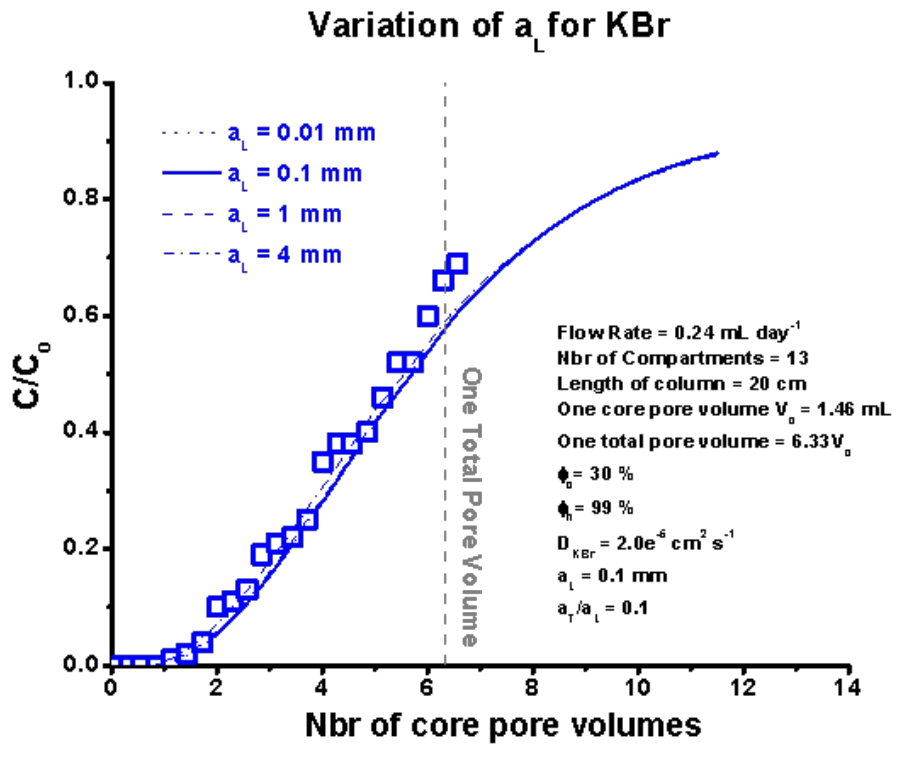

Figure A.2: Hele-Shaw Cell (slow flow) - Variation of a_L for KBr

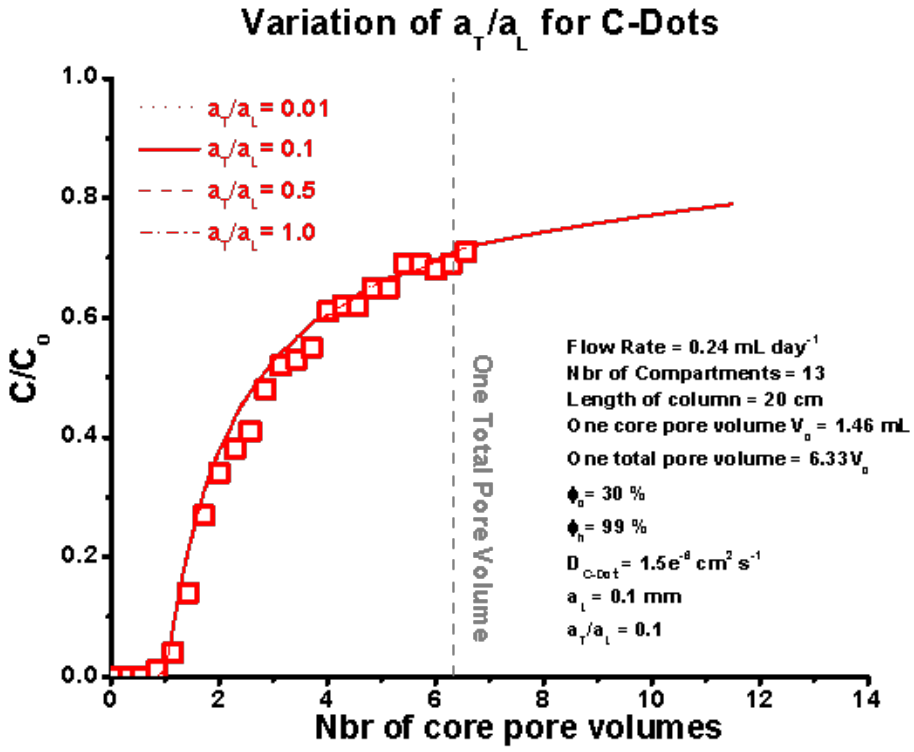

Figure A.3: Hele-Shaw Cell (slow flow) - Variation of a_T/a_L for C-Dots

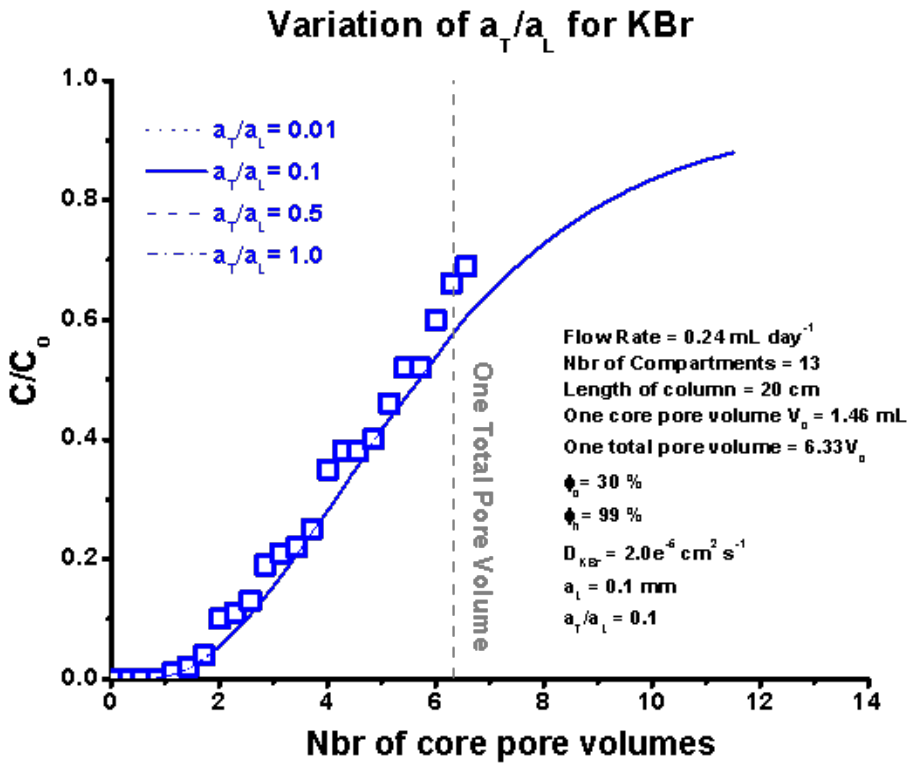

Figure A.4: Hele-Shaw Cell (slow flow) - Variation of a_T/a_L for KBr

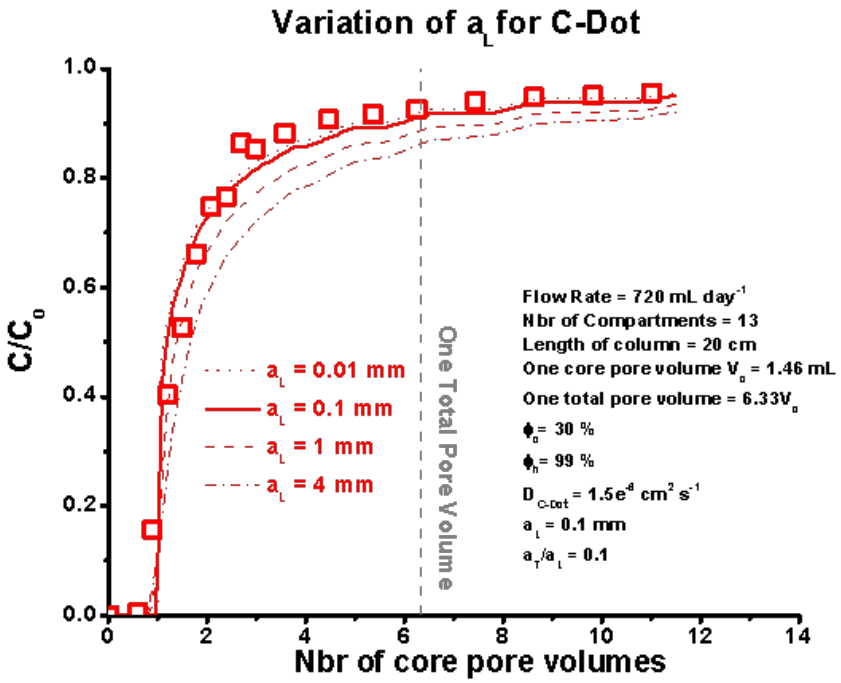

Figure A.5: Hele-Shaw Cell (fast flow) - Variation of a_L for C-Dots

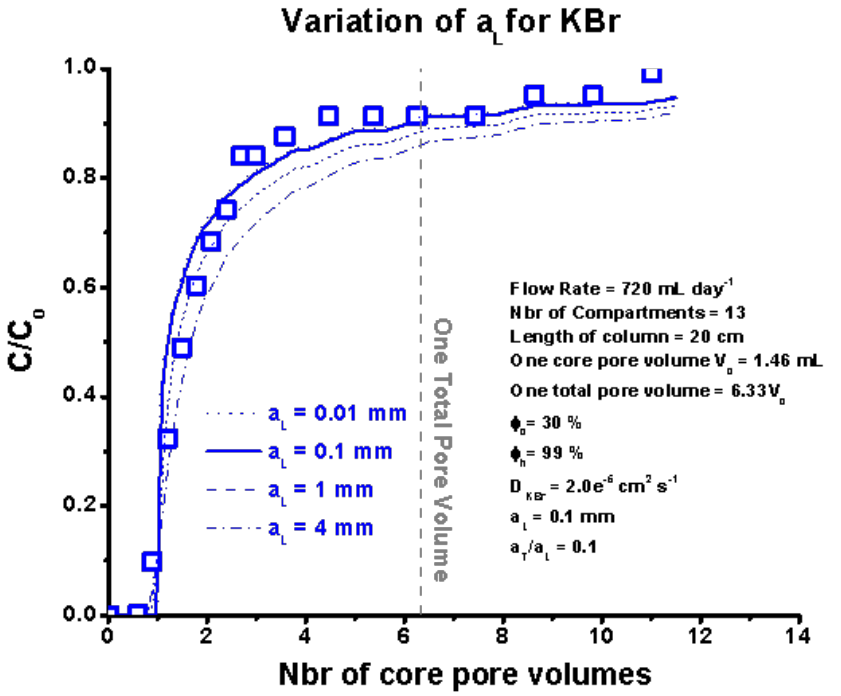

Figure A.6: Hele-Shaw Cell (fast flow) - Variation of a_L for KBr

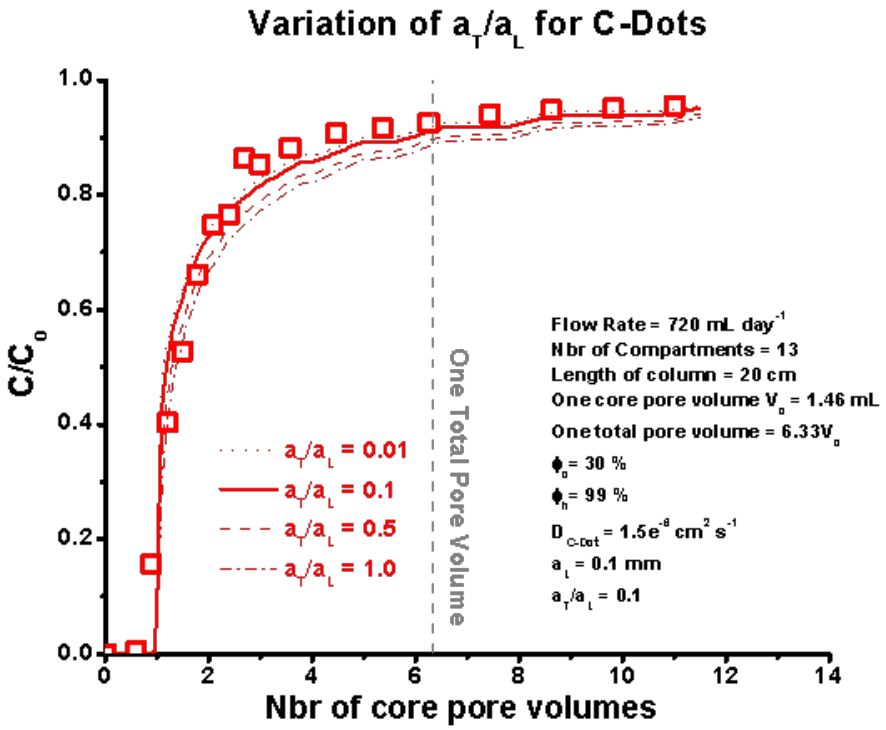

Figure A.7: Hele-Shaw Cell (fast flow) - Variation of a_T/a_L for C-Dots

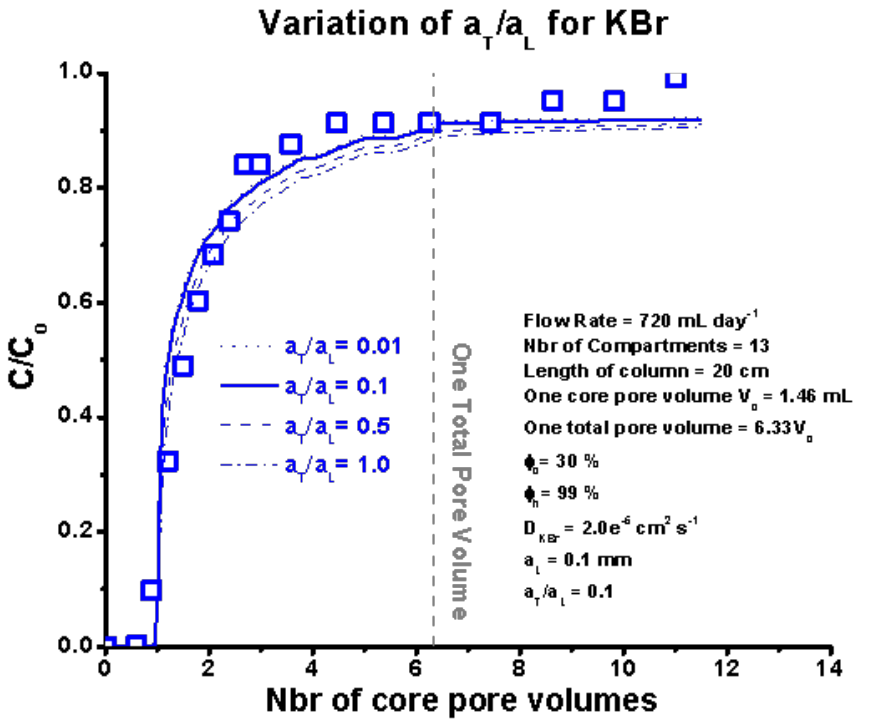

Figure A.8: Hele-Shaw Cell (fast flow) - Variation of a_T/a_L for KBr

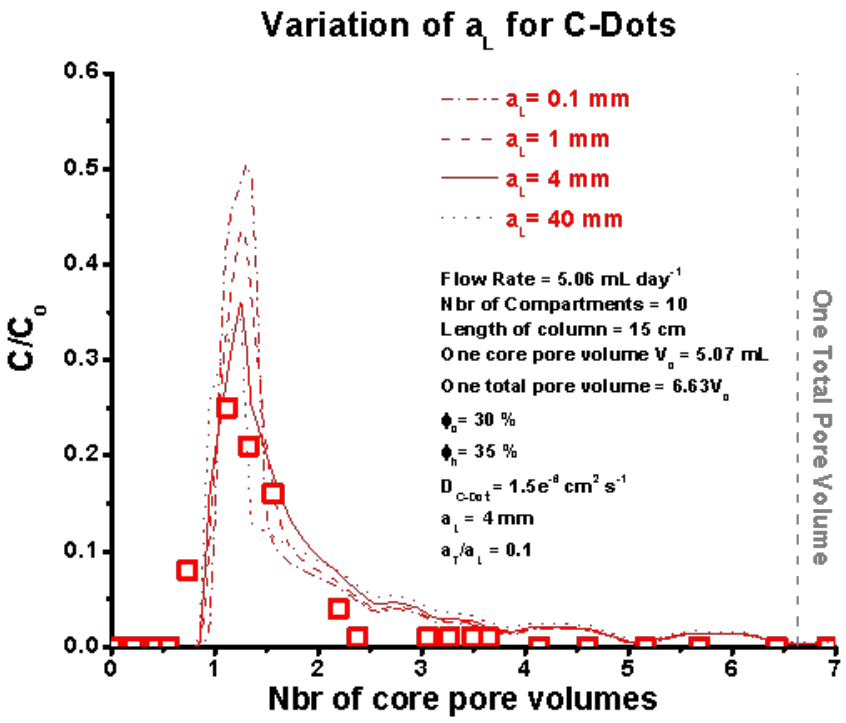

Figure A.9: Rectangular Beadpack (10 Compartment, Pulse) - Variation of a_L for C-Dots

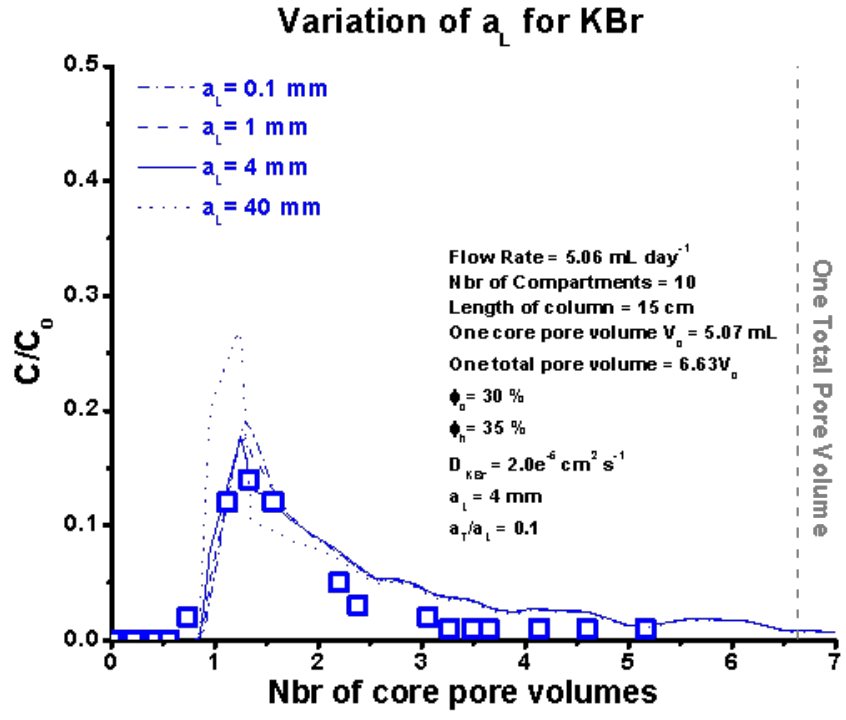

Figure A.10: Rectangular Beadpack (10 compartment, Pulse) - Variation of a_L for KBr

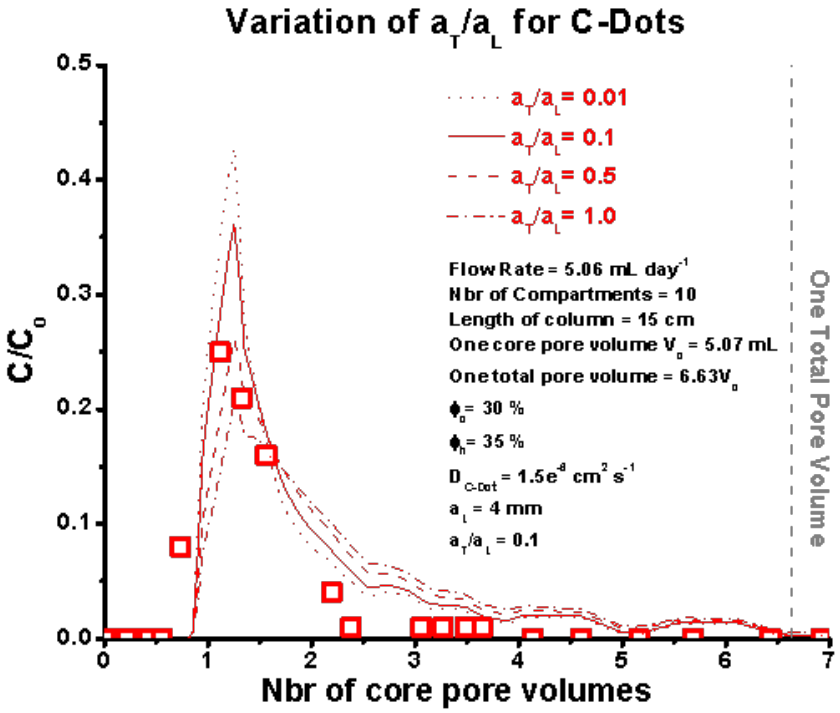

Figure A.11: Rectangular Beadpack (10 Compartment, Pulse) - Variation of a_T/a_L for C-Dots

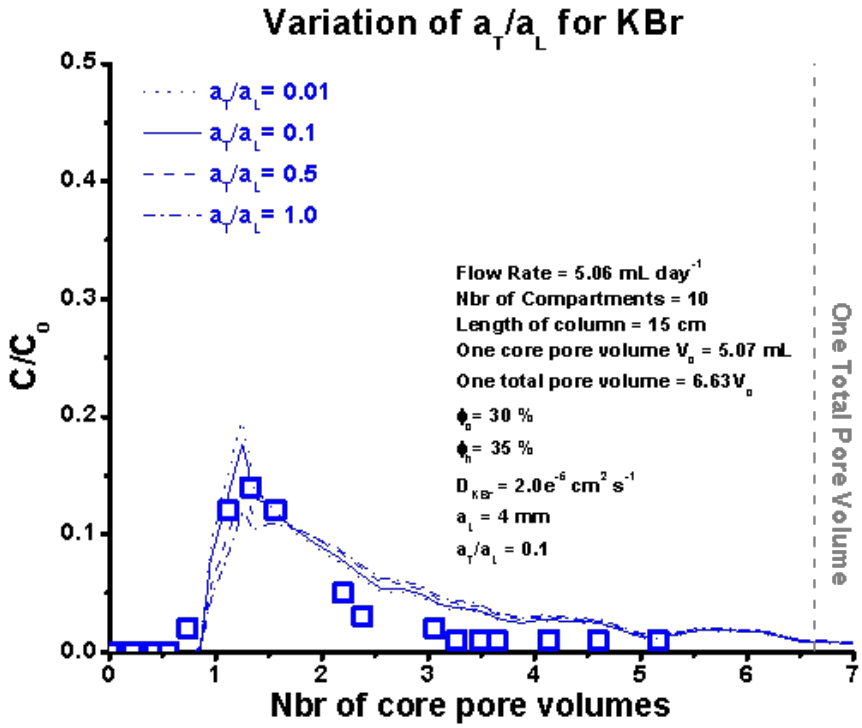

Figure A.12: Rectangular Beadpack (10 Compartment, Pulse) - Variation of a_T/a_L for KBr

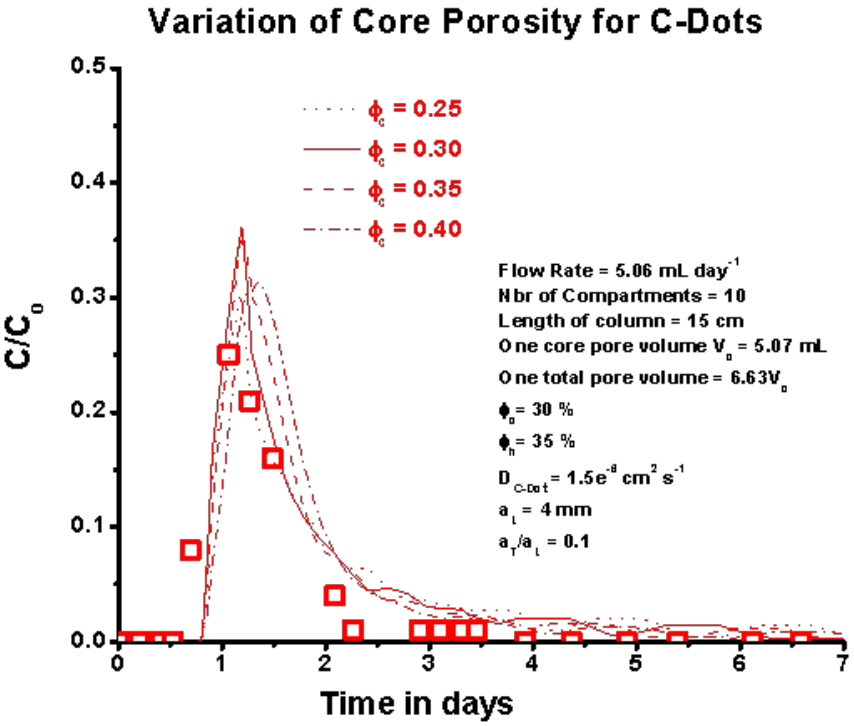

Figure A.13: Rectangular Beadpack (10 Compartment, Pulse) - Variation of core porosity for C-Dots

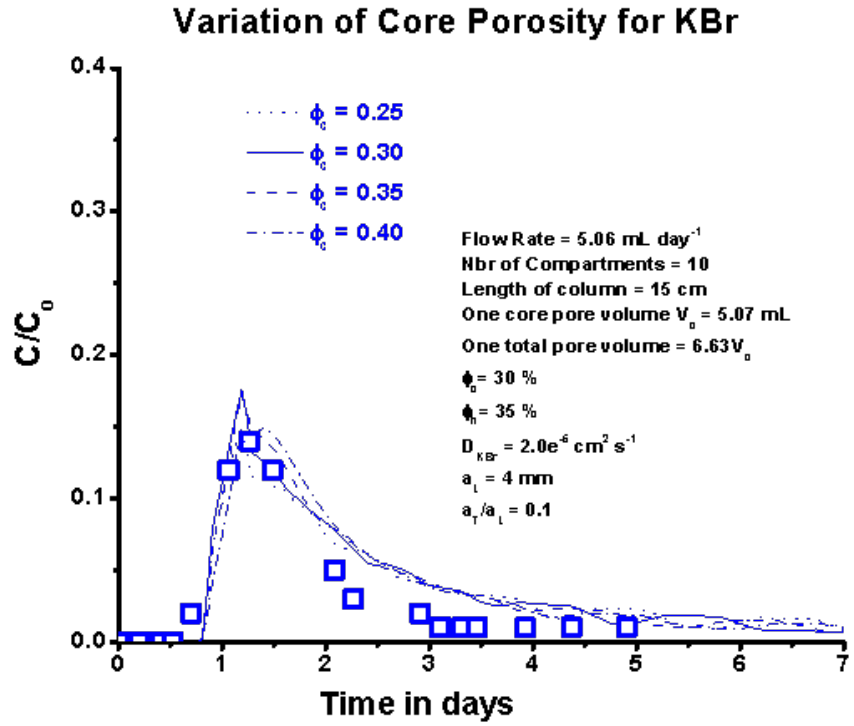

Figure A.14: Rectangular Beadpack (10 Compartment, Pulse) - Variation of core porosity for KBr

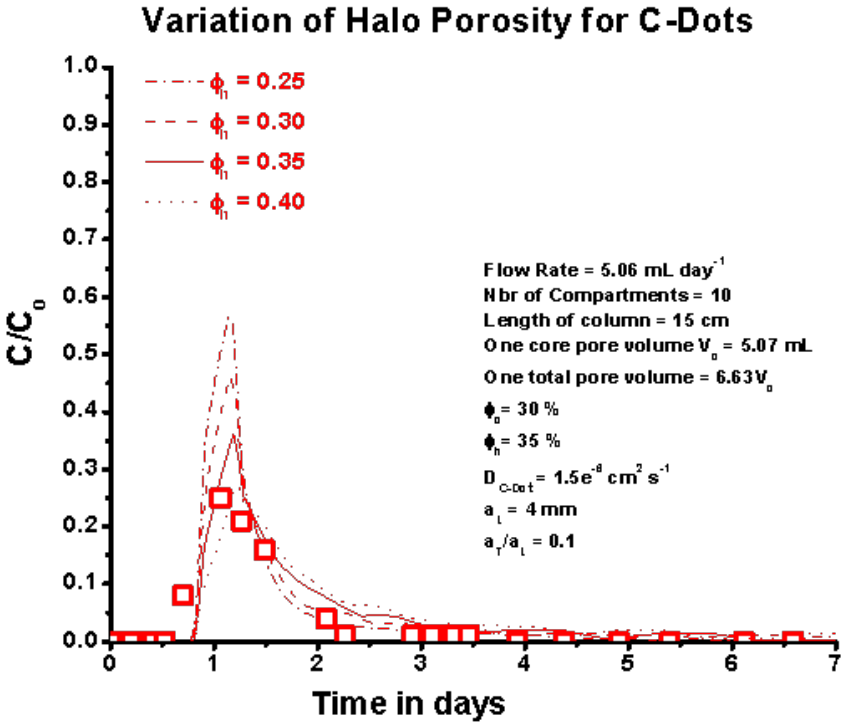

Figure A.15: Rectangular Beadpack (10 Compartment, Pulse) - Variation of halo porosity for C-Dots

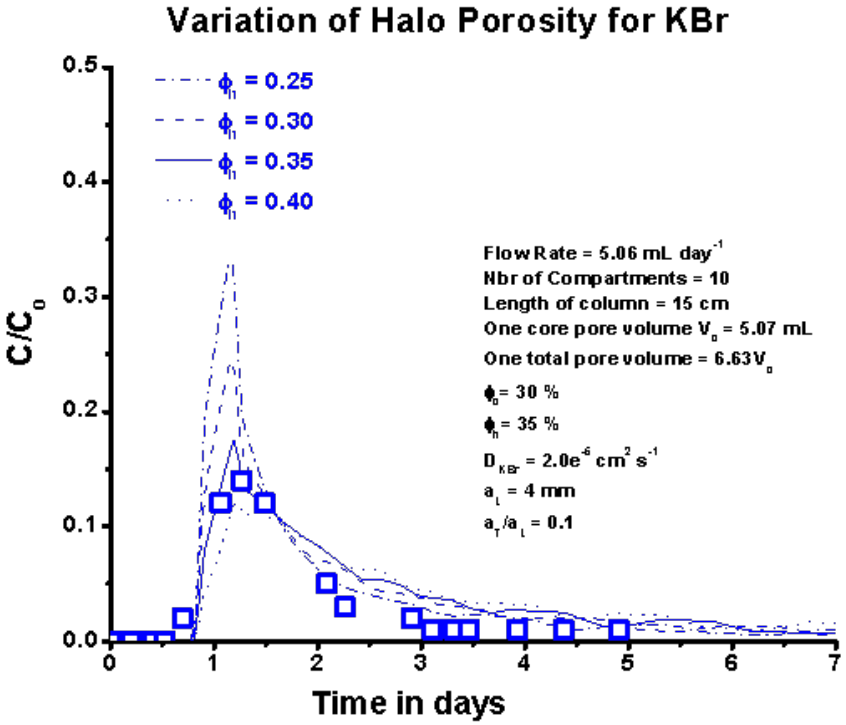

Figure A.16: Rectangular Beadpack (10 Compartment, Pulse) - Variation of halo porosity for KBr

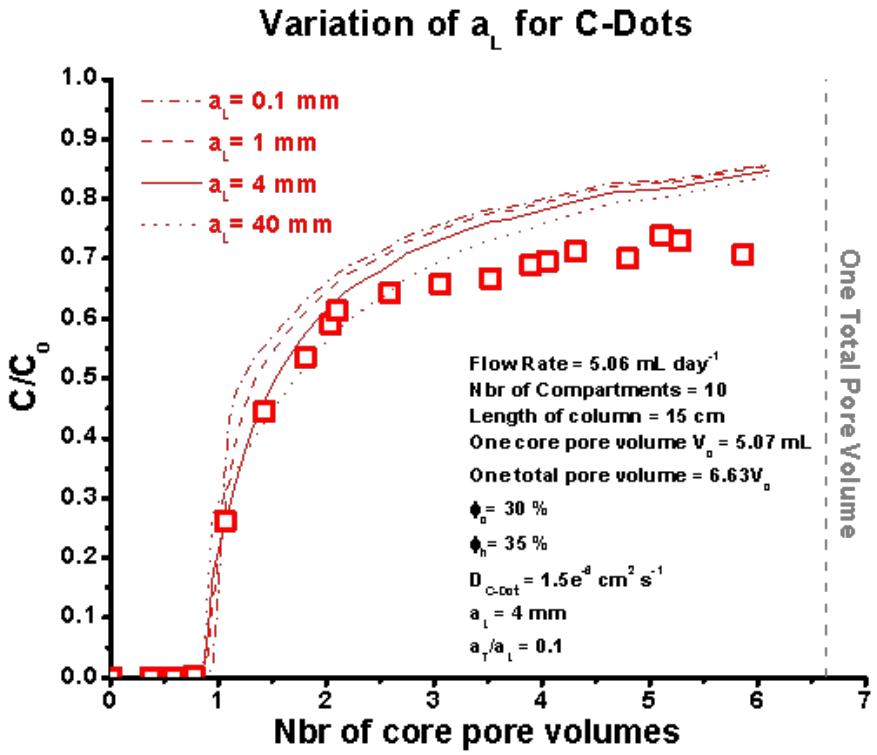

Figure A.17: Rectangular Beadpack (10 Compartment) - Variation of a_L for C-Dots

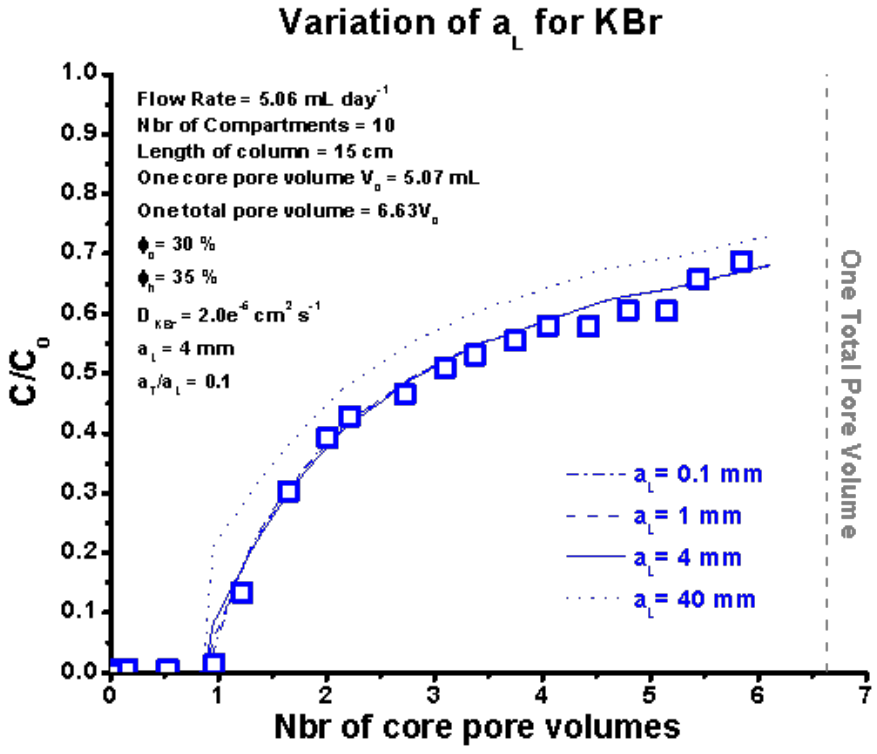

Figure A.18: Rectangular Beadpack (10 Compartment) - Variation of a_L for KBr

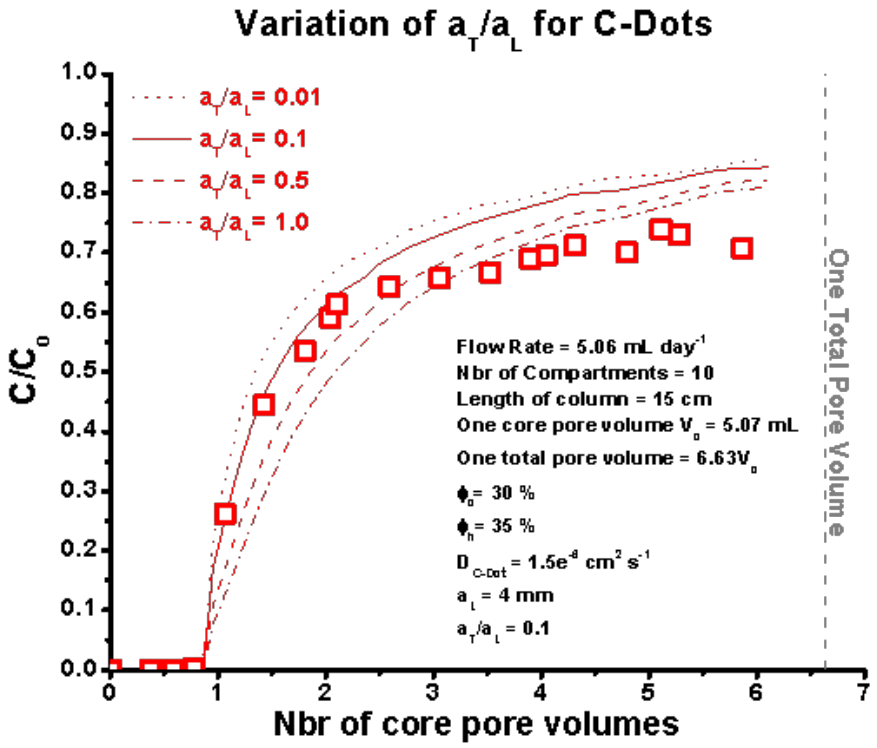

Figure A.19: Rectangular Beadpack (10 Compartment) - Variation of a_T/a_L for C-Dots

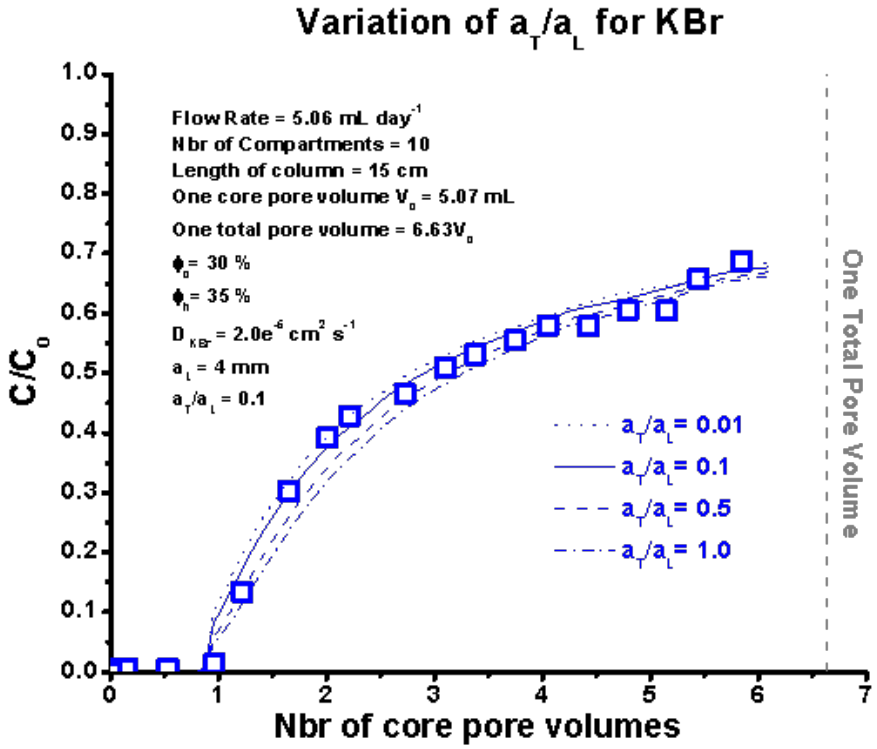

Figure A.20: Rectangular Beadpack (10 Compartment) - Variation of a_T/a_L for KBr

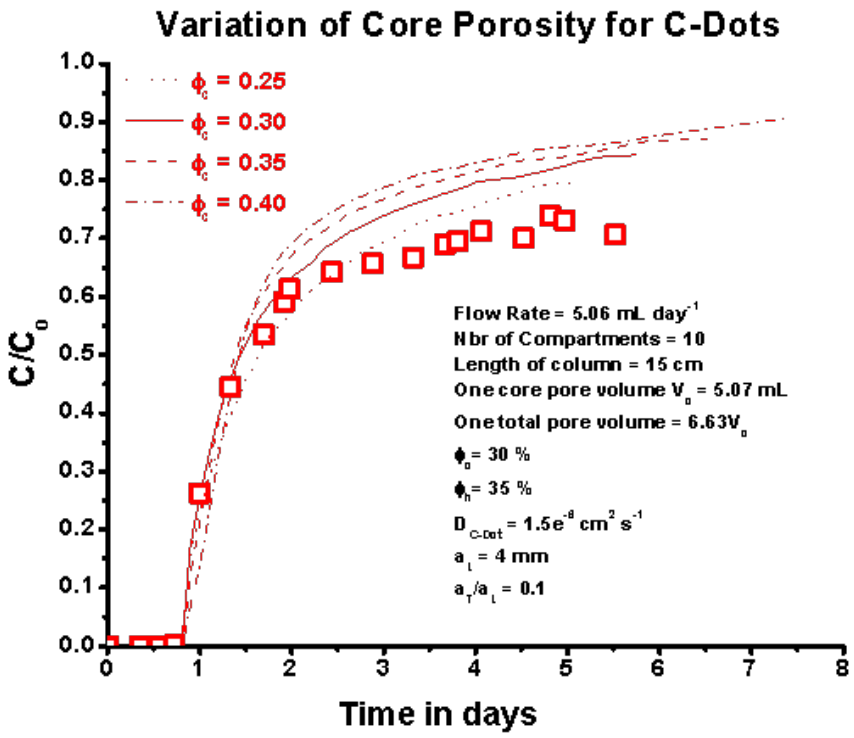

Figure A.21: Rectangular Beadpack (10 Compartment) - Variation of core porosity for C-Dots

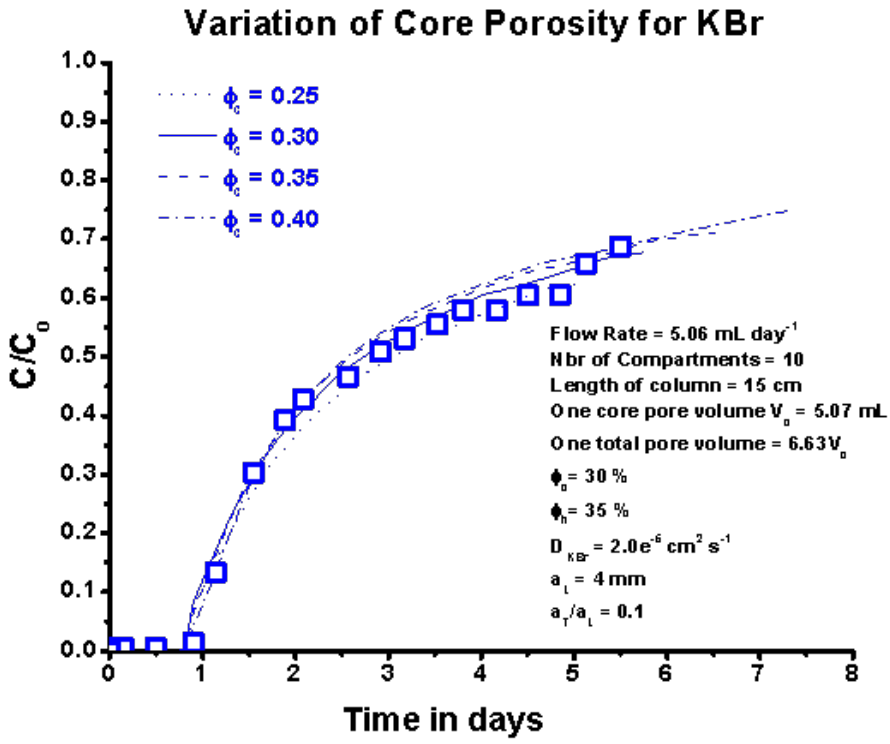

Figure A.22: Rectangular Beadpack (10 Compartment) - Variation of core porosity for KBr

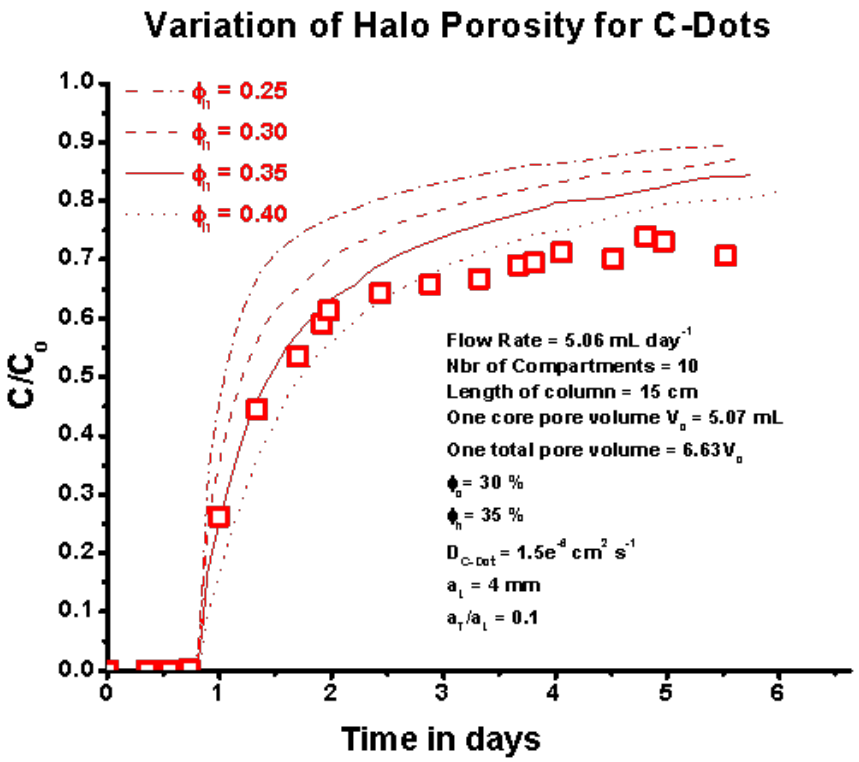

Figure A.23: Rectangular Beadpack (10 Compartment) - Variation of halo porosity for C-Dots

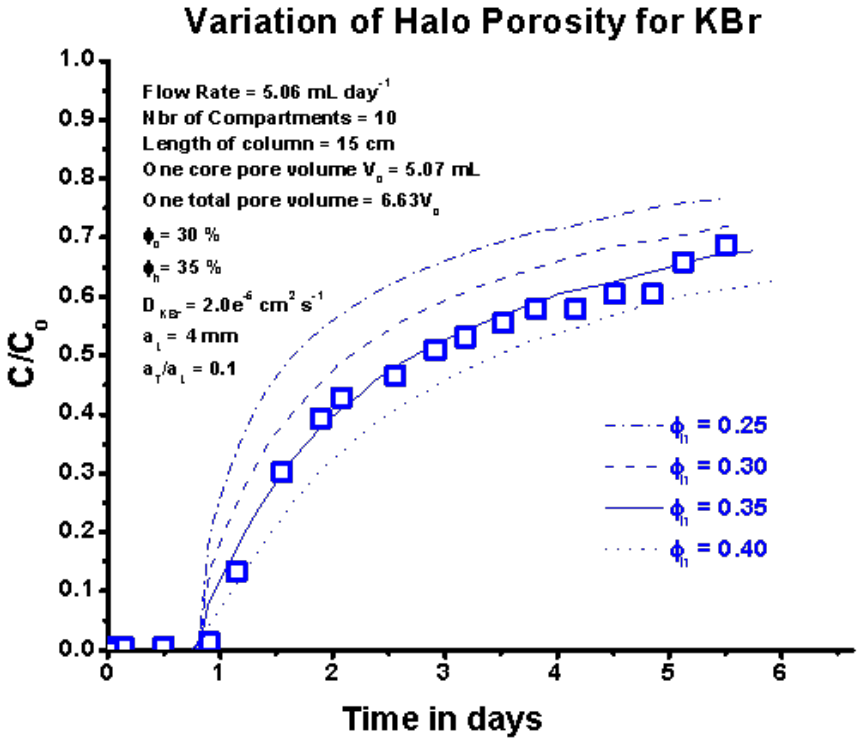

Figure A.24: Rectangular Beadpack (10 Compartment) - Variation of halo porosity for KBr

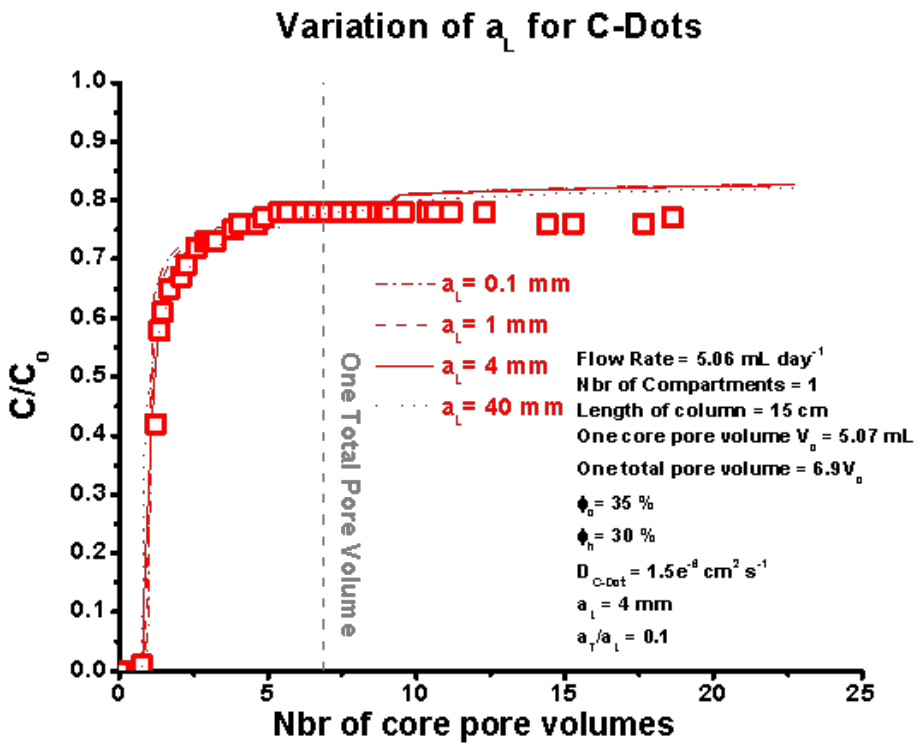

Figure A.25: Rectangular Beadpack (1 Compartment) - Variation of a_L for C-Dots

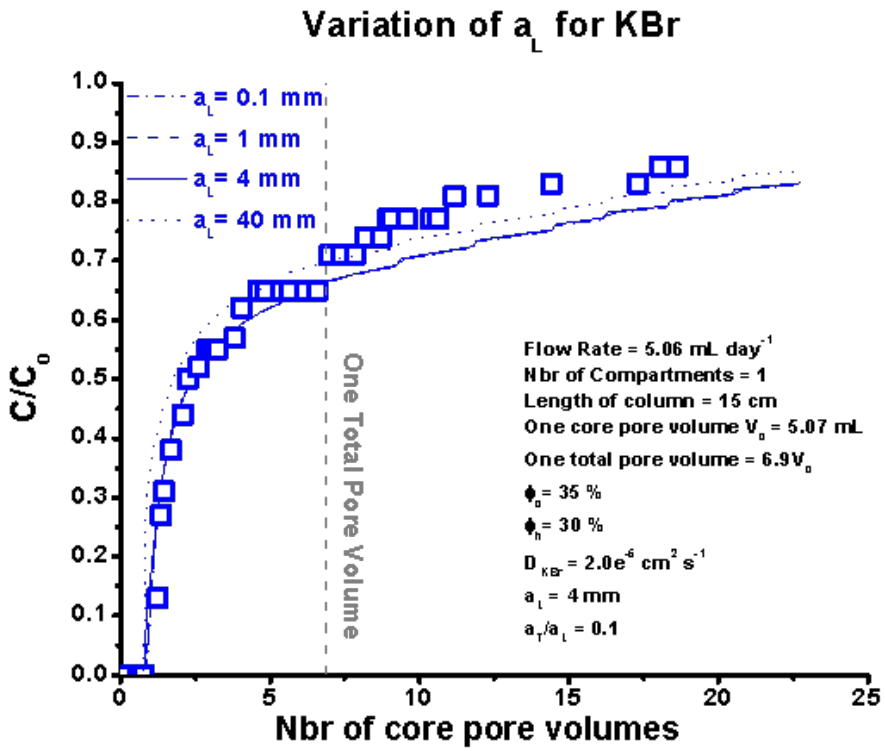

Figure A.26: Rectangular Beadpack (1 Compartment) - Variation of a_L for KBr

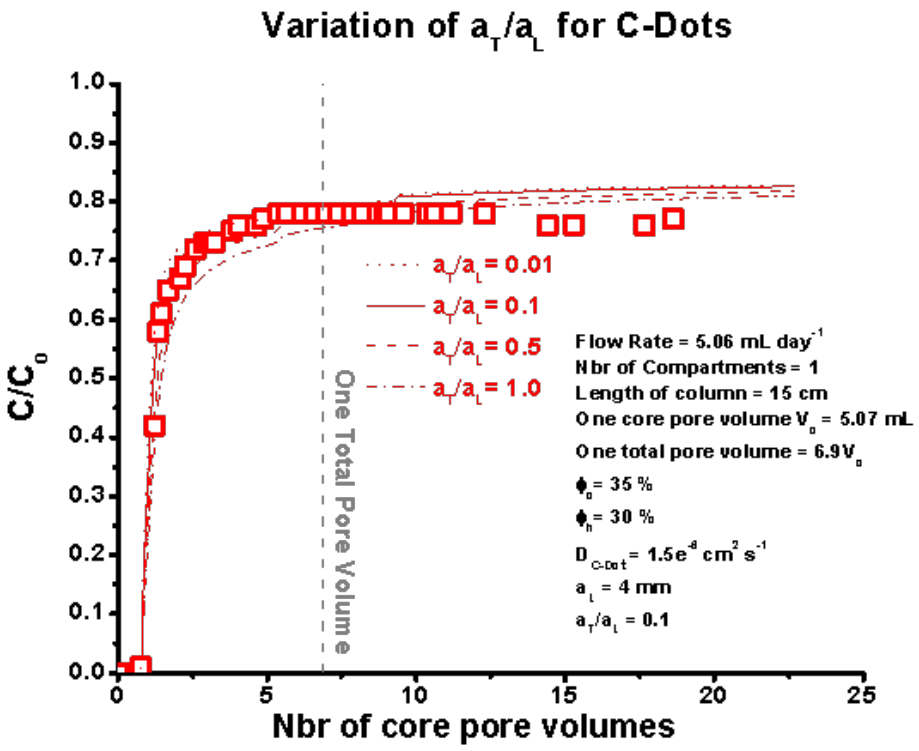

Figure A.27: Rectangular Beadpack (1 Compartment) - Variation of a_T/a_L for C-Dots

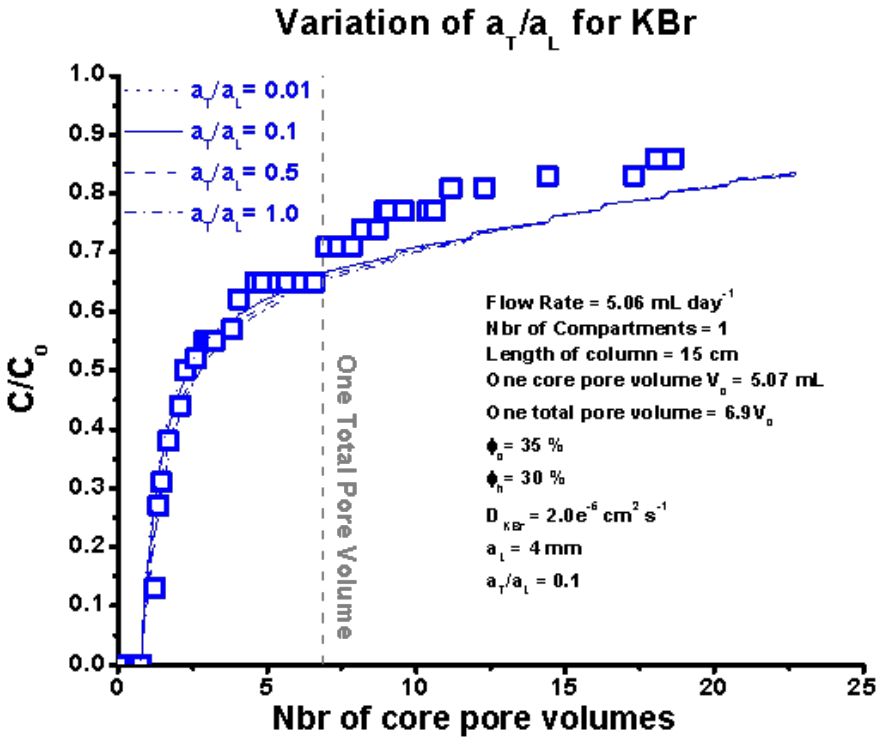

Figure A.28: Rectangular Beadpack (1 Compartment) - Variation of a_T/a_L for KBr

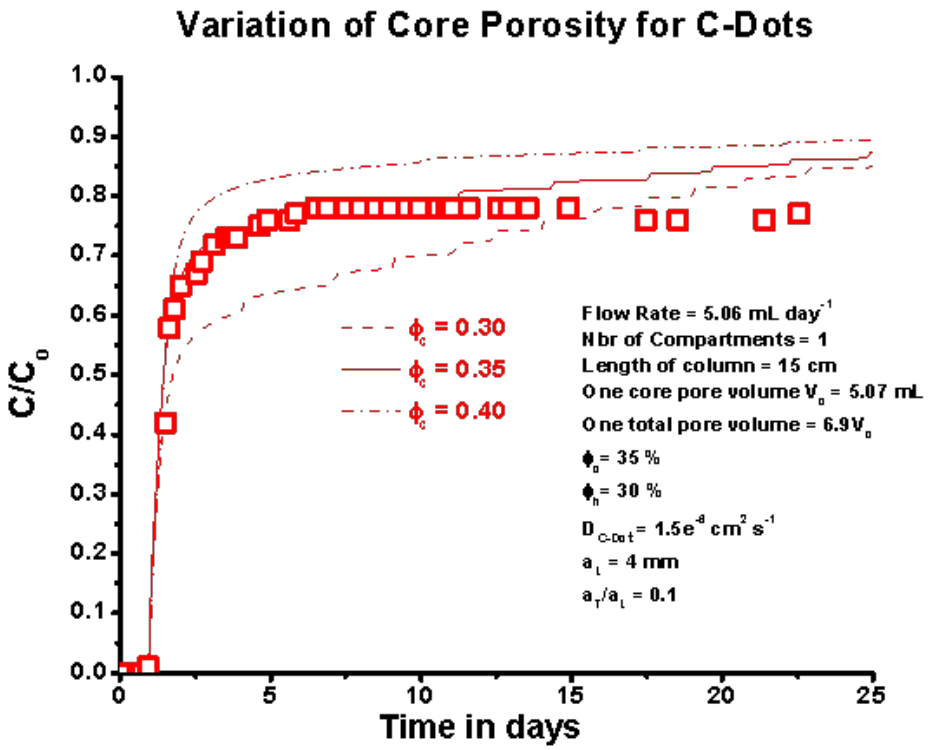

Figure A.29: Rectangular Beadpack (1 Compartment) - Variation of core porosity for C-Dots

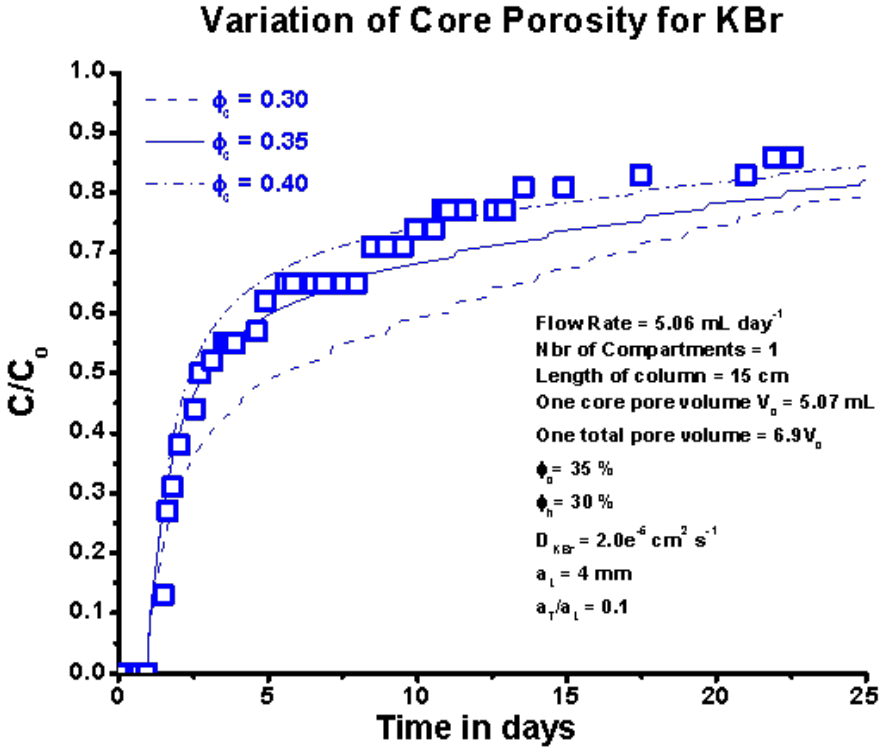

Figure A.30: Rectangular Beadpack (1 Compartment) - Variation of core porosity for KBr

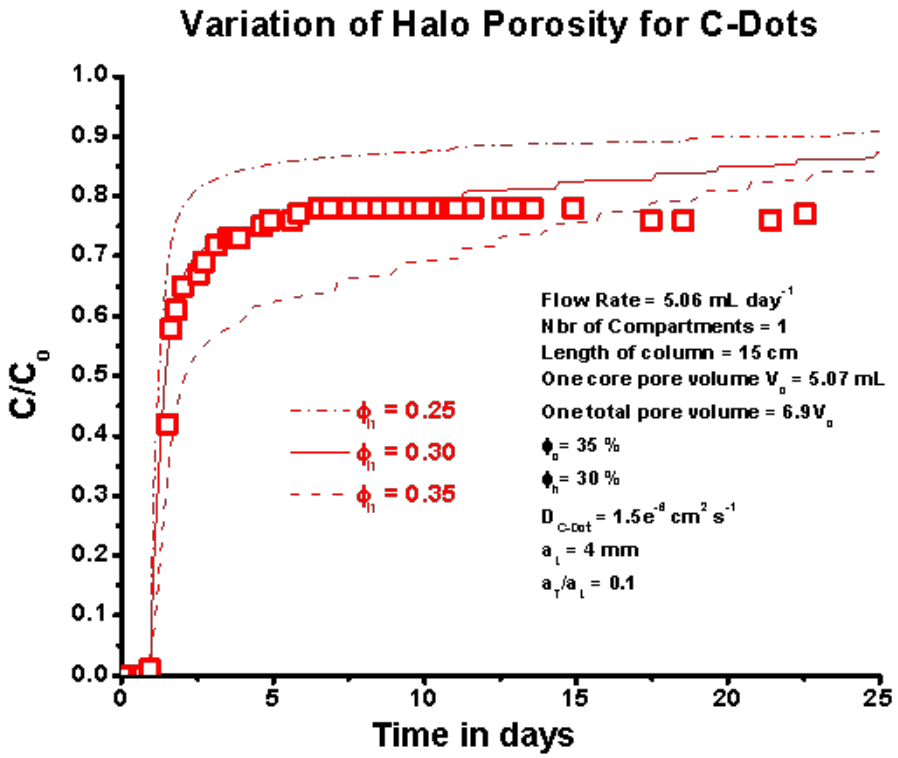

Figure A.31: Rectangular Beadpack (1 Compartment) - Variation of halo porosity for C-Dots

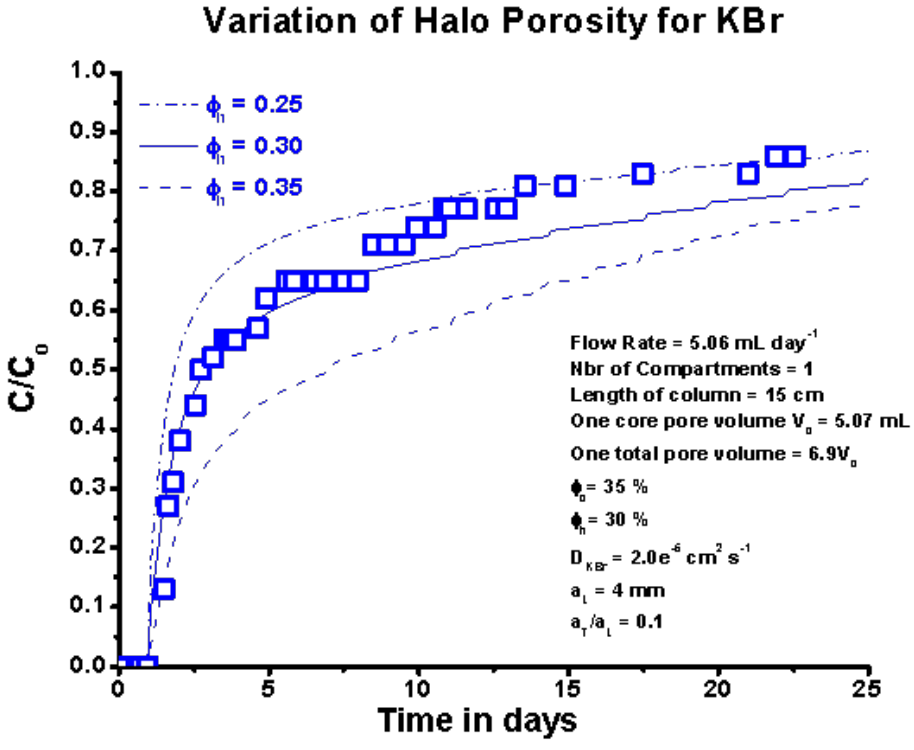

Figure A.32: Rectangular Beadpack (1 Compartment) - Variation of halo porosity for KBr

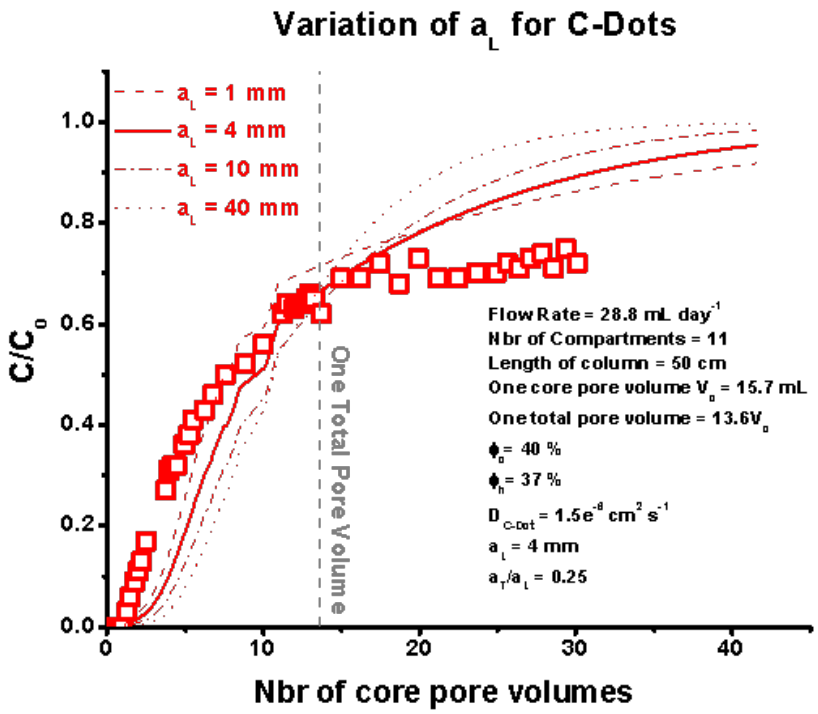

Figure A.33: Plexi-glass Cylindrical Column - Variation of a_L for C-Dots

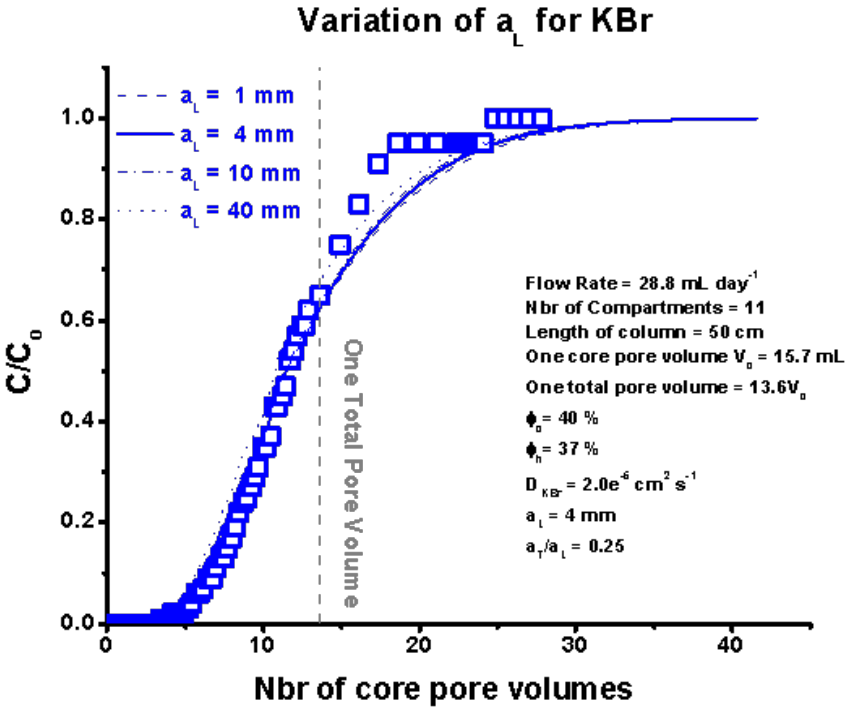

Figure A.34: Plexi-glass Cylindrical Column - Variation of a_L for KBr

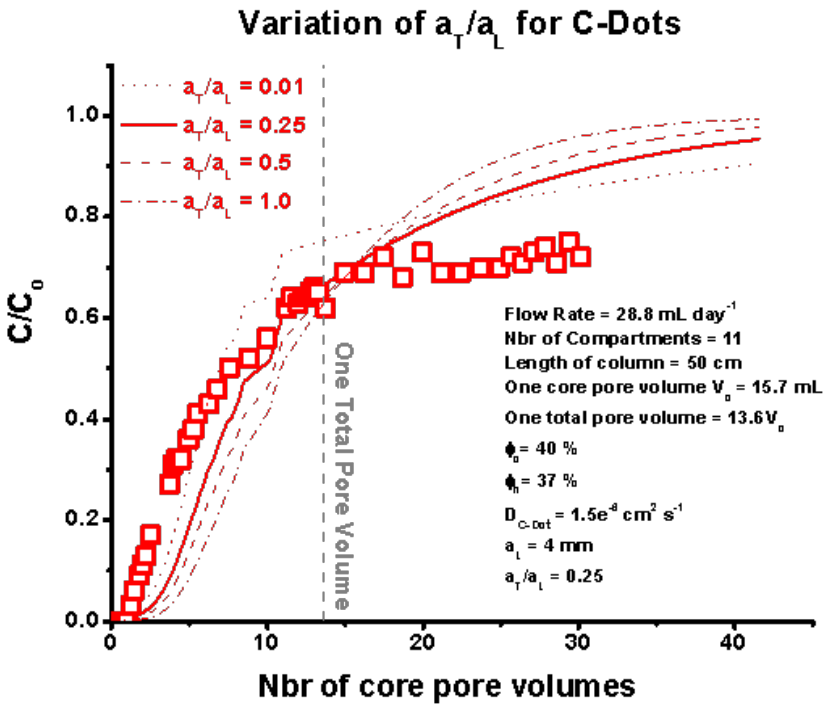

Figure A.35: Plexi-glass Cylindrical Column - Variation of a_T/a_L for C-Dots

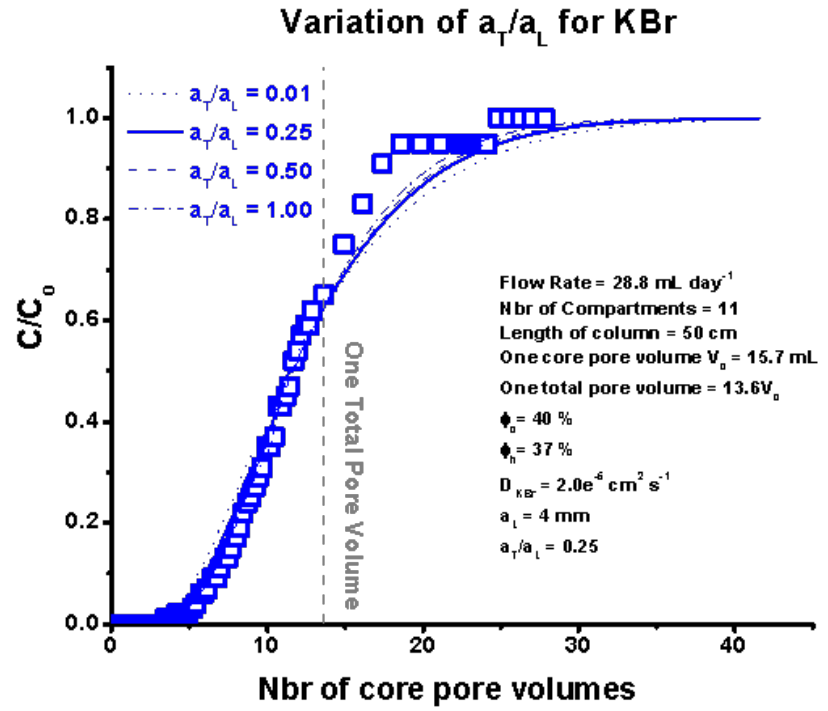

Figure A.36: Plexi-glass Cylindrical Column - Variation of a_T/a_L for KBr

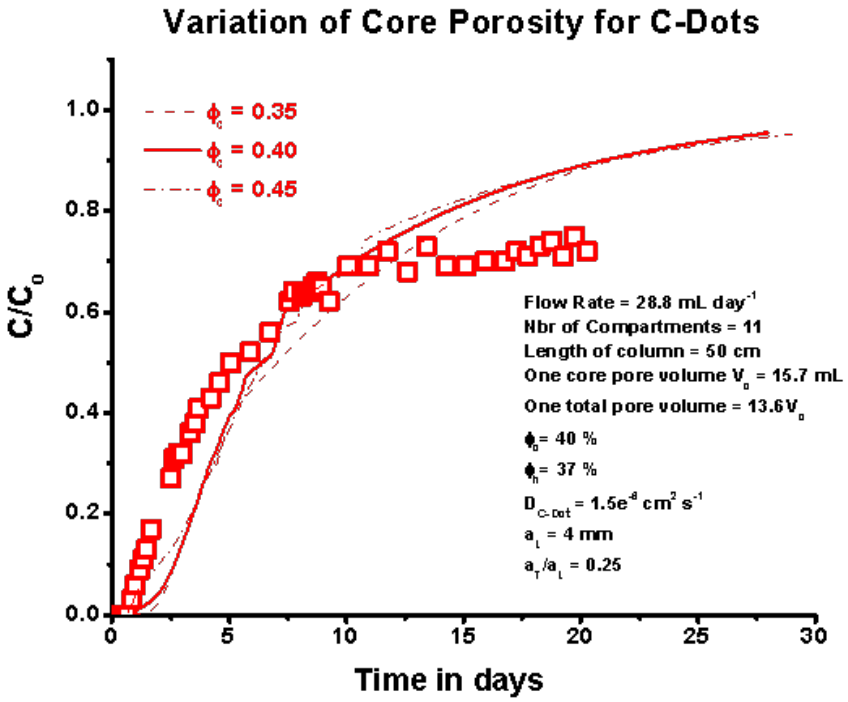

Figure A.37: Plexi-glass Cylindrical Column - Variation of core porosity for C-Dots

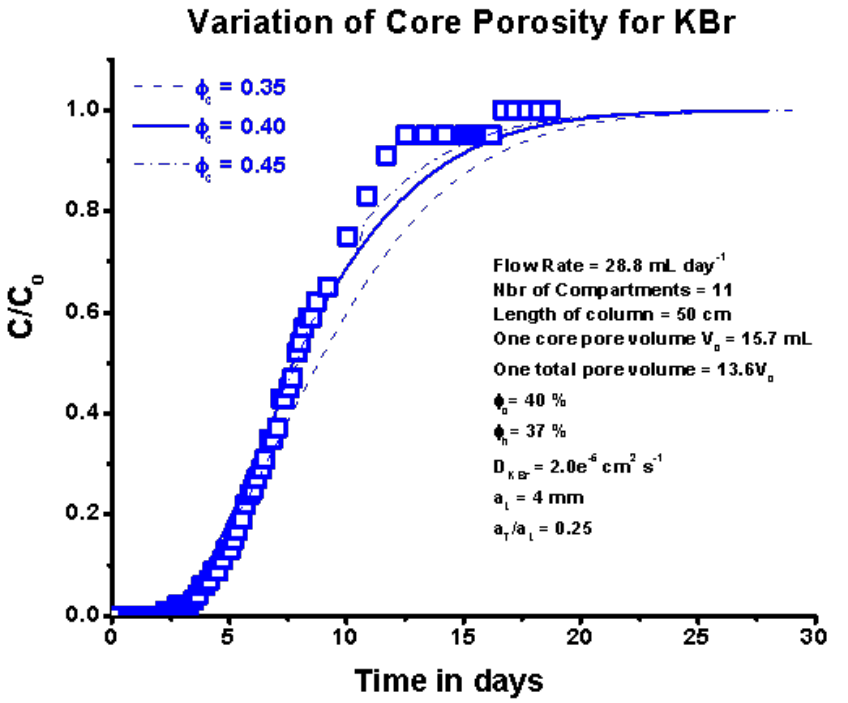

Figure A.38: Plexi-glass Cylindrical Column - Variation of core porosity for KBr

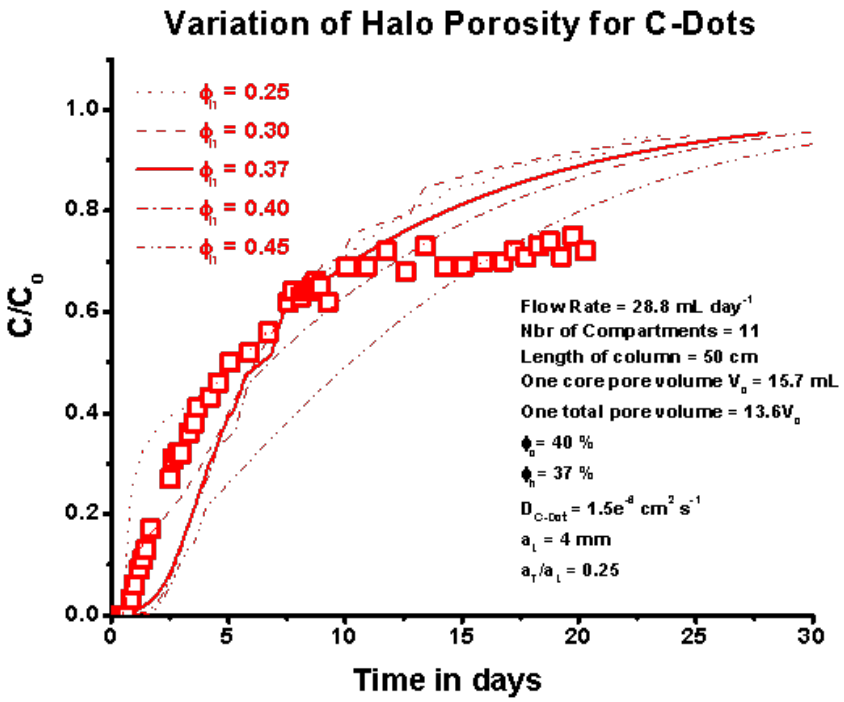

Figure A.39: Plexi-glass Cylindrical Column - Variation of halo porosity for C-Dots

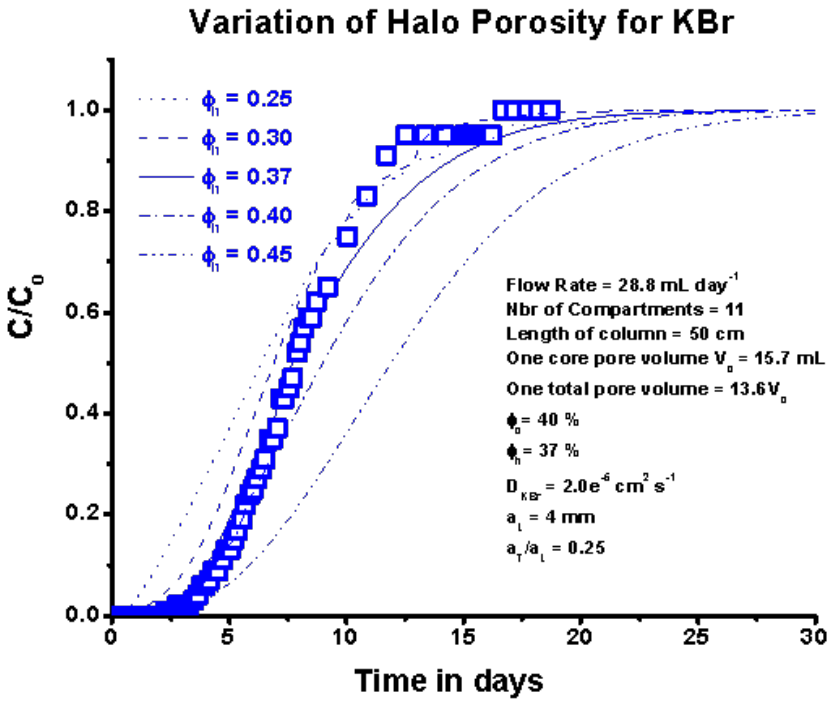

Figure A.40: Plexi-glass Cylindrical Column - Variation of halo porosity for KBr

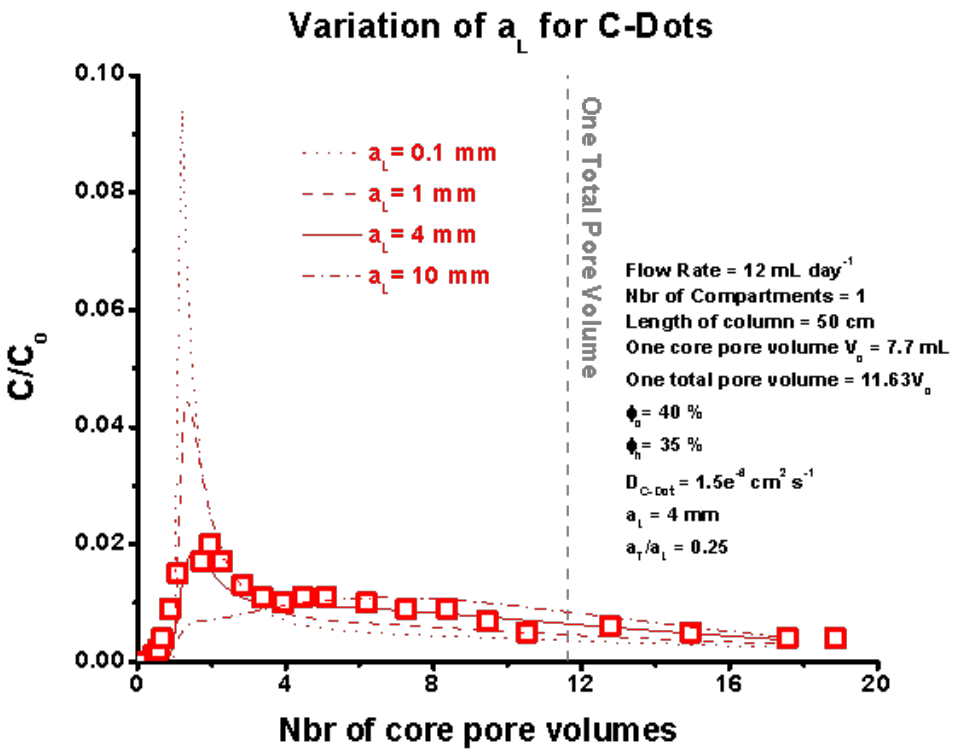

Figure A.41: Stainless Steel Cylindrical Column (slow flow) - Variation of a_L for C-Dots

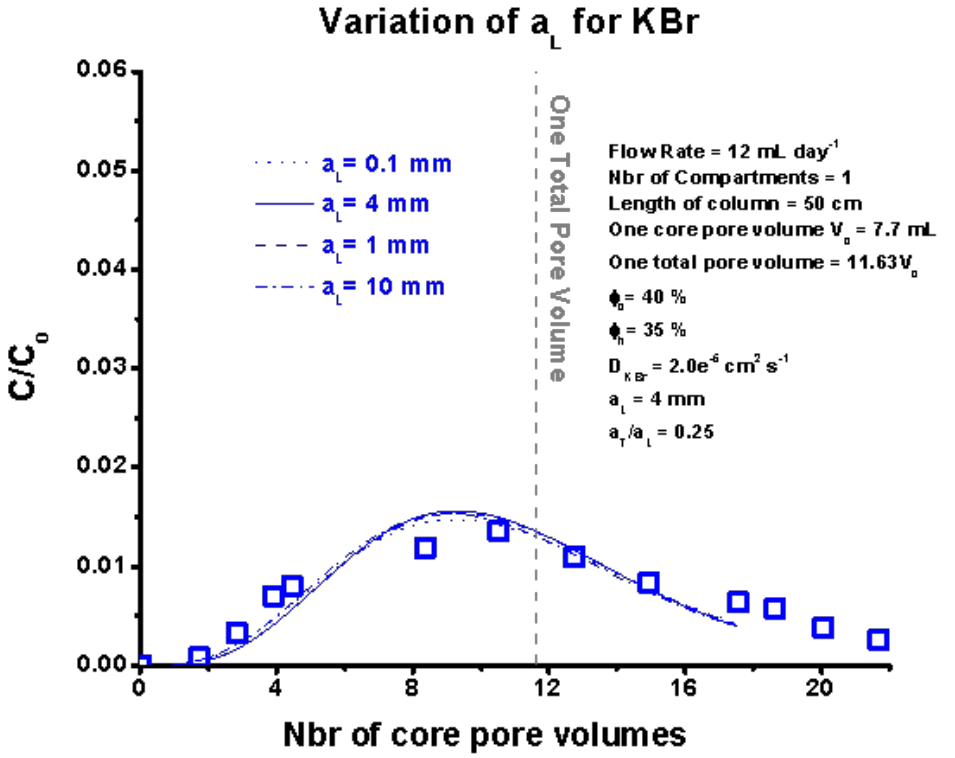

Figure A.42: Stainless Steel Cylindrical Column (slow flow) - Variation of a_L for KBr

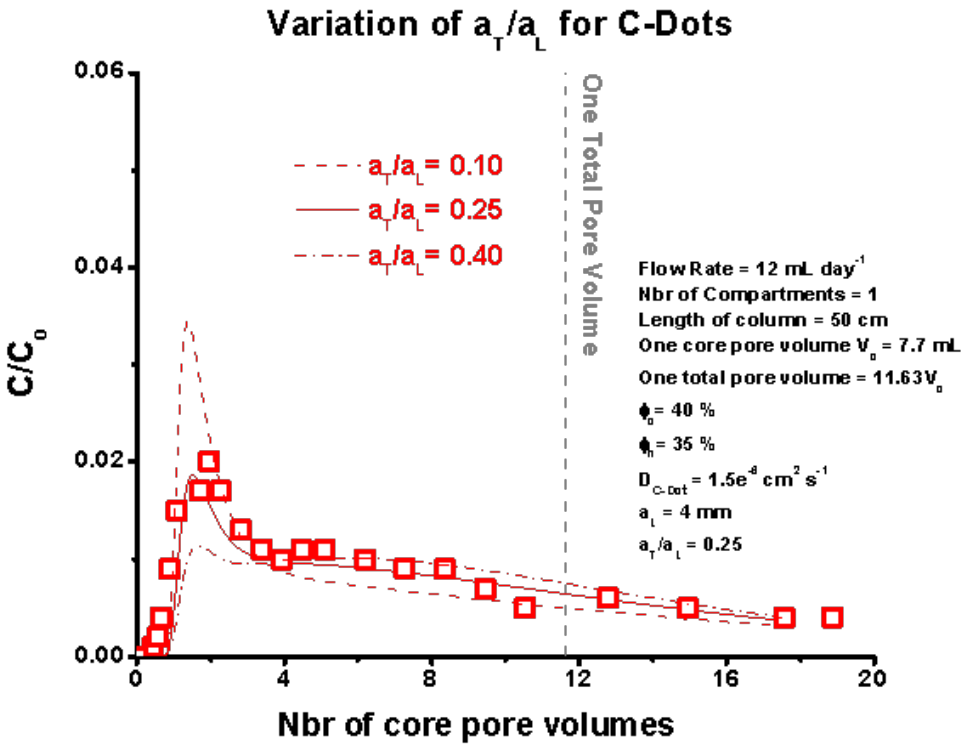

Figure A.43: Stainless Steel Cylindrical Column (slow flow) - Variation of a_T/a_L for C-Dots

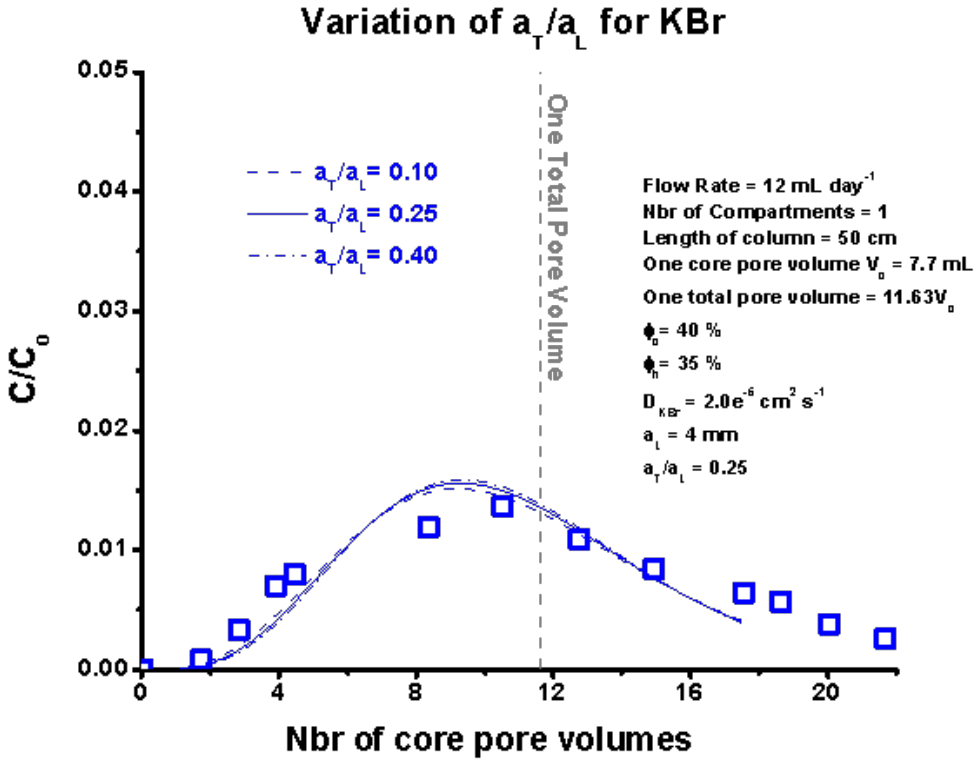

Figure A.44: Stainless Steel Cylindrical Column (slow flow) - Variation of a_T/a_L for KBr

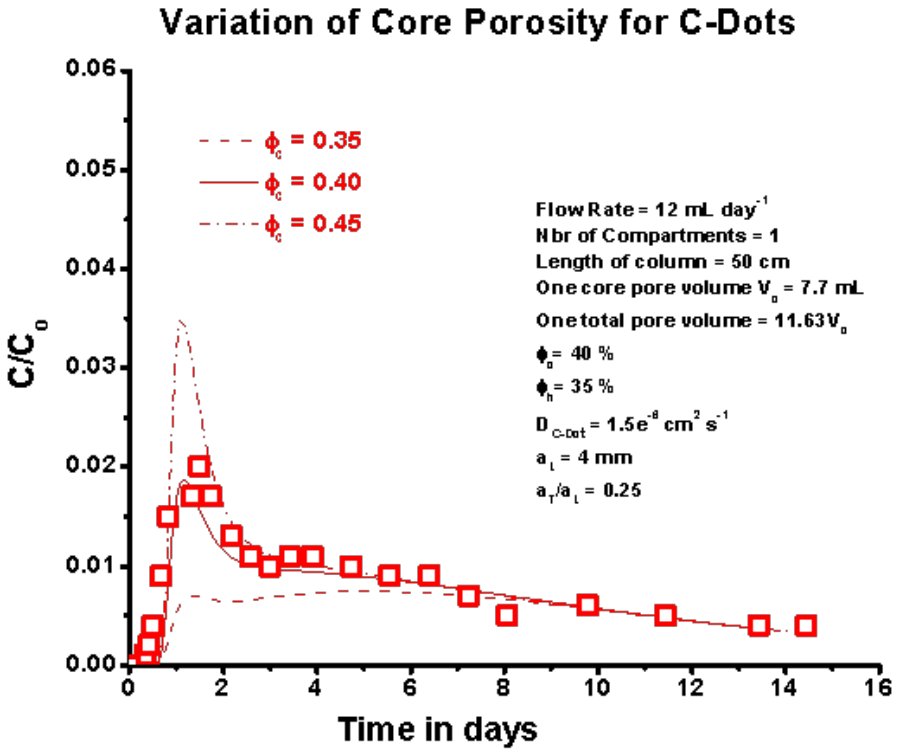

Figure A.45: Stainless Steel Cylindrical Column (slow flow) - Variation of core porosity for C-Dots

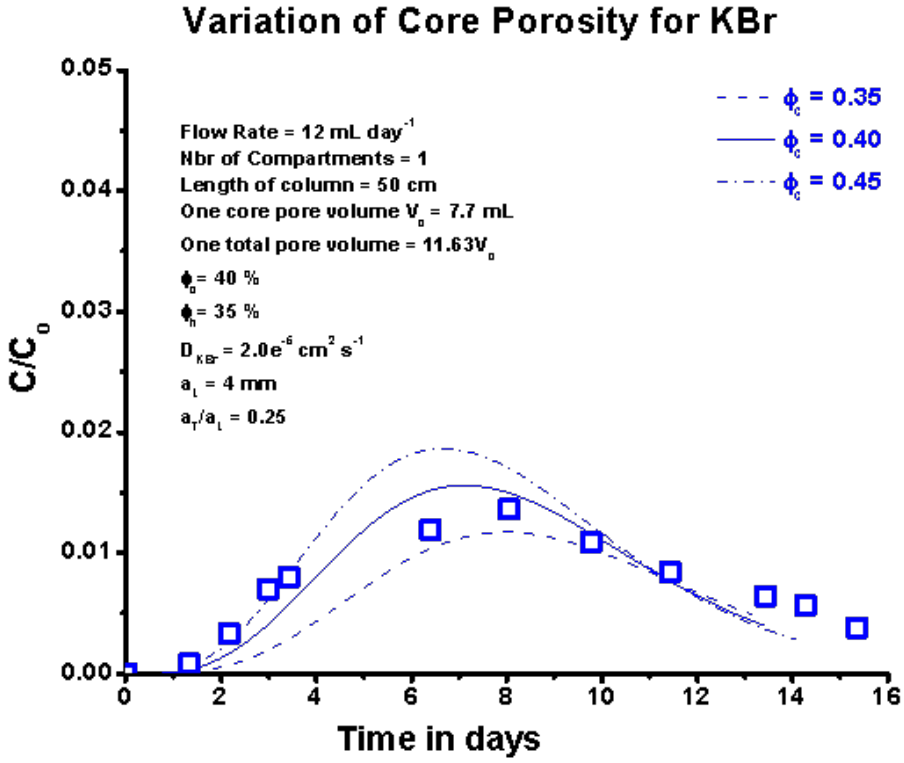

Figure A.46: Stainless Steel Cylindrical Column (slow flow) - Variation of core porosity for KBr

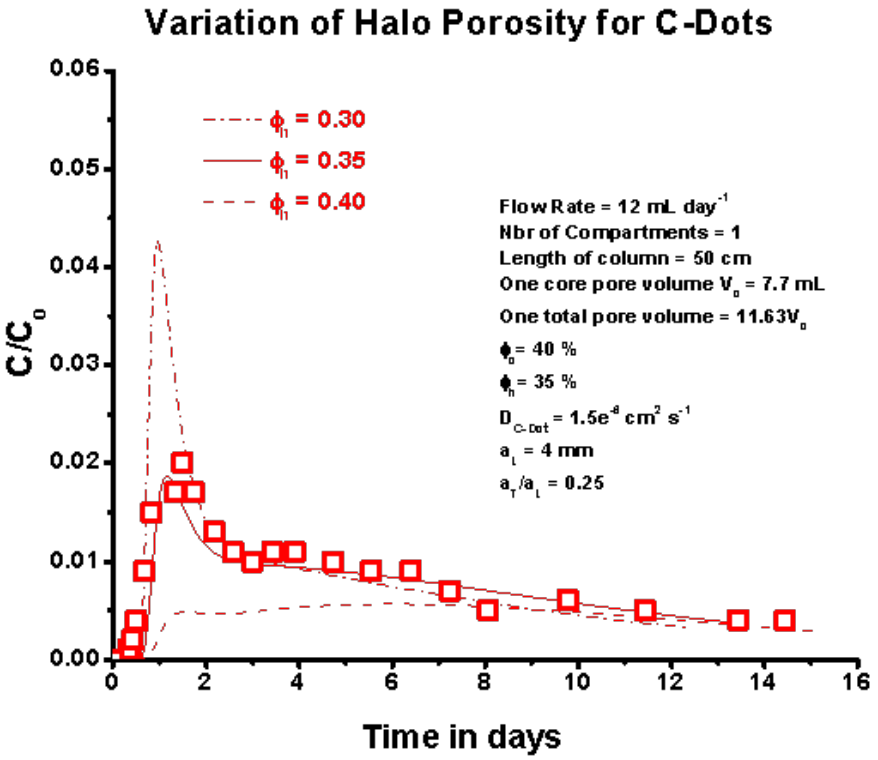

Figure A.47: Stainless Steel Cylindrical Column (slow flow) - Variation of halo porosity for C-Dots

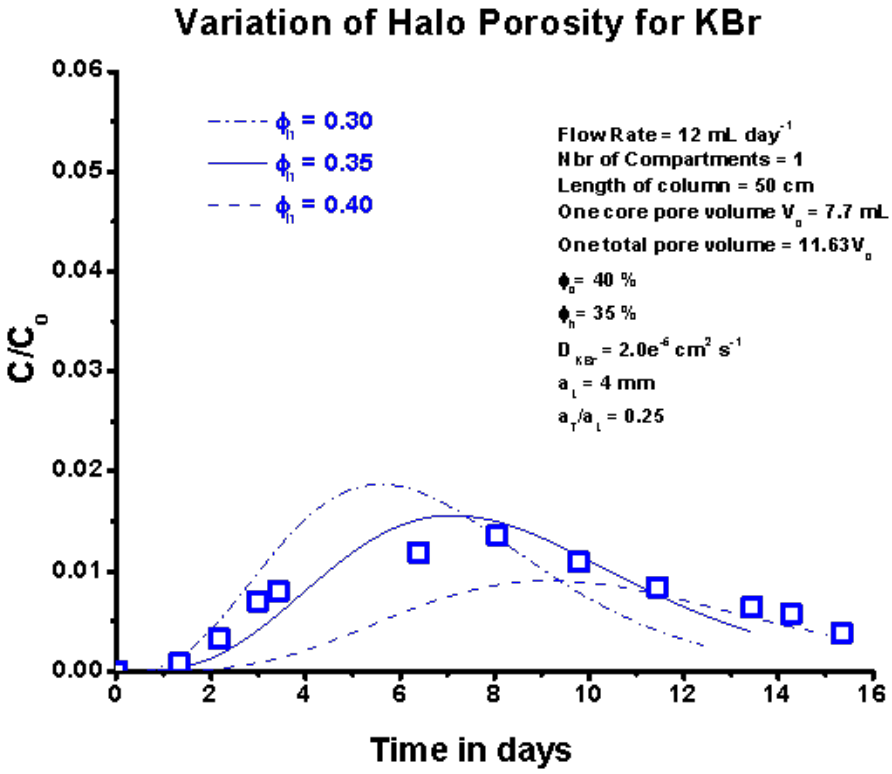

Figure A.48: Stainless Steel Cylindrical Column (slow flow) - Variation of halo porosity for KBr

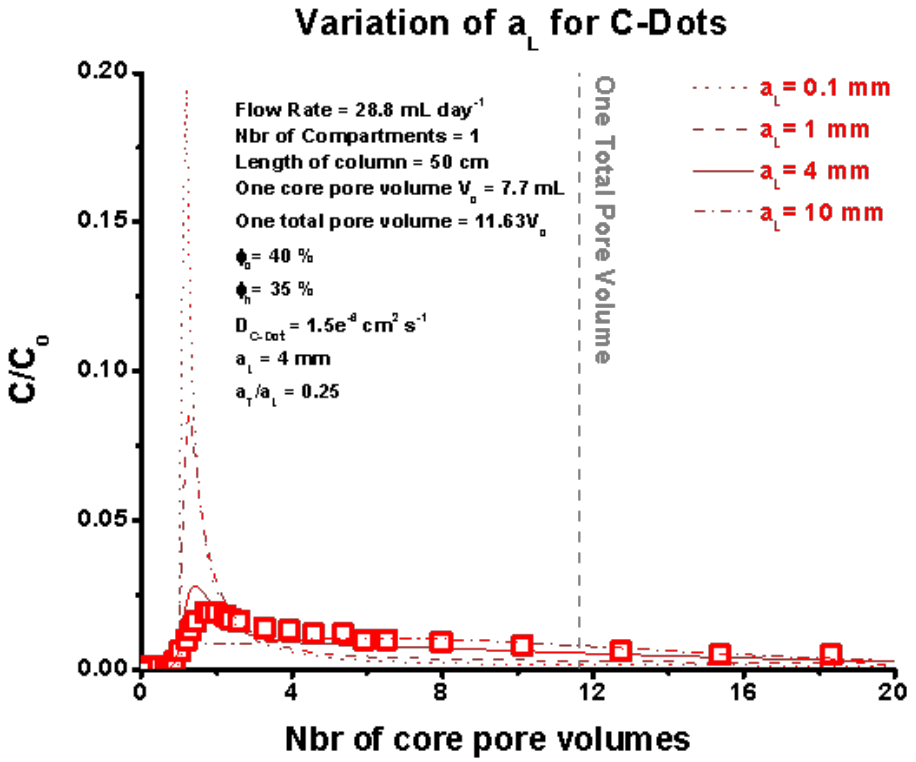

Figure A.49: Stainless Steel Cylindrical Column (fast flow) - Variation of a_L for C-Dots

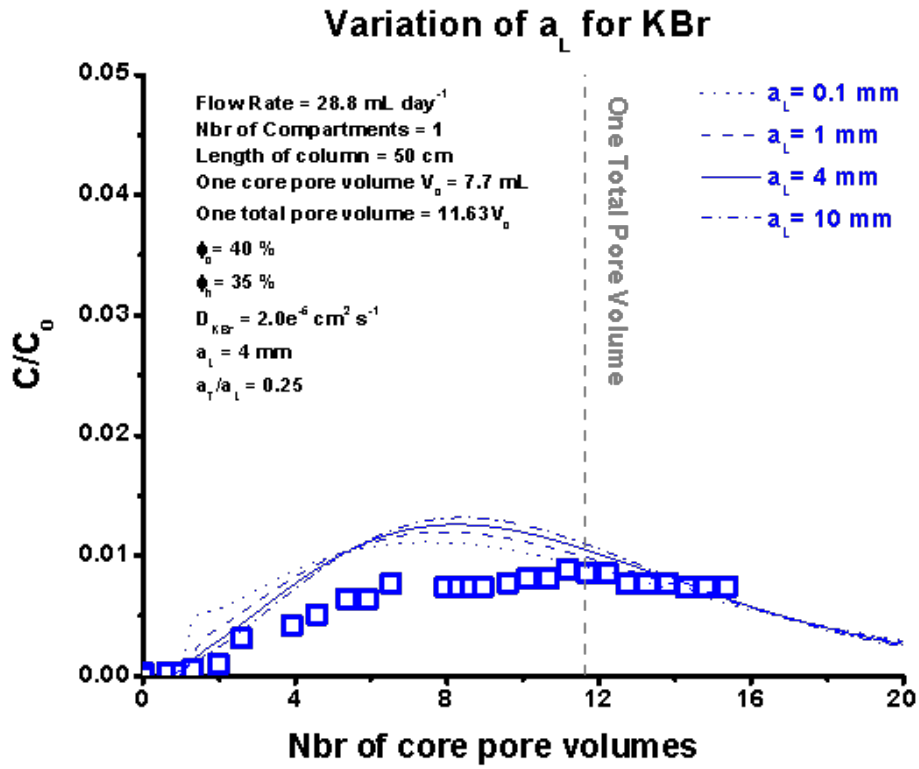

Figure A.50: Stainless Steel Cylindrical Column (fast flow) - Variation of a_L for KBr

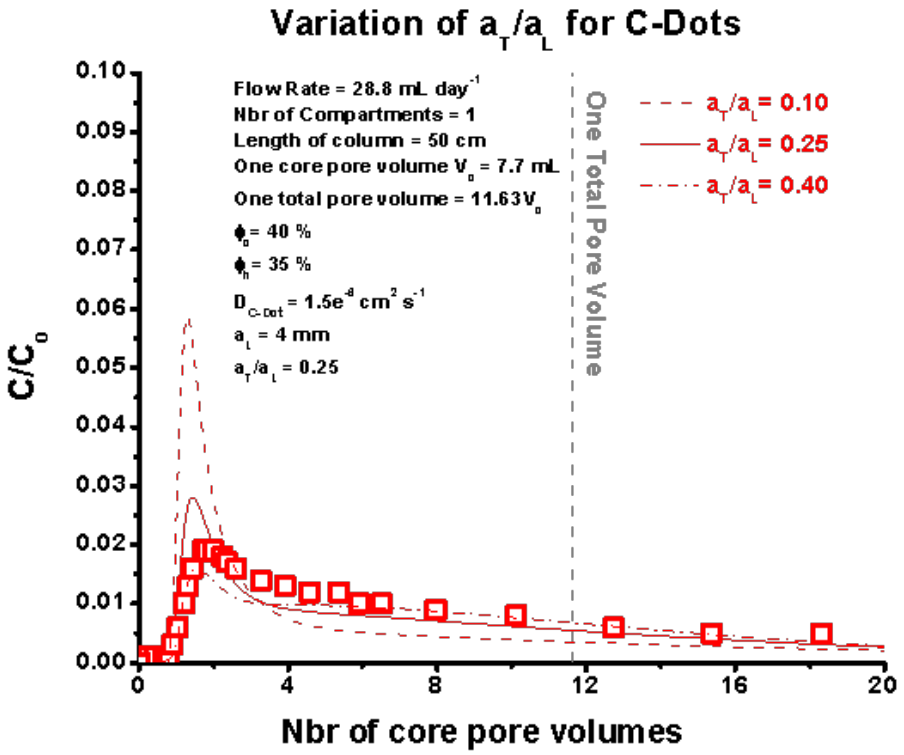

Figure A.51: Stainless Steel Cylindrical Column (fast flow) - Variation of a_T/a_L for C-Dots

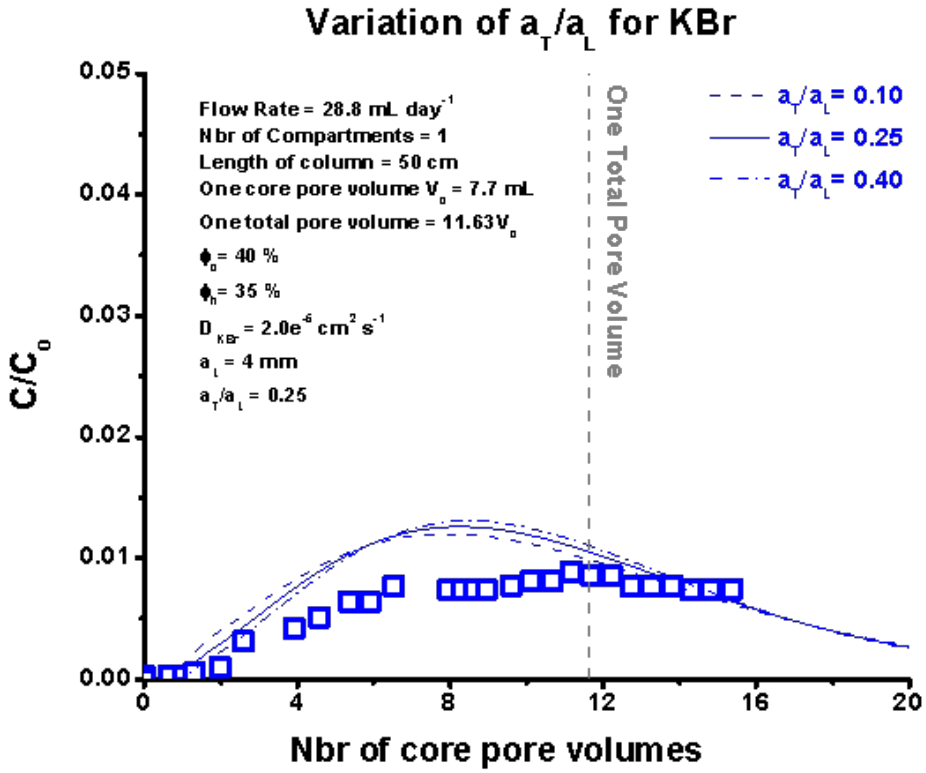

Figure A.52: Stainless Steel Cylindrical Column (fast flow) - Variation of a_T/a_L for KBr

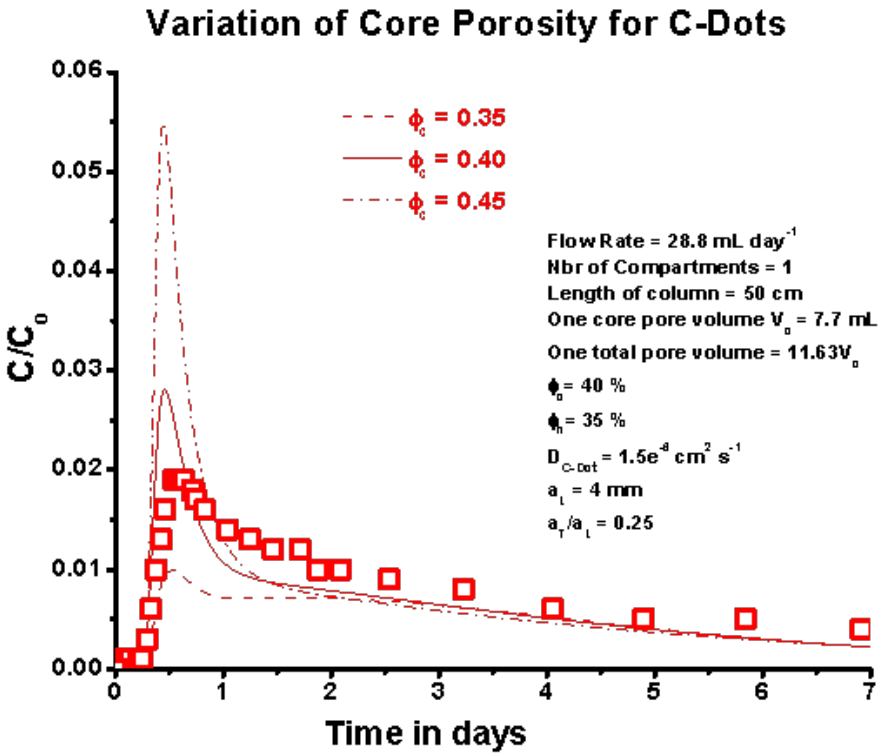

Figure A.53: Stainless Steel Cylindrical Column (fast flow) - Variation of core porosity for C-Dots

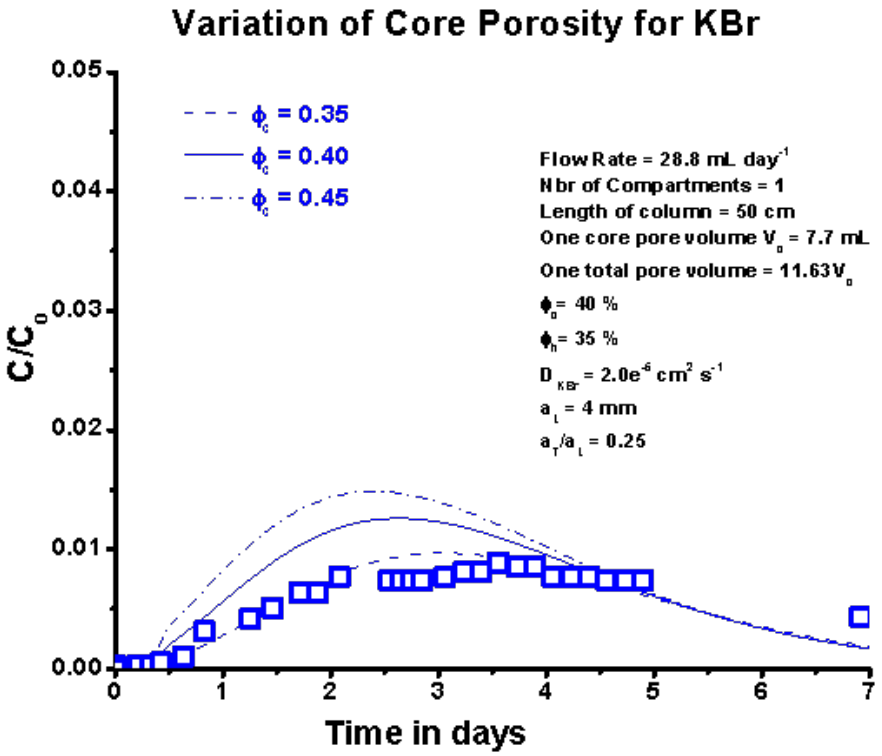

Figure A.54: Stainless Steel Cylindrical Column (fast flow) - Variation of core porosity for KBr

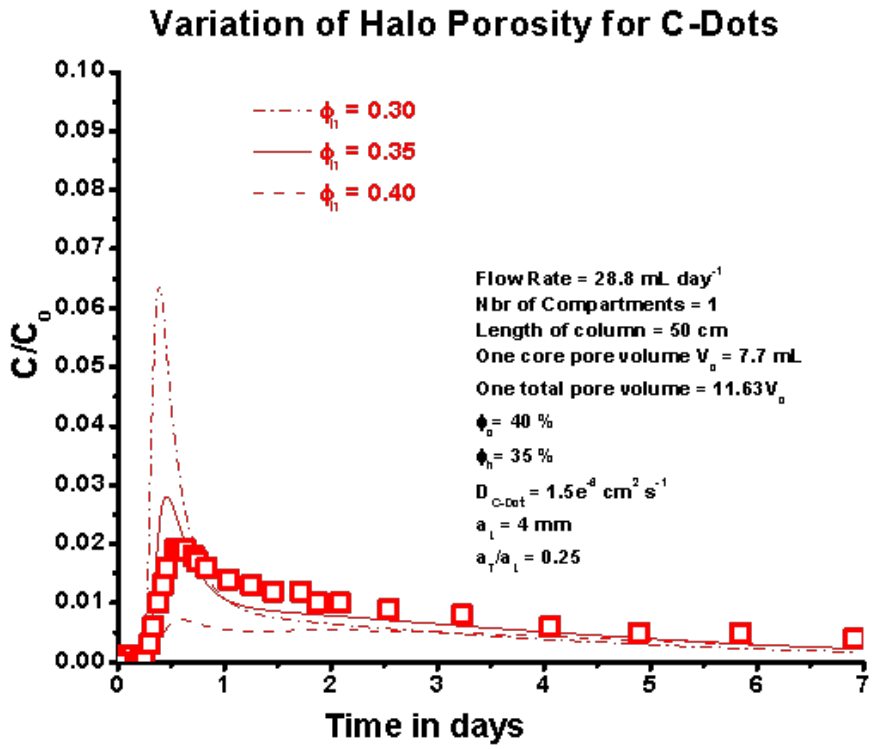

Figure A.55: Stainless Steel Cylindrical Column (fast flow) - Variation of halo porosity for C-Dots

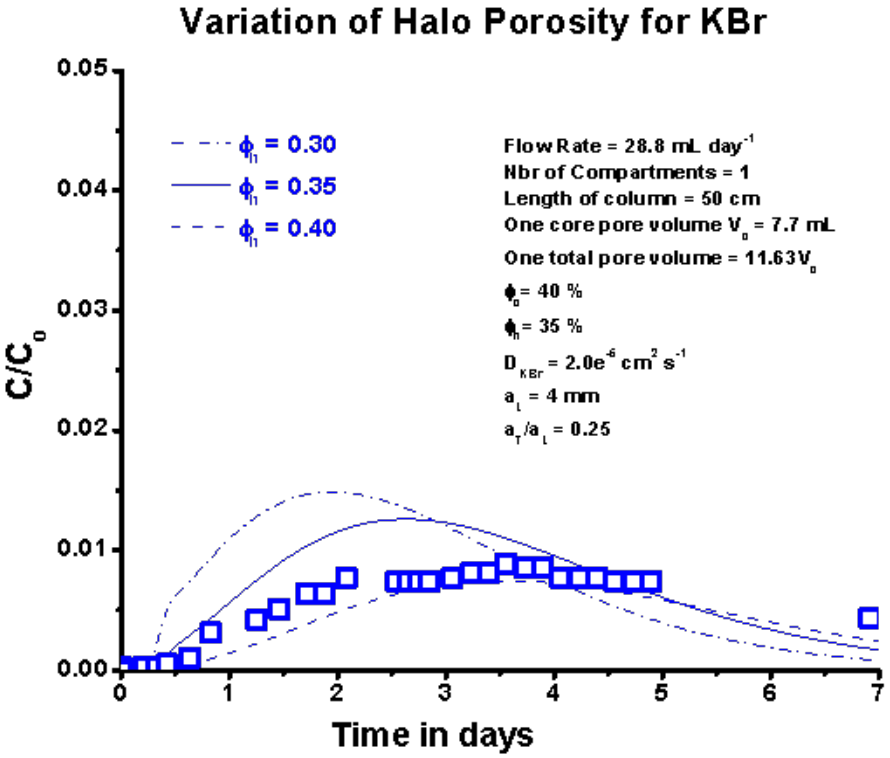

Figure A.56: Stainless Steel Cylindrical Column (fast flow) - Variation of halo porosity for KBr

APPENDIX B: SUMMARY OF PARTICLE-CHEMICAL TRACER EXPERIMENTS FROM LITERATURE

As evident from literature review, tracer experiments are very diverse in terms of tracers, core rock, and degree of fracture or heterogeneity and are tested in various length scales. Several of these experiments have been thoroughly reviewed in the literature section. The geometry and flow properties have been extracted from each experiment and interpreted. Based on our inverse Peclet number, we highlight the dominant flow mechanisms in these studies.

The Inverse Peclet number is applied to interpreting experiments reported in the literature in Table B.1. We constructed this table by determining for each experiment (1) the fluid transit time through the permeable central core or fracture(s) (t_c in column 2), (2) the ratio of the total to the fracture(s) or permeable zone pore volumes (V_t/V_c in column 3), the halo width (H in column 4), and the halo porosity (Φ_h in column 5). We then calculated the transit time for the condition in which the tracer diffused rapidly into the halo (by multiplying the core transit time by V_t/V_c), and the diffusional time constant, t_{diff}, and the inverse Peclet number, N_{iPe}, using equation 2. If N_{iPe} approaches or exceeds 1 for the chemical tracer, but not the particle tracer, we expect to see a delay in the arrival of the chemical relative to the particle tracer. Column 10 indicates whether the experiment behaves in this regard as we expect it should from the calculated value of N_{iPe}. It can be seen that of the 13 experiments tabulated, only 2 contradicted our expectations regarding diffusion. For one of these [17], there are clear indications that the uranine is sticking to the quartz sand. The pore volume in the impermeable filters is not sufficient to account for the observed delay in the uranine tracer. We have no good explanation for the failure of the latex spheres in the experiment by [21] to arrive earlier than the KBr tracer,

other than that there was very low recovery of the latex spheres, and the spheres may have been delayed by sticking to a mineral surface in the shale. The clearest diffusional delay is shown by [57] who inject a tracer pulse through fractured shale, but the recovery of the particles was very low. Three of the four field tests are expected to and do show a clear delay in the arrival of the chemical tracer, but the recovery of the particles in three of these tests was very low, and the fourth was perhaps compromised by chemical alteration of the particles before they were all analyzed [25]. The table shows that although very few experiments have been carried out that probe diffusion into stagnant areas adjacent to zones where fluid is flowing, but (as indicated in the "agreement" column) those that have are in good accord with the diffusional sequestration expected based on an easily calculated inverse Peclet number, N_{iPe}.

Table B.1 Summary of literature describing experiments involving chemical and/or particle tracers in heterogeneous porous media. Parameters from papers indicated in column 2-7 are used to calculate an inverse peclet number (Col 8) for the chemical tracer. If N_{ipe} approaches or exceeds 1, arrival of chemical tracer is expected. The 9th column records the observe results and the 10th indicated if there is agreement with the N_{ipe} predictions

Reference	t_c (days)	V_t/V_c	t_{adv} (days)	H (cm)	Φ_h	t_{diff} (days)	$N_{ipe}=t_{adv}/t_{diff}$	Observation	Agree-ment	"Rock" type	Tracers Particles (Chemical)	C/Co (%)	Comments
[23]	0.0206	203	4.2	8	0.4	138.9	0.03	Small delay in chemical tracer	Y	Core, Cut fracture chalk	Latex: 20,200,1000 nm (Br^-)	75,100,90 (92.5)	Cut fracture
[16]	0.0118	9.52	0.113	1.6	0.38	5.89	0.02	No Delay in chemical tracer	Y	Lab, Quartz sand	Silica spheres: 100 nm (Cl^-)	100 (100)	Core in cyl column
[21]	0.012	74.55	0.9	1	0.38	2.28	0.39	No Delay in chemical tracer	N	Core, Fractured shale	Latex: 50,100,500,1000 nm (Br^-)	0.14,0.28, 1.4,1 (100)	Low concentrations indicate sticking and lack of clear separation
[57]	0.23	74.5	1.71	1	0.38	2.28	0.75	Delay	Y	Core, Fractured shale	Latex: 100,500,1000,2100 nm (Br^-)	Pulse	Low recoveries
[17]	0.0227	1.41	0.0319	1	0.104	34.77	0.001	Delay	N	Lab, Dual porosity quartz sandpacks	Latex: 1000 nm (Uranine)	70, (94)	Uranine delayed more than expected
[26]	0.00579	3	1.74	2.4	0.3	16.65	0.104	Separation	-	Core, Fractured Tuff Block	Latex: 280,980 nm (Γ)	90 (80)	High recoveries
[26]	1.07	50	50	5	0.05	216	0.25	Separation	-	Field, fractured granite	Latex: 360, 830 nm (D_2O)	10,1 (80%)	Low Recovery for large spheres

Table B.1 continued

Reference	t_c (days)	V_t/V_c	t_{adv} (days)	H (cm)	Φ_h	t_{diff} (days)	$N_{ipe}=t_{adv}/t_{diff}$	Observation	Agree-ment	"Rock" type	Tracers Particles (Chemical)	C/Co (%)	Comments
[18]	0.0157	7.8	0.091	1.15	0.3	3.82	0.024	No Separation	Y	Lab, Dual permeable quartz Sandpacks	Latex: 1000,3200 nm (Br^-)	60 (100%)	Straining studied
[25]	10.57	100	1000	10	0.1	867	1.22	Delay	Y	Field, fractured igneous rock	Silica spheres: 500 nm (Cl^-)	50 (0%)	NaCl never recovered
[58]	0.18	200	36	1	0.2	4.33	8.3	Delay	Y	Field, fractured saprolite	Latex: 100nm, bacteriophage (Dye)	10^{-5} pulse (10^{-3})	Very Low Recovery
[59]	1.8	320	575	10	0.32	270	2.12	Delay	Y	Field, fractured clay till	Bacteriophage (Br^-)	-	Very Low Recovery
[60]	0.277	11.8	3.3	5	0.1	188	0.02	No Delay	Y	Core, Cut Fracture in granite core	(THO)	100	No particle tracers
[61]	0.025	348	8.8	2	0.35	9.9	0.89	Delay	Y	Core, Fractured Till	($CaCl_2$)	80	No particle tracers

REFERENCES

1. Shapiro, A.M., *Effective matrix diffusion in kilometer-scale transport in fractured crystalline rock.* Water Resources Research, 2001. **37**(Compendex): p. 507-522.
2. Neretnieks, I., *Solute transport in fractured rock : applications to radionuclide waste repositories*1990, Stockholm.
3. Grisak, G.E. and J.F. Pickens, *An analytical solution for solute transport through fractured media with matrix diffusion.* Journal of Hydrology, 1981. **52**(1-2): p. 47-57.
4. Grisak, G.E. and J.F. Pickens, *Solute transport through fractured media. I. The effect of matrix diffusion.* Water Resources Research, 1980. **16**(Copyright 1981, IEE): p. 719-30.
5. Gillham, R.W., et al., *An Advection-Diffusion Concept for Solute Transport in Heterogeneous Unconsolidated Geological Deposits.* Water Resour. Res., 1984. **20**(3): p. 369-378.
6. Dagan, G., *Solute transport in heterogeneous porous formations.* Journal of Fluid Mechanics, 1984. **145**: p. 151-177.
7. Wiesner, M.R. and J.-Y. Bottero, *Environmental nanotechnology : applications and impacts of nanomaterials*2007, New York: McGraw-Hill.
8. Wan, J. and J.L. Wilson, *Colloid transport in unsaturated porous media.* Water Resour. Res., 1994. **30**(4): p. 857-864.
9. Ryan, J.N. and M. Elimelech, *Colloid mobilization and transport in groundwater.* Colloids and Surfaces A: Physicochemical and Engineering Aspects, 1996. **107**(Compendex): p. 1-1.
10. McCarthy, J.F. and L.D. McKay, *Colloid Transport in the Subsurface -- Past, Present, and Future Challenges.* Vadose Zone Journal, 2004. **3**(2): p. 326-337.
11. Frimmel, F.H., et al. *Colloidal transport in porous media*. 2007; Available from: http://dx.doi.org/10.1007/978-3-540-71339-5.
12. Auset, M. and A.A. Keller, *Pore-scale processes that control dispersion of colloids in saturated porous media.* Water Resour. Res., 2004. **40**(3): p. W03503.
13. McCarthy, J.F. and J.M. Zachara, *Subsurface transport of contaminants.* Environmental Science & Technology, 1989. **23**(5): p. 496-502.
14. Kanti Sen, T. and K.C. Khilar, *Review on subsurface colloids and colloid-associated contaminant transport in saturated porous media.* Advances in Colloid and Interface Science, 2006. **119**(2-3): p. 71-96.
15. Kretzschmar, R., et al., *Mobile Subsurface Colloids and Their Role in Contaminant Transport*, in *Advances in Agronomy*, L.S. Donald, Editor 1999, Academic Press. p. 121-193.
16. Saiers, J.E., G.M. Hornberger, and C. Harvey, *Colloidal silica transport through structured, heterogeneous porous media.* Journal of Hydrology, 1994. **163**(3-4): p. 271-288.
17. Niehren, S. and W. Kinzelbach, *Artificial colloid tracer tests: development of a compact on-line microsphere counter and application to soil column experiments.* Journal of Contaminant Hydrology, 1998. **35**(1-3): p. 249-259.

18. Bradford, S., et al., *Straining and attachment of colloids in physically heterogeneous porous media.* Vadose Zone Journal, 2004(3): p. 384-394.
19. Silliman, S.E., *Particle transport through two-dimensional, saturated porous media: influence of physical structure of the medium.* Journal of Hydrology, 1995. **167**(1-4): p. 79-98.
20. Toran, L. and A.V. Palumbo, *Colloid transport through fractured and unfractured laboratory sand columns.* Journal of Contaminant Hydrology, 1992. **9**(3): p. 289-303.
21. Cumbie, D.H. and L.D. McKay, *Influence of diameter on particle transport in a fractured shale saprolite.* Journal of Contaminant Hydrology, 1999. **37**(1-2): p. 139-157.
22. McCarthy, M.a.B., *Influence of ionic strength and cation charge on transport of colloidal particles in fractured shale saprolite.* Environment Science and Technology, 2002. **36**: p. 3735-3743.
23. Zvikelsky, O. and N. Weisbrod, *Impact of particle size on colloid transport in discrete fractures.* Water Resour. Res., 2006. **42**(12): p. W12S08.
24. Reimus, P.W., *The use of synthetic colloids in tracer transport experiments in saturated rock fractures*, in *Other Information: DN: NM; TH: Thesis. Submitted to University of New Mexico, Albuquerque,; PBD: Aug 1995*1995. p. Medium: ED; Size: 252 p.
25. Cathles, L., H. Spedden, and E. Malouf, *A tracer technique to measure the diffusional accesability of matrix block mineralization.* American Institute of Mining, 1974. **103rd Annual Meeting**.
26. Becker, M.W., P.W. Reimus, and P. Vilks, *Transport and Attenuation of Carboxylate-Modified Latex Microspheres in Fractured Rock Laboratory and Field Tracer Tests.* Ground Water, 1999. **37**(3): p. 387-395.
27. McKay, L.D., et al., *A field example of bacteriophage as tracers of fracture flow.* Environmental Science & Technology, 1993. **27**(6): p. 1075-1079.
28. Harvey, R.W., et al., *Role of physical heterogeneity in the interpretation of small-scale laboratory and field observations of bacteria, microbial-sized microsphere, and bromide transport through aquifer sediments.* Water Resour. Res., 1993. **29**(8): p. 2713-2721.
29. Harvey, R.W., *Microorganisms as tracers in groundwater injection and recovery experiments: a review.* FEMS Microbiology Reviews, 1997. **20**(3-4): p. 461-472.
30. Kass, W. and H. Behrens, *Tracing technique in geohydrology*1998, Rotterdam, Netherlands; Brookfield, VT: Balkema.
31. Bales, R.C., et al., *Bacteriophage adsorption during transport through porous media: chemical perturbations and reversibility.* Environmental Science & Technology, 1991. **25**(12): p. 2088-2095.
32. Bhattacharjee, S., J.N. Ryan, and M. Elimelech, *Virus transport in physically and geochemically heterogeneous subsurface porous media.* Journal of Contaminant Hydrology, 2002. **57**(3-4): p. 161-187.
33. Fontes, D.E., et al., *Physical and chemical factors influencing transport of microorganisms through porous media.* Applied and Environmental Microbiology, 1991. **57**(9): p. 2473-2481.
34. Murphy, E.M. and T.R. Ginn, *Modeling microbial processes in porous media.* Hydrogeology Journal, 2000. **8**(1): p. 142-158.

35. Redman, J.A., S.L. Walker, and M. Elimelech, *Bacterial Adhesion and Transport in Porous Media:,Äâ Role of the Secondary Energy Minimum.* Environmental Science & Technology, 2004. **38**(6): p. 1777-1785.
36. Petosa, A.R., et al., *Aggregation and Deposition of Engineered Nanomaterials in Aquatic Environments: Role of Physicochemical Interactions.* Environmental Science & Technology, 2010. **44**(17): p. 6532-6549.
37. Rodriguez and et.al., *Enhanced migration of surface-treated nanoparticles in sedimentary rocks.* 2009.
38. Kanj, M.Y., J. Funk, and Z. Al-Yousif, *Nanofluid Coreflood Experiments in the ARAB-D.* SPE, 2009. **SPE126161**.
39. Kanel, S.R., et al., *Transport of surface-modified iron nanoparticle in porous media and application to arsenic(III) remediation.* Journal of Nanoparticle Research, 2007. **9**(5): p. 725-735.
40. Mazen, Y.K., H. Rashid, and E. Giannelis, *Industry First Field Trial of Reservoir Nanoagents.* SPE 142592, 2011.
41. Muller, C.B., et al., *Precise measurement of diffusion by multi-color dual-focus fluorescence correlation spectroscopy.* EPL (Europhysics Letters), 2008. **83**(4): p. 46001.
42. Newman, *Electrochemical Systems*1973.
43. Saffman, P.G. and G. Taylor, *The Penetration of a Fluid into a Porous Medium or Hele-Shaw Cell Containing a More Viscous Liquid.* Proceedings of the Royal Society A: Mathematical, Physical and Engineering Sciences, 1958. **245**(1242): p. 312-329.
44. Bear, J., *Dynamics of fluids in porous media*1972, New York: American Elsevier Pub. Co.
45. Toth, J., *A theory of groundwater motion in small drainage basins in central alberta canada.* Journal of Geophysical Research, 1962. **67**(11).
46. Bodin, J., F. Delay, and G. de Marsily, *Solute transport in a single fracture with negligible matrix permeability: 1. fundamental mechanisms.* Hydrogeology Journal, 2003. **11**(4): p. 418-433.
47. Maloszewski, P. and A. Zuber, *Tracer experiments in fractured rocks: Matrix diffusion and the validity of models.* Water Resour. Res., 1993. **29**(8): p. 2723-2735.
48. Callahan, T.J., et al., *Using multiple experimental methods to determine fracture/matrix interactions and dispersion of nonreactive solutes in saturated volcanic tuff.* Water Resour. Res., 2000. **36**(12): p. 3547-3558.
49. Jardine, P.M., et al., *Quantifying diffusive mass transfer in fractured shale bedrock.* Water Resour. Res., 1999. **35**(7): p. 2015-2030.
50. Yao, K.-M., M.T. Habibian, and C.R. O'Melia, *Water and waste water filtration. Concepts and applications.* Environmental Science & Technology, 1971. **5**(11): p. 1105-1112.
51. McDowell-Boyer, L.M., J.R. Hunt, and N. Sitar, *Particle transport through porous media.* Water Resources Research, 1986. **22**(Copyright 1987, IEE): p. 1901-21.
52. Kretzschmar, R. and H. Sticher, *Colloid transport in natural porous media: influence of surface chemistry and flow velocity.* Physics and Chemistry of The Earth, 1998. **23**(2): p. 133-139.

53. Godinez, I.G. and C.J.G. Darnault, *Aggregation and transport of nano-TiO2 in saturated porous media: Effects of pH, surfactants and flow velocity.* Water Research, 2011. **45**(2): p. 839-851.
54. Kretzschmar, R., et al., *Experimental determination of colloid deposition rates and collision efficiencies in natural porous media.* Water Resour. Res., 1997. **33**(5): p. 1129-1137.
55. Derjaguin, B. and L. Laundau, *Theory of the stability of strongly charged lyophobic sols and of the adhesion of strongly charged particles in solutions of electrolytes.* Acta Physicochem, 1941. **14**: p. 733-762.
56. Kobayashi, M., et al., *Aggregation and Charging of Colloidal Silica Particles:,Äâ Effect of Particle Size.* Langmuir, 2005. **21**(13): p. 5761-5769.
57. McCarthy, McKay, and Bruner, *Influence of ionic strength and cation charge on transport of colloidal particles in fractured shale saprolite.* Environment Science and Technology, 2002. **36**: p. 3735-3743.
58. McKay, L.D., W.E. Sanford, and J.M. Strong, *Field-Scale Migration of Colloidal Tracers in a Fractured Shale Saprolite.* Ground Water, 2000. **38**(1): p. 139-147.
59. McKay, L.D., R.W. Gillham, and J.A. Cherry, *Field experiments in a fractured clay till: 2. Solute and colloid transport.* Water Resour. Res., 1993. **29**(12): p. 3879-3890.
60. Neretnieks, I., T. Eriksen, and P.i. T‰htinen, *Tracer movement in a single fissure in granitic rock: Some experimental results and their interpretation.* Water Resour. Res., 1982. **18**(4): p. 849-858.
61. Grisak, G.E., J.F. Pickens, and J.A. Cherry, *Solute transport through fractured media: 2. Column study of fractured till.* Water Resour. Res., 1980. **16**(4): p. 731-739.